MODE-LOCKED RAMAN LASER IN H_2 PUMPED BY A MODE-LOCKED EXTERNAL CAVITY DIODE LASER

by

Yihan Xiong

A dissertation submitted in partial fulfillment
of the requirements for the degree

of

Doctor of Philosophy

in

Physics

MONTANA STATE UNIVERSITY
Bozeman, Montana

July 2007

APPROVAL

of a dissertation submitted by

Yihan Xiong

This dissertation has been read by each member of the dissertation committee and has been found to be satisfactory regarding content, English usage, format, citations, bibliographic style, and consistency, and is ready for submission to the Division of Graduate Education.

Dr. John L. Carlsten

Approved for the Department of Physics

Dr. William A. Hiscock

Approved for the Division of Graduate Education

Dr. Carl A. Fox

STATEMENT OF PERMISSIN TO USE

In presenting this dissertation in partial fulfillment of the requirements for a doctoral degree at Montana State University, I agree that the Library shall make it available to borrowers under rules of the Library. I further agree that copying of this dissertation is allowable only for scholarly purposes, consistent with "fair use" as prescribed in the U. S. Copyright Law. Requests for extensive copying or reproduction of this dissertation should be referred to Bell & Howell Information and Learning, 300 North Zeeb Road, Ann Arbor, Michigan 48106, to whom I have granted "the exclusive right to reproduce and distribute my dissertation in and from microform along with the non-exclusive right to reproduce and distribute my abstract in any format in whole or in part."

Yihan Xiong

July 2007

ACKNOWLEDGEMENTS

I would like to express my utmost gratitude to Dr. John Carlsten, my advisor, for guiding me through the whole doctoral program, for furthering my passion for physics and for improving my personality.

My sincere appreciation goes to Drs. Lei Meng, Kevin Repasky and Peter Roos who helped me get started in the lab and gave me many illuminating thoughts and discussions. Thanks also go to those people who helped me in my research project: Norm Williams, Paul Nachman and Peter Sellin. In addition, I want to thank the rest of my group members, Amin Nehrir, David Hoffman, Seth Humphries, Chris Melton, Charlie Keith and Mike Obland for many pleasurable moments in the lab.

I send my special thanks to Sytil Murphy, my labmate, for keeping me company in the lab everyday, for helping me through this academic exploration and for improving my English.

Last but not the least; I would like to thank my husband, upcoming baby and parents for their endless love and support.

TABLE OF CONTENTS

TABLE OF CONTENTS − CONTINUED

LIST OF FIGURES

Figure Page

LIST OF FIGURES − CONTINUED

Figure Page

LIST OF FIGURES − CONTINUED

Figure Page

LIST OF FIGURES − CONTINUED

Figure Page

LIST OF FIGURES − CONTINUED

Figure Page

LIST OF FIGURES − CONTINUED

Figure Page

LIST OF FIGURES − CONTINUED

Figure Page

ABSTRACT

In this thesis, a theory is first presented for a far-off resonance mode-locked Raman laser in H_2 with high finesse cavity enhancement. The theoretical derivation for the mode-locked Raman laser is based on semiclasscial laser theory and time-dependent continuous wave (CW) Raman theory. Numerically calculated results, including the intra-cavity fields' amplitude and phase evolution and output Stokes power versus input pump power are discussed in three different regimes depending on the relationship between the coherence dephasing rate and the repetition rate of the mode-locked pump laser. Then experimentally, first an actively mode-locked external-cavity diode laser (ML-ECDL) was built along with a demonstration of how to frequency lock all the longitudinal modes from the ML-ECDL to a high finesse cavity. Then a tapered amplifier diode system was designed to increase the ML-ECDL power. Finally, a far-off resonance mode-locked Raman laser pumped by a ML-ECDL was demonstrated. With nine longitudinal pump modes, when operating at an average power level slightly above the CW threshold (3.89 mW), each of the pump modes, taken on its own, is below the CW lasing threshold. If these pump modes are not in-phase, the threshold will be nine times the CW threshold, roughly 35 mW. However the measured threshold for the ML Raman laser is about 5.4 mW, much less than 35 mW, because the pump modes are in-phase, and they can augment each other through four-wave-mixing processes causing all of them to lase as expected from the theory. The full width half maximum of the ML Stokes output is 310 ps. The beat signals from the ML Stokes showed that the Stokes pulses were made of at least eight modes.

CHAPTER 1

INTRODUCTION

Raman Scattering

To understand a Raman laser, we first need to explain Raman scattering, which was discovered by Chandrasekhara Venkata Raman in 1928 and for which he received the 1930 Nobel Prize in physics.

Scattering is one of the most common phenomena of everyday life. We see objects due to the light scattering from the object's surface. We see blue skies and red sunsets because sunlight scatters from molecules in the atmosphere.

When light interacts with atoms or molecules, most photons are elastically scattered (Rayleigh scattering): the scattered photons have the same energy (frequency) as the incident photons. However, a small fraction of the scattered light is at different frequencies, usually lower than the frequency of the incident photons. This is inelastic scattering, and Raman scattering is in this category. In a gas, Raman scattering can occur with a change in vibrational, rotational or electronic energy of the scattering molecule.

In Raman scattering, when the scattering molecule absorbs energy, we call it "Stokes scattering"; when the molecule loses energy, we have Raman anti-Stokes scattering. Figure 1-1 shows Rayleigh, Raman Stokes and Raman anti-Stokes using an energy level diagram. In Rayleigh scattering, the molecule absorbs an incident photon of energy $h\nu_0$ and then emits a photon with the same energy. For Stokes scattering, an

incident photon with energy $h\nu_0$ yields a scattered photon at $h(\nu_0 - \nu_{21})$ and leaves the energy $h\nu_{21}$ in the scattering molecule. For anti-Stokes scattering, the scattered photon's energy is $h(\nu_0 + \nu_{21})$ where the additional energy of $h\nu_{21}$ is taken from the molecule.

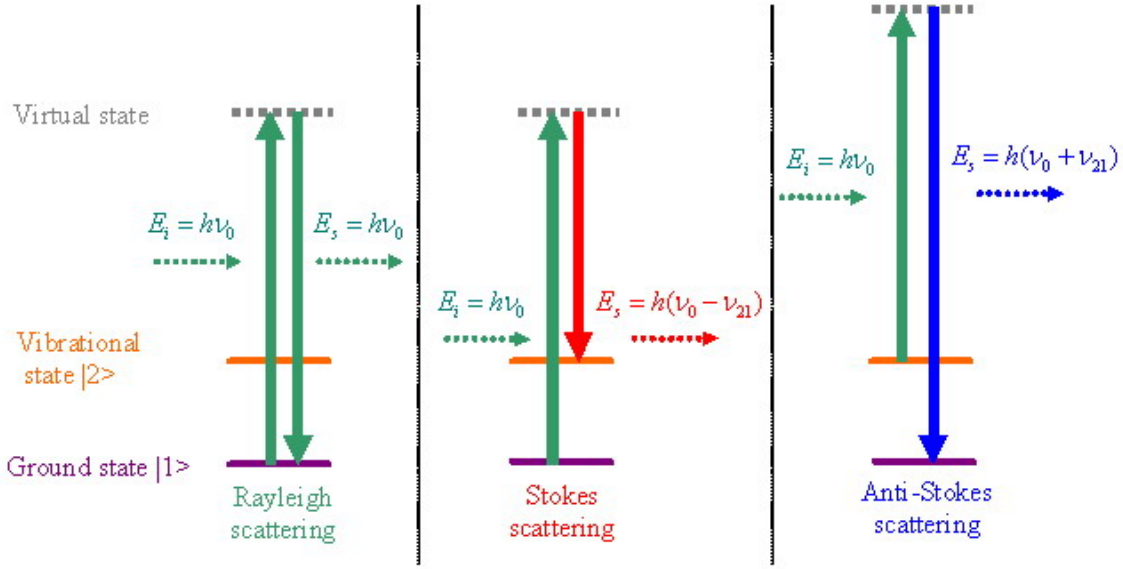

Figure 1-1. Three different types of scattering. Rayleigh (no energy exchange), Stokes (molecule absorbs energy) and anti-Stokes (molecule loses energy). $E_{i(s)}$ represents the incident and scattering photon energies. ν_0 is the incident photon's frequency. $h\nu_{21}$ is the energy difference between the vibrational state and the ground state.

Stimulated Raman Scattering

Now that we have a basic understanding of Raman scattering, let us discuss stimulated Raman scattering (SRS) [1]. SRS was first discovered, rather accidentlly, by Woodbury and Ng [2] in 1962. It was found in the investigation of a Q-switched ruby laser, utilizing a Kerr cell with nitrobenzene in the optical cavity, that the laser's output

red-ruby light intensity decreased, rather than increased, at high excitation of the ruby. At the same time, a strong infrared emission occured, the result of SRS.

In order to make the spontaneous Raman scattering into SRS, either a high gain (G) or long propagation path (z) is needed because $I_s = I_{s0}e^{Gz}$, where I_{s0} is the spontaneous Raman scattering intensity. Most SRS studies are under the far-off-resonance condition as shown in figure 1-2, which means the pump laser frequency is much smaller than the frequency difference between the ground state and the excited electronic state, so the gain of the SRS is very low. The Raman gain is proportional to pump intensity, so normally a high-power pulsed solid-state laser is used for the pump source and the SRS threshold is in the range of 10-10^3 kW of pump power [3-6].

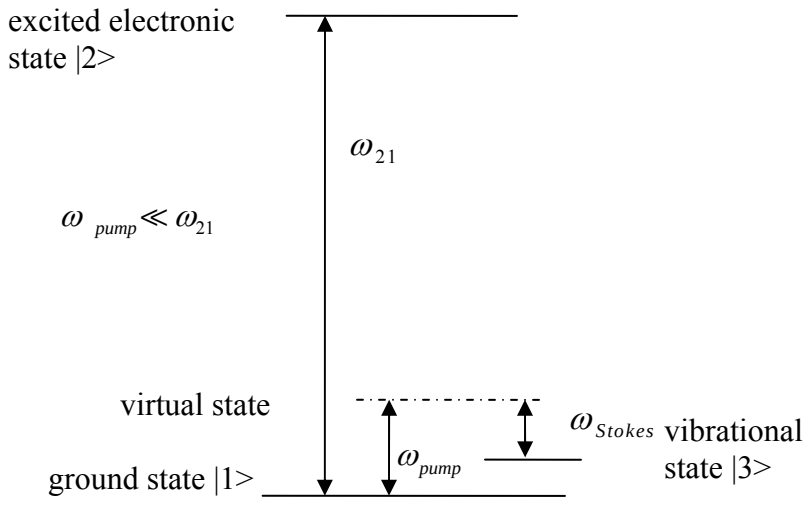

Figure 1-2. Far-off resonance energy level configuration. The pump laser frequency ω_{pump} is much less than the frequency difference between the ground state and excited electronic state ω_{21}.

Raman Laser

Raman lasing requires taking the spontaneoulsy scattered Raman light and amplifiying it inside an optical cavity to emit a coherent laser beam. In other words, inside the optical cavity, the cirulating electric field must constructively interfere with the incoming electric field.

The solid state pulsed lasers used in SRS are not good pump sources for Raman lasers because the pulse width, in general, is much shorter than a useable cavity length. This relationship between the pulse width and the cavity length makes the build up of the intra-cavity coherence (phases between fields) very difficult, but not impossible. An example of such a system has been shown by J. H. Dennis and P.E. Tannenwald [7].

For a CW pump, since the far-off resonance gain is so low, most previous CW Raman lasers used near-resonance pumping, including a 67 μm CW Rb Raman laser in $^{14}NH_3$ [8], a dye laser pumped CW sodium Raman laser near the Na D_1 line [9], a two photon pumped CW Rb Raman laser near 776 nm [10] and various CW Raman laser near the Ne resonance in the He-Ne laser discharge tube [11-13]. Since those lasers were near-resonance, the frequency tunability was very limited. In recent years, the Carlsten group started to use high-finesse-cavity (HFC) enhancement to increase the gain inside the Raman cavity — allowing them to create a far-off resonance CW Raman Laser. The spectra of the CW pump and Stokes are shown schematically in figure 1-3 (the Stokes intensity can be smaller, equal or larger than the pump intensity). These HFCs, whether linear or ring, consist of mirrors with high reflectivities (>99.99%) resulting in a finesse

of 10^4 or higher. Furthermore, the mirrors were double coated so high finesse can be realized at both the pump and Stokes wavelengths.

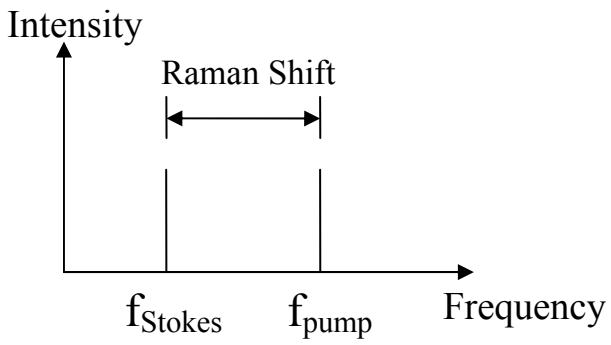

Figure 1-3. CW Raman laser frequency shift.

Far-off Resonance CW Raman Laser Development

The first far-off resonance CW Raman laser was achieved by Brasseur *et al.* [14] in 1998. The pump was a frequency-doubled Nd:YAG laser, and the Raman gain medium was hydrogen gas (H_2). Then Roos *et al.* [15] demonstrated the first diode-pumped CW Raman laser, using a free-running diode laser and a passive optical locking technique. Because these lasers operate far off resonance with virtual states involved in the two-photon Raman process, their gain depends only weakly upon the pump wavelength. Thus, using external cavity diode lasers (ECDL) that can be tuned over tens of nm, Meng *et al.* [16] developed widely-tunable CW Raman lasers.

With the build-up of pump laser power provided by the HFCs, the lasing threshold can be lower than 1 mW. With the variety of commercially available low-cost diode lasers and with common gases such as CH_4 and H_2 for the Raman medium, CW Raman lasers can now cover the spectrum from the visible to the near IR ($\sim 4\,\mu m$).

Prospect of Far-off Resonance Mode-locked Raman Laser

After several years of research on CW Raman lasers, here we make a mode-locked Raman laser source, starting with a mode-locked diode laser as the pump laser. This is a possible scenario if the pulse circulating within the HFC resonates in such a way that its return to the input mirror is synchronized with the arrival of the next incoming pulse. Since a mode-locked laser can be viewed as a set of coherent CW modes, this condition is met when all the CW modes are simultaneously resonant in the laser cavity. The spectrum of the mode-locked pump and Stokes are shown schematically in figure 1-4.

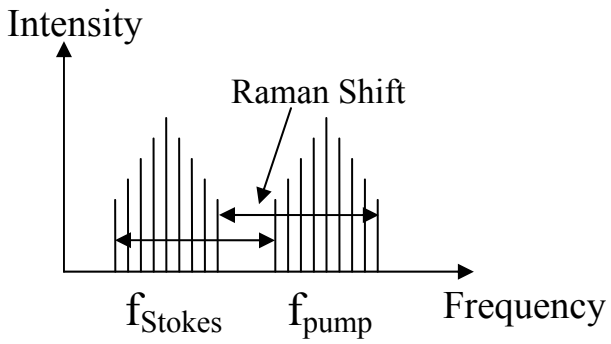

Figure 1-4. Mode-locked Raman laser frequency shift.

This thesis investigated whether such a device could operate with approximately the same average pumping power as a CW Raman laser, even if all the pumping modes were individually below threshold. We were encouraged by the earlier work of J. Rifkin [17], who showed that the correlated Raman gain driven by a multi-longtudinal mode laser can be larger than the gain for a single mode laser because of "collaboration" between the modes by four-wave-mixing processes. However with a mode-locked source, we were not sure if the collaboration would help build up the gain for a particular Stokes

mode. We also wanted to know if all the different Stokes modes --- as well as the residual pump modes –would have the proper phase to yield short pulses after the Raman lasing.

The most challenging part in the experiment was expected to be frequency locking all the longtitudinal modes from the mode-locked laser to the HFC simultaneously. Previous work had shown frequency locking a single laser mode to a HFC could be done successfully. The question was what extra efforts would be needed to lock the mode-locked laser to the Raman cavity? And would the hydrogen dispersion interfere with the locking?

Structure of the Thesis

Chapter 2 reviews the far-off-resonance CW Raman laser theory. We generalize the semiclassical two-level laser system theory from Sargent, Scully and Lamb [18] to a three-level system. With some simplifications appropriate when the pump laser is far-off resonance, the intra-cavity CW pump and Stokes field equations are derived.

In Chapter 3, we change the pump source from CW (single mode) to two in-phase modes and derive the four intra-cavity fields (two pumps and two Stokes) and one coherence equation, and then we study the solutions to these simplified equations. Then we generalize the two-mode case to the general mode-locked case. This theory for a far-off resonance mode-locked Raman laser in H_2 with HFC enhancement is presented here for the first time to the author's knowledge.

Chapter 4 focuses on the Raman experiments. Before taking ML Raman laser data, there are a few preliminary tasks: building a mode-locked ECDL pump source, designing

an optical amplifier to provide more pump power and learning how to frequency lock the ML-ECDL to a HFC. All the details for these steps are given in chapter 4. The CW and ML Raman laser data and analysis based on theoretical simulations and experimental results are also presented in this chapter.

Chapter 5 gives brief concluding remarks. A few appendices such as a method used in the mathematical derivation of the mode-locked Raman equations, Matlab code for the theoretical simulations, the optical amplifier design and the ringdown measurements for the high reflectivity mirrors are included.

References

1. N. Bloembergen, "The stimulated Raman effect," *Am. J. Phys.*, Vol. 35, pp. 989-1023, 1967.

2. E. J. Woodbury and W. K. Ng, Proc. IRE 50, 2347, 1962.

3. D. C. Mac Pherson, R. C. Swanson and J. L. Carlsten, "Stimulated Raman Scattering in the Visible with a Multipass Cell," *IEEE J. of Quant. Elec*. Vol. 25, No. 7, pp. 1741-1746, 1989.

4. G. Eckhardt, R. W. Hellwarth, F. J. McClung, S. E. Schwarz, and D. Weiner and E. J. Woodbury, "Stimulated Raman scattering from organic liquids," *Phys. Rev. Lett.,* Vol. 9, p. 455, 1962.

5. R. W. Minck, R. W. Terhune, and W. G. Rado, "Laser-stimulated Raman effect and resonant four-photon interactions in gases H_2, D_2, and CH_4," *Appl. Phys. Lett.,* Vol. 3, p. 181, 1963.

6. M. Geller, D. P. Bortfeld, and W. R. Sooy, "New Woodbury-Raman laser materials," *Appl. Phys. Lett.,* Vol. 3, p. 36, 1963.

7. J. H. Dennis and P.E. Tannenwald, "Stimulated raman emission at 90° to the Ruby Beam," *App. Phys. Lett.*, Vol. 5, No. 3, pp. 58-60, 1964.

8. R. Max, U. Huber, I. Abdul-Halim, J. Heppner, Y. Ni, G. Willenberg and C. O. Weiss, "Far-infrared CW Raman and laser gain of ^{14}NH3,"*IEEE J. of Quant. Elec*. Vol. 17, No. 6, pp. 1123-1128, 1981.

9. M. Poelker and P. Kumer, "Sodium-Raman laser: direct measurements of the narrow-band Raman gain," *Opt. Lett.,* Vol. 17, p. 399, 1992.

10. G. Grynber, E. Giacobino and F. Biraben, *Opt. Commun*. Vol. 36, p. 403, 1981.

11. S. N. Jabr, *Opt. Lett*., Vol. 12, p. 690, 1987.

12. P. Franke, a. feirisch, F. Riehle, K. Zhao and J. helmcke, Appl. Opt., Vol. 28, p. 3702, 1989.

13. X. W. Xia, W. J. Sandle, R. J. Ballagh and D. M. Warrington, *Opt. Commun*., Vol. 96, p. 99, 1993.

14. J. K. Brasseur, K. S. Repasky, and J. L. Carlsten, "Continuous-wave Raman laser in H_2," *Opt. Lett.,* Vol. 23, pp. 367-369, 1998.

15. P. A. Roos, J. K. Brasseur, and J. L. Carlsten, "Diode-pumped nonresonant continuous-wave Raman laser in H_2 with resonant optical feedback stabilization," *Opt. Lett.,* Vol. 15, pp. 1130-1132, 1999.

16. L. S. Meng, K. S. Repasky , P. A. Roos, and J. L. Carlsten, "Widely tunable continuous-wave Raman laser in diatomic hydrogen pumped by an external-cavity diode laser," *Opt. Lett.,* Vol. 25, pp. 472-474, 2000.

17. J. Rifkin, M. L. Bernt, D. Macpherson and J. L. Carlsten, "Gain enhancement in z XeCl-pumped Raman amplifier," *J. Opt. Soc. Am. B,* Vol. 5, No. 8, pp.1607-1612 1988.

18. M. Sargent, M. O. Scully and W. E. Lamb, "Semiclasscial Laser Theory," in *Laser Physics,* (Addison-Wesley 1974), pp.96-114.

CHAPTER 2

REVIEW OF THE FAR-OFF RESONANCE SEMICLASSICAL CW RAMAN LASER THEORY

Introduction of the Semiclassical Laser Theory

Semiclassical laser theory is a combination of quantum theory and classical electromagnetic theory. Maxwell's equations are used to describe the electromagnetic radiation in the laser cavity, and the quantum mechanical density matrix is introduced to obtain the macroscopic polarization of the medium from the individual dipole moments.

The laser self-consistency diagram (Figure 2-1) by Lamb [1] is used to explain the semiclassical theory. Here the field $\tilde{E}(\tilde{r},t)$ induces electric-dipole moments P_i in the medium based on quantum mechanics. Then these dipole moments are summed to yield the macroscopic polarization of the medium $\tilde{P}(\tilde{r},t)$, which acts as a source in Maxwell's equations. The condition of self-consistency requires that the assumed field $\tilde{E}(\tilde{r},t)$ equal the resulting field $\tilde{E}'(\tilde{r},t)$.

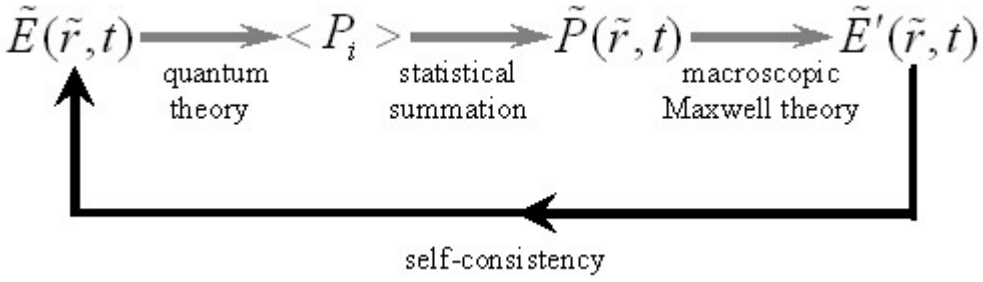

Figure 2-1. Semiclassical self-consistency diagram.

This section presents a general derivation of the semi-classical laser theory. Following the development of Lamb [1], we start with a classical treatment of the fields, beginning with Maxwell's equations and assuming the laser fields are resonant cavity modes. Then, based on the quantum theory from Sakurai [2], density matrix is introduced to describe the medium's macroscopic polarization. Since the density matrix depends on the laser fields, the self-consistency loop can be completed by plugging the polarization into the field equations derived from Maxwell's equations, as done in the next section for the generalized case of the CW Raman laser.

Electromagnetic Field Equations (Maxwell's Equations)

Let us start with Maxwell's equations in mks units [1]:

$$\begin{cases} \nabla \bullet \tilde{D} = 0 & \nabla \times \tilde{E} = -\dfrac{\partial \tilde{B}}{\partial t} \\ \nabla \bullet \tilde{B} = 0 & \nabla \times \tilde{H} = \tilde{J} + \dfrac{\partial \tilde{D}}{\partial t} \end{cases}, \tag{2.1}$$

where

$$\tilde{D} = \varepsilon_0 \tilde{E} + \tilde{P}, \quad \tilde{B} = \mu_0 \tilde{H}, \quad \tilde{J} = \sigma \tilde{E}. \tag{2.2}$$

In hydrogen gas, an isotropic medium, we can assume $\nabla \bullet \tilde{P} = 0$ [Appendix A]. Also the variations in the field intensity transverse to the laser axis are slowly varying on the scale of an optical wavelength, so we will neglect the x and y derivatives, that is $\nabla^2 \tilde{E} = -\dfrac{\partial^2 \tilde{E}}{\partial z^2}$ [Appendix B]. Then substituting Eq. (2.2) with the time derivative of the curl H equation into the curl of the curl E equation

$$\frac{\partial}{\partial t}(\nabla \times \tilde{H}) = \frac{\partial \tilde{J}}{\partial t} + \frac{\partial^2 \tilde{D}}{\partial t^2} = \sigma \frac{\partial \tilde{E}}{\partial t} + \frac{\partial^2}{\partial t^2}(\varepsilon_0 \tilde{E} + \tilde{P}) \tag{2.3}$$

$$\begin{aligned} \frac{\partial}{\partial t}(\nabla \times \tilde{H}) &= \frac{1}{\mu_0}\frac{\partial}{\partial t}(\nabla \times \tilde{B}) = \frac{1}{\mu_0}(\nabla \times \frac{\partial}{\partial t}\tilde{B}) = -\frac{1}{\mu_0}(\nabla \times \nabla \times \tilde{E}) \\ &= -\frac{1}{\mu_0}[\nabla^2 \tilde{E} + \nabla(\nabla \bullet \tilde{E})] = -\frac{1}{\mu_0}[\nabla^2 \tilde{E} + \frac{\nabla \bullet \tilde{D} - \nabla \bullet \tilde{P}}{\varepsilon_0}] \\ &= -\frac{1}{\mu_0}\nabla^2 \tilde{E} = \frac{1}{\mu_0}\frac{\partial^2 \tilde{E}}{\partial z^2} \end{aligned} \tag{2.4}$$

$$\frac{1}{\mu_0}\frac{\partial^2 \tilde{E}}{\partial z^2} = \sigma \frac{\partial \tilde{E}}{\partial t} + \frac{\partial^2}{\partial t^2}(\varepsilon_0 \tilde{E} + \tilde{P}) \tag{2.5}$$

Now we have the wave equation

$$-\frac{\partial^2 \tilde{E}}{\partial z^2} + \mu_0 \sigma \frac{\partial \tilde{E}}{\partial t} + \mu_0 \varepsilon_0 \frac{\partial^2 \tilde{E}}{\partial t^2} = -\mu_0 \frac{\partial^2 \tilde{P}}{\partial t^2} \tag{2.6}$$

where the second term of the Eq. (2.6) accounts for cavity losses. Suppose that the field in the laser cavity is represented in the form

$$\tilde{E}(z,t) = \tfrac{1}{2}\sum_n E_n(t)\exp(-i\omega_n t)U_n(z) + c.c. \tag{2.7}$$

where, for example, in a simple Fabry-Perot laser cavity, the axial variation of the nth mode (a standing wave) is given by

$$U_n(z) \propto \sin(K_n z) = \sin(\frac{n\pi}{L} z) \tag{2.8}$$

With this field, the induced polarization can be expressed as

$$\tilde{P}(z,t) = \tfrac{1}{2}\sum_n P_n(t)\exp(-i\omega_n t)U_n(z) + c.c, \tag{2.9}$$

where $P_n(t)$ is the complex, slowly varying component of the polarization for mode n.

$$\frac{\partial^2 \tilde{E}}{\partial z^2} = \tfrac{1}{2}\sum_n -(K_n)^2 E_n(t)\exp(-i\omega_n t)U_n(z) + c.c. \tag{2.10}$$

$$\frac{\partial \tilde{E}}{\partial t} = \tfrac{1}{2}\sum_n (-i\omega_n)E_n(t)\exp(-i\omega_n t)U_n(z) + \tfrac{1}{2}\sum_n \dot{E}_n(t)\exp(-i\omega_n t)U_n(z) + c.c, \tag{2.11}$$

$$\begin{aligned}\frac{\partial^2 \tilde{E}}{\partial t^2} = {} & \tfrac{1}{2}\sum_n (-i\omega_n)^2 E_n(t)\exp(-i\omega_n t)U_n(z) + \sum_n (-i\omega_n)\dot{E}_n(t)\exp(-i\omega_n t)U_n(z) \\ & + \tfrac{1}{2}\sum_n \ddot{E}_n(t)\exp(-i\omega_n t)U_n(z) + c.c,\end{aligned} \tag{2.12}$$

$$\begin{aligned}\frac{\partial^2 \tilde{P}}{\partial t^2} = {} & \tfrac{1}{2}\sum_n (-i\omega_n)^2 P_n(t)\exp(-i\omega_n t)U_n(z) + \sum_n (-i\omega_n)\dot{P}_n(t)\exp(-i\omega_n t)U_n(z) \\ & + \tfrac{1}{2}\sum_n \ddot{P}_n(t)\exp(-i\omega_n t)U_n(z) + c.c.\end{aligned} \tag{2.13}$$

Because $E_n(t)$ and $P_n(t)$ vary little in an optical frequency period ($\dot{E}_n(t) \ll \omega_n E_n(t)$, $\ddot{E}_n(t) \ll \omega_n^2 E_n(t)$, $\dot{P}_n(t) \ll \omega_n P_n(t)$ and $\ddot{P}_n(t) \ll \omega_n^2 P_n(t)$) and the losses are small ($\sigma \ll 1$) and the medium dilute, we neglect terms containing $\ddot{E}_n(t)$, $\sigma\dot{E}_n(t)$, $\dot{P}_n(t)$ and $\ddot{P}_n(t)$. Then, substituting Eq. (2.10)-(2.13) into the wave equation(2.6), for each operation frequency of ω_n , we have

$$E_n(t)[(K_n)^2 - i\omega_n\mu_0\sigma - \mu_0\varepsilon_0\omega_n^2] - 2i\omega_n\mu_0\varepsilon_0\dot{E}_n(t) = \mu_0\omega_n^2 P_n(t). \tag{2.14}$$

In the experiments, the operating frequencies (pump and Stokes) will be on cavity resonances and we have $\omega_n = 2\pi\frac{nc}{2L}$, $K_n = \frac{n\pi}{L}$ (Eq.(2.8)) and $c^2 = \frac{1}{\mu_0\varepsilon_0}$, so $(K_n)^2 = \mu_0\varepsilon_0\omega_n^2$. This leaves us with the following equation

$$\dot{E}_n(t) = -(\frac{\sigma}{2\varepsilon_0})E_n(t) - \frac{\omega_n}{2i\varepsilon_0}P_n(t), \tag{2.15}$$

where the subscript, n, will be used to denote either the pump or the Stokes field. The first term on the right side accounts for the losses in the medium due to the material conductivity. While in our case, there is no free charge or conductivity in the laser cavity, we take the first loss term from the cavity mirrors. Later, we will have different expression for the loss coefficient. The second term describes gain from the induced polarization.

Polarization of the Medium

Now we need to find an expression for polarization to plug into Eq. (2.15). This will be done by introducing the density matrix [1, 2]. We start with the density matrix for the two-level system.

The interaction of radiation with matter involves a Hamiltonian H, given by the sum of an unperturbed term H_0 and an interaction energy V:

$$\hat{H} = \hat{H}_0 + \hat{V} \tag{2.16}$$

The corresponding Schrödinger equation is

$$\frac{d}{dt}|\psi(t)\rangle = -\frac{i}{\hbar}\hat{H}|\psi(t)\rangle = -\frac{i}{\hbar}(\hat{H}_0 + \hat{V})|\psi(t)\rangle. \tag{2.17}$$

The Schrödinger picture state vector is written as

$$|\psi(t)\rangle = \sum_j c_j(t)|j\rangle \tag{2.18}$$

where the $c_j(t)$ are the probability amplitudes for the corresponding basis state vectors $|j\rangle$. The equation of motion for the $c_j(t)$ is

$$\dot{c}_j = -i\omega_j c_j - \frac{i}{\hbar}\sum_k \langle j|\hat{V}|k\rangle c_k. \tag{2.19}$$

The density matrix for a two-level system is

$$\rho = \begin{pmatrix} \rho_{aa} & \rho_{ab} \\ \rho_{ba} & \rho_{bb} \end{pmatrix}. \tag{2.20}$$

where a(b) represents the upper (lower) state and the components of the matrix are

$$\begin{aligned} &\rho_{aa} \equiv c_a c_a^*, \text{ probability of being in upper state,} \\ &\rho_{bb} \equiv c_b c_b^*, \text{ probability of being in lower state,} \\ &\rho_{ab} \equiv c_a c_b^*, \text{ proportional to the complex dipole moment,} \\ &\rho_{ba} \equiv c_b c_a^* \equiv \rho_{ab}^*; \end{aligned} \tag{2.21}$$

The polarization (i.e. the total dipole moment per unit volume) is given in terms of the off-diagonal elements of the density matrix by [3]

$$\tilde{P}(z,t) = N < \tilde{\mu} >= N\mathrm{Tr}(\hat{\rho}\hat{\mu}) = N(\mu_{ab}\rho_{ba} + \mu_{ba}\rho_{ab}) \tag{2.22}$$

where N is the number density of molecules and $\hat{\mu} = -e\hat{r}$ denotes the electric dipole moment operator of the atom. We also have defined the polarization as in Eq.(2.9), so we have

$$\frac{1}{2}\sum_n P_n(t)\exp(-i\omega_n t)U_n(z) = N\mu_{ab}\rho_{ba}. \tag{2.23}$$

The laser cavity spatial modes are orthogonal:

$$\int_0^L U_n(z)U_m^*(z)dz = \begin{cases} 0 & n \neq m \\ \int_0^L |U_n(z)|^2 \, dz & n = m \end{cases} \tag{2.24}$$

We use the orthogonality property by multipling $U_m^*(z)$ on both sides of Eq. (2.23) and then integrating over cavity length, yielding

$$P_m(t) = 2N \exp(i\omega_m t) \frac{\int_0^L \mu_{ab}\rho_{ba}U_m^*(z)dz}{\int_0^L U_m(z)U_m^*(z)dz}. \quad (2.25)$$

So far we have used classical electromagnetic theory to describe the laser cavity fields and also used quantum mechanics to get the polarization, which is dependent on the off-diagonal component of density matrix. Since the density matrix depends on the laser field, we can now complete the self-consistency loop of figure 2-1 by plugging Eq. (2.25) into Eq. (2.15).

CW Raman Laser Theory

Now we extend the semiclassical laser theory to get the CW Raman laser intracavity field equations. In this complicated dynamics, the pump and Stokes fields will interact with each other, giving us a set of coupled equations for the fields. We start with field's equation Eq.(2.15), then find the polarization of the Raman medium and plug it into Eq.(2.15); finally the coupled Raman laser field's equations can be achieved. This has been previously done by J. Brasseur [4], L. Meng [5] and P. Roos [6].

Raman Process Equation Derivation

To find an expression for the polarization of the Raman medium, let us start with an energy level diagram. Figure 2-2 shows the energy levels of H_2 with a 800 nm laser used for the CW pump not drawn to scale. The ground state and first electronic state are labeled |1> and |2> respectively. The dashed line represents the virtual level. The pump and Stokes radiation fields will both be far-off resonance from the |2> ↔ |1> and |2> ↔

|3> transitions. The transition between levels |3> and |1> is electric dipole forbidden. The pump laser establishes a polarization of the medium between the ground state |1> and the electronic state |2>, which in turn produces a Stokes that establishes a polarization of the medium between the electronic state |2> and the vibrational state |3>. δ is the detuning between the virtual level to the first excited state |2> and it is much larger than the pump frequency, so we consider this Raman process far-off-resonance.

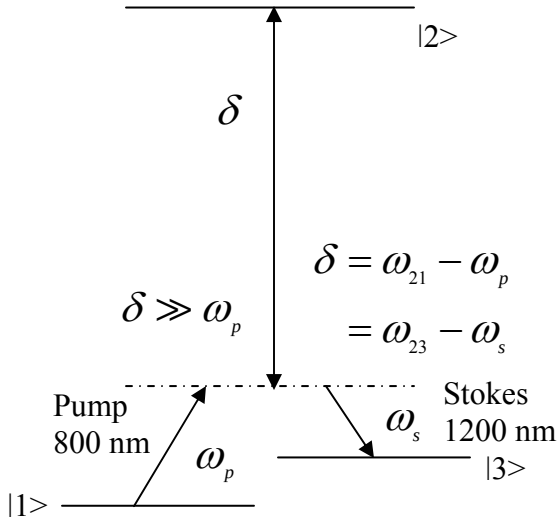

Figure 2-2. Energy level diagram of H_2.

We assume that the interaction energy can be described in the electric dipole approximation, in which case the interaction Hamiltonian has the form

$$\hat{V}(t) = -\hat{\mu} \bullet \tilde{E}(t). \tag{2.26}$$

where $\tilde{E}(t) = \tilde{E}_p(t) + \tilde{E}_s(t) = \frac{1}{2}(E_p e^{-i\omega_p t} + E_p^* e^{i\omega_p t}) + \frac{1}{2}(E_s e^{-i\omega_s t} + E_s^* e^{i\omega_s t})$. The molecular wave functions in a diatomic molecule like H_2 corresponding to states |1>, |2> and |3> have definite parity so that the diagonal matrix elements of $\hat{\mu}$ vanish (i.e. $\mu_{11} = \mu_{22} = \mu_{33} = 0$) and, hence, $V_{11} = V_{22} = V_{33} = 0.$ And since |3> ↔ |1> is forbidden, $\mu_{31} = \mu_{13}^* = 0$ and $V_{31} = V_{13}^* = 0$. So the nonvanishing elements of $\hat{V}$ are

$$V_{21} = V_{12}^* = -\mu_{21}\tilde{E}(t) \text{ and } V_{23} = V_{32}^* = -\mu_{23}\tilde{E}(t), \tag{2.27}$$

Now we introduce the density matrix for our three-level problem

$$\hat{\rho} = \begin{bmatrix} \rho_{11} & \rho_{12} & \rho_{13} \\ \rho_{22} & \rho_{22} & \rho_{23} \\ \rho_{31} & \rho_{32} & \rho_{33} \end{bmatrix} \tag{2.28}$$

where $\rho_{nm} = \rho_{mn}^*$. The time evolution of the density matrix [3] is given

$$\dot{\rho}_{nm} = -(i\omega_{nm} + \frac{1}{T_{2(nm)}})\rho_{nm} - \frac{i}{\hbar}\sum_{\alpha}^{1,2,3}(V_{n\alpha}\rho_{\alpha m} - \rho_{n\alpha}V_{\alpha m}), \tag{2.29}$$

with the condition

$$\rho_{11} + \rho_{22} + \rho_{33} = 1 \tag{2.30}$$

and $T_{2(nm)}$ is dipole moment dephasing time between states |n> and |m>.Based on the Eq.(2.29), the coherence equations can be written

$$\begin{aligned} \dot{\rho}_{21} &= -(i\omega_{21} + \frac{1}{T_{2(21)}})\rho_{21} - \frac{i}{\hbar}[V_{21}(\rho_{11} - \rho_{22}) + V_{23}\rho_{31}] \\ &= -(i\omega_{21} + \frac{1}{T_{2(21)}})\rho_{21} + \frac{i}{\hbar}\mu_{21}\tilde{E}(\rho_{11} - \rho_{22}) + \frac{i}{\hbar}\mu_{23}\tilde{E}\rho_{31} \end{aligned} \tag{2.31}$$

$$\begin{aligned}\dot{\rho}_{23} &= -(i\omega_{23} + \frac{1}{T_{2(23)}})\rho_{23} - \frac{i}{\hbar}[V_{23}(\rho_{33} - \rho_{22}) + V_{21}\rho_{13}] \\ &= -(i\omega_{23} + \frac{1}{T_{2(23)}})\rho_{23} + \frac{i}{\hbar}\mu_{23}(\rho_{33} - \rho_{22})\tilde{E} + \frac{i}{\hbar}\mu_{21}\rho_{31}^{*}\tilde{E}\end{aligned} \tag{2.32}$$

$$\begin{aligned}\dot{\rho}_{31} &= -(i\omega_{31} + \frac{1}{T_{2(31)}})\rho_{31} - \frac{i}{\hbar}[V_{32}\rho_{21} - V_{21}\rho_{32}] \\ &= -(i\omega_{31} + \frac{1}{T_{2(31)}})\rho_{31} + \frac{i}{\hbar}\mu_{23}^{*}\rho_{21}\tilde{E} - \frac{i}{\hbar}\mu_{21}\rho_{23}^{*}\tilde{E}\end{aligned} \tag{2.33}$$

By introducing the slowly varying quantities σ_{21}, σ_{23} and σ_{31}, defined by $\rho_{21}(t) = \sigma_{21}(t)e^{-i\omega_p t}$, $\rho_{23}(t) = \sigma_{23}(t)e^{-i\omega_s t}$ and $\rho_{31}(t) = \sigma_{31}(t)e^{-i(\omega_p - \omega_s)t}$, then the slowly varying part coherence equations can be expressed as

$$\dot{\sigma}_{21} = [-i(\omega_{21} - \omega_p) - \frac{1}{T_{2(21)}}]\sigma_{21} + e^{i\omega_p t}\frac{i}{\hbar}\mu_{21}(\rho_{11} - \rho_{22})\tilde{E} + e^{i\omega_p t}\frac{i}{\hbar}\mu_{23}\rho_{31}\tilde{E} \tag{2.34}$$

$$\dot{\sigma}_{23} = [-i(\omega_{23} - \omega_s) - \frac{1}{T_{2(23)}}]\sigma_{23} + e^{i\omega_s t}\frac{i}{\hbar}\mu_{23}(\rho_{33} - \rho_{22})\tilde{E} + e^{i\omega_s t}\frac{i}{\hbar}\mu_{21}\rho_{31}^{*}\tilde{E} \tag{2.35}$$

$$\begin{aligned}\dot{\sigma}_{31} = \{-i[\omega_{31} - (\omega_p - \omega_s)] - \frac{1}{T_{2(31)}}\}\sigma_{31} + e^{i(\omega_p - \omega_s)t}\frac{i}{\hbar}\mu_{23}^{*}\rho_{21}\tilde{E} \\ -e^{i(\omega_p - \omega_s)t}\frac{i}{\hbar}\mu_{21}\rho_{23}^{*}\tilde{E}\end{aligned} \tag{2.36}$$

Now what we have the expression for the density matrix, we can return to the field and polarization equation. The polarization can be written in terms of the density matrix as

$$\tilde{P}(z,t) = N < \tilde{\mu} >= N\mathrm{Tr}(\hat{\rho}\hat{\mu}) = N(\rho_{21}\mu_{12} + \rho_{23}\mu_{32}) + c.c \tag{2.37}$$

and the complex, slowly varying envelope of the polarization for mode n becomes

$$P_n(t) = 2N \exp(i\omega_n t) \frac{\int_0^L (\rho_{21}\mu_{12} + \rho_{23}\mu_{32}) U_n^*(z) dz}{\int_0^L U_n(z) U_n^*(z) dz}, \tag{2.38}$$

an obvious generalization of (2.25). Because $\rho_{21}(\rho_{23})$ has the same spatial dependence as the pump (Stokes) field, only one term survives the spatial integration for either pump or Stokes polarization

$$\begin{aligned} P_p(t) &= 2N exp[i(\omega_p t)] \frac{\int_0^L U_p(z) U_p^*(z) dz}{\int_0^L U_p(z) U_p^*(z) dz} \mu_{12}\rho_{21} \\ &= 2N exp(i\omega_p t)\mu_{12}\rho_{21} \\ &= 2N\mu_{21}^*\sigma_{21}, \end{aligned} \tag{2.39}$$

$$\begin{aligned} P_s(t) &= 2N exp[i(\omega_s t)] \frac{\int_0^L U_s(z) U_s^*(z) dz}{\int_0^L U_s(z) U_s^*(z) dz} \mu_{32}\rho_{23} \\ &= 2N exp(i\omega_s t)\mu_{32}\rho_{23} \\ &= 2N\mu_{23}^*\sigma_{23} \end{aligned} \tag{2.40}$$

Inserting Eqs. (2.39) and (2.40) into Eq.(2.15) gives the intra-cavity field's equation

$$\dot{E}_p(t) = -(\frac{\sigma_p}{2\varepsilon_0})E_p(t) + \frac{i\omega_p}{2\varepsilon_0} 2N\mu_{21}^*\sigma_{21} + K(t) \tag{2.41}$$

$$\dot{E}_s(t) = -(\frac{\sigma_s}{2\varepsilon_0})E_s(t) + \frac{i\omega_s}{2\varepsilon_0} 2N\mu_{23}^*\sigma_{23} \tag{2.42}$$

where K(t) accounts for the transmission of the pump field into the HFC.

So the CW Raman process can be described with the following set of couopled ordinary differential equations [7]:

$$\dot{E}_p(t) = -(\frac{\sigma_p}{2\varepsilon_0})E_p(t) + \frac{i\omega_p}{2\varepsilon_0} 2N\mu_{21}^*\sigma_{21} + K(t) \tag{2.43}$$

$$\dot{E}_s(t) = -(\frac{\sigma_s}{2\varepsilon_0})E_s(t) + \frac{i\omega_s}{2\varepsilon_0} 2N\mu_{23}^*\sigma_{23} \tag{2.44}$$

$$\begin{aligned}\dot{\sigma}_{21} &= [-i(\omega_{21}-\omega_p)-\gamma_{21}]\sigma_{21} + e^{i\omega_p t}\frac{i}{\hbar}\mu_{21}(\rho_{11}-\rho_{22})\tilde{E} \\ &+ e^{i\omega_p t}\frac{i}{\hbar}\mu_{23}\sigma_{31}e^{-i(\omega_p-\omega_s)t}\tilde{E}\end{aligned} \tag{2.45}$$

$$\begin{aligned}\dot{\sigma}_{23} &= [-i(\omega_{23}-\omega_s)-\gamma_{23}]\sigma_{23} + e^{i\omega_s t}\frac{i}{\hbar}\mu_{23}(\rho_{33}-\rho_{22})\tilde{E} \\ &+ e^{i\omega_s t}\frac{i}{\hbar}\mu_{21}\sigma_{31}^*e^{i(\omega_p-\omega_s)t}\tilde{E}\end{aligned} \tag{2.46}$$

$$\begin{aligned}\dot{\sigma}_{31} &= \{-i[\omega_{31}-(\omega_p-\omega_s)]-\gamma_{31}\}\sigma_{31} + e^{i(\omega_p-\omega_s)t}\frac{i}{\hbar}\mu_{23}^*\sigma_{21}e^{-i\omega_p t}\tilde{E} \\ &- e^{i(\omega_p-\omega_s)t}\frac{i}{\hbar}\mu_{21}\sigma_{23}^*e^{i\omega_s t}\tilde{E}\end{aligned} \tag{2.47}$$

Where $\gamma_{mn} \equiv \frac{1}{T_{2(mn)}}$ is the dipole moment dephasing rate. It is not easy to solve those differential equations, even numerically. Luckily, a couple of approximations can be made for this system. We are going to go through these step by step in the following section.

Far-off Electronic Resonance and
Ground State Non-Depletion Approximation

The first approximation that will be made is that the pump laser is far off electronic resonance or $\omega_{21} \gg \omega_p$. The energy from the ground state to the first excited electronic state in H_2 is about 84,800 cm^{-1} which is about seven times larger than the pump laser's wave number of 12,000 cm^{-1}. As a result, the population in the excited state (level |2>) can be assumed to be zero and all the interactions related with level |2>) are

considered to zero too, so $\rho_{22} = \dot{\rho}_{22} = 0$. Also the slowly varying part of the coherences with level 2 will not be affected by the laser interaction, so $\dot{\sigma}_{21} = \dot{\sigma}_{23} = 0$.

The next approximation that will be made is that the ground-state is not depleted. The following calculation will show why it is safe to think so. At 10 atm. of H_2, the density is approximately 2.7×10^{20} molecules/cm^3. A Raman cell with 50 cm radius of curvature mirrors spaced by 17.78 cm gives an interaction volume through one focus of approximately of 0.02 cm^3, so the average number of molecules in the interaction volume is about 6×10^{18}. If all these molecules yielded Stokes photons within the $\sim 40\mu s$ lifetime of the vibrational state, we would have 25 kW of Stokes power, which exceeds the 10mW Stokes output expected from the cavity by 6 orders of magnitude. This means that most of the molecules are in the ground-state or the ground-state is not depleted. So $\rho_{11} - \rho_{33}$ is set to one. Also we have $\rho_{11} - \rho_{22} = 1$ and $\rho_{22} - \rho_{33} = 0$.

Simplified Intra-cavity Raman Fields' Equation

With those approximations ($\dot{\sigma}_{21} = \dot{\sigma}_{23} = 0$), we can write σ_{21} and σ_{23} in terms of σ_{31} by setting the left side of Eq. (2.45)and (2.46) to be zero, yielding

$$\begin{aligned}\sigma_{21} &= \frac{ie^{i\omega_p t}\tilde{E}}{\hbar}\left[\frac{\mu_{21} + \mu_{23}\sigma_{31}e^{-i(\omega_p-\omega_s)t}}{i(\omega_{21}-\omega_p)+\gamma_{21}}\right] \\ &\approx \frac{ie^{i\omega_p t}\tilde{E}}{\hbar}\left[\frac{\mu_{21} + \mu_{23}\sigma_{31}e^{-i(\omega_p-\omega_s)t}}{i(\omega_{21}-\omega_p)}\right] \\ &= \frac{ie^{i\omega_p t}\tilde{E}}{\hbar}\left[\frac{\mu_{21} + \mu_{23}\sigma_{31}e^{-i(\omega_p-\omega_s)t}}{i\delta}\right]\end{aligned} \tag{2.48}$$

$$\begin{aligned}\sigma_{23} &= \frac{ie^{i\omega_s t}e^{i(\omega_p-\omega_s)t}\tilde{E}}{\hbar}\frac{\mu_{21}\sigma_{31}^{*}}{i(\omega_{23}-\omega_s)+\gamma_{23}} \\ &\approx \frac{ie^{i\omega_s t}e^{i(\omega_p-\omega_s)t}\tilde{E}}{\hbar}\frac{\mu_{21}\sigma_{31}^{*}}{i(\omega_{23}-\omega_s)} \\ &= \frac{ie^{i\omega_s t}e^{i(\omega_p-\omega_s)t}\tilde{E}}{\hbar}\frac{\mu_{21}\sigma_{31}^{*}}{i\delta}\end{aligned} \tag{2.49}$$

where $\delta = (\omega_{21}-\omega_p) \gg \gamma_{21}$ and $\delta = (\omega_{23}-\omega_s) \gg \gamma_{23}$ as shown in figure 2-2 because of far-off-resonance. We insert these into Eq. (2.47) to get an equation for σ_{31},

$$\begin{aligned}\dot{\sigma}_{31} &= \{-i[\omega_{31}-(\omega_p-\omega_s)]-\gamma_{31}\}\sigma_{31} + e^{i(\omega_p-\omega_s)t}\frac{i}{\hbar}\mu_{23}^{*}\sigma_{21}e^{-i\omega_p t}\tilde{E} \\ &\quad -e^{i(\omega_p-\omega_s)t}\frac{i}{\hbar}\mu_{21}\sigma_{23}^{*}e^{i\omega_s t}\tilde{E} \\ &= \{-i[\omega_{31}-(\omega_p-\omega_s)]-\gamma_{31}\}\sigma_{31} + e^{i(\omega_p-\omega_s)t}\frac{i}{\hbar}\mu_{23}^{*}e^{-i\omega_p t}\tilde{E}\frac{ie^{i\omega_p t}\tilde{E}}{\hbar} \\ &\quad [\frac{\mu_{21}+\mu_{23}\sigma_{31}e^{-i(\omega_p-\omega_s)t}}{i\delta}] - e^{i(\omega_p-\omega_s)t}\frac{i}{\hbar}\mu_{21}e^{i\omega_s t}\tilde{E} \\ &\quad (\frac{ie^{i\omega_s t}e^{i(\omega_p-\omega_s)t}\tilde{E}}{\hbar}\frac{\mu_{21}\sigma_{31}^{*}}{i\delta})^{*} \\ &= \{-i[\omega_{31}-(\omega_p-\omega_s)]-\gamma_{31}\}\sigma_{31} + i(\tilde{E})^2 e^{i(\omega_p-\omega_s)t}\frac{\mu_{23}^{*}\mu_{21}}{\hbar^2\delta} \\ &\quad +i(\tilde{E})^2\sigma_{31}[\frac{(\mu_{23}^{*}\mu_{23}-\mu_{21}^{*}\mu_{21})}{\hbar^2\delta}]\end{aligned} \tag{2.50}$$

Here $\mu_{23}^{*}\mu_{23} \approx \mu_{21}^{*}\mu_{21}$ and $\sigma_{31} \ll 1$ [5], so the last term on the right side of Eq. (2.50) is relatively small compared with the second term. Then the σ_{31} (coherence) equation becomes

$$\begin{aligned}\dot{\sigma}_{31} &= \{-i[\omega_{31}-(\omega_p-\omega_s)]-\gamma_{31}\}\sigma_{31}+i(\tilde{E})^2 e^{i(\omega_p-\omega_s)t}\frac{\mu_{23}^*\mu_{21}}{\hbar^2\delta} \\ &= \{-i[\omega_{31}-(\omega_p-\omega_s)]-\gamma_{31}\}\sigma_{31}+i\frac{\mu_{23}^*\mu_{21}}{4\hbar^2\delta}e^{i(\omega_p-\omega_s)t} \\ &[E_p^2 e^{-i2\omega_p t}+E_pE_p^*+E_pE_s e^{-i(\omega_p+\omega_s)t}+E_pE_s^* e^{-i(\omega_p-\omega_s)t} \\ &+E_p^*E_p+(E_p^*)^2 e^{i2\omega_p t}+E_p^*E_s e^{i(\omega_p-\omega_s)t}+E_p^*E_s^* e^{i(\omega_p+\omega_s)t} \\ &+E_sE_p e^{-i(\omega_p+\omega_s)t}+E_sE_p^* e^{i(\omega_p-\omega_s)t}+E_s^2 e^{-i2\omega_s t}+E_sE_s^* \\ &+E_s^*E_p e^{-i(\omega_p-\omega_s)t}+E_s^*E_p^* e^{i(\omega_p+\omega_s)t}+E_sE_s^*+(E_s^*)^2 e^{i2\omega_s t}]\end{aligned} \tag{2.51}$$

The general solution to Eq.(2.51) shows that the significant terms are those with variations slower than or comparable to γ_{31} (Appendix C). Therefore, we will safely drop all the terms that oscillate at ω_p, ω_s or $\omega_p-\omega_s$ because even at high pressures, γ_{31} will never be comparable to an optical frequency. We can then simplify Eq. (2.51) to:

$$\begin{aligned}\dot{\sigma}_{31} &= [i\Delta-\gamma_{31}]\sigma_{31}+i\frac{\mu_{23}^*\mu_{21}}{4\hbar^2\delta}e^{i(\omega_p-\omega_s)t}[E_pE_s^* e^{-i(\omega_p-\omega_s)t}+E_s^*E_p e^{-i(\omega_p-\omega_s)t}] \\ &= [i\Delta-\gamma_{31}]\sigma_{31}+i\frac{\mu_{23}^*\mu_{21}}{2\hbar^2\delta}E_s^*E_p \\ &= [i\Delta-\gamma_{31}]\sigma_{31}+ig_{31}E_s^*E_p\end{aligned} \tag{2.52}$$

where $\Delta \equiv (\omega_p-\omega_s)-\omega_{31}$ and $g_{31}\equiv\frac{\mu_{23}^*\mu_{21}}{2\hbar^2\delta}$. For simplicity, in the remaining discussion and simulations we set $\Delta\approx 0$ or $\omega_{31}\approx\omega_p-\omega_s$, assuming that the two-photon Raman detuning is zero. The HFC intra-cavity fields (E_p and E_s) buildup time is ~μs, which is about 3 orders of magnitude slower than coherence decay time ($\gamma_{31}\sim GHz$), so the coherence is well established in the CW Raman regime. Then Eq. (2.52) is set to zero and σ_{31} can be easily solved:

$$\sigma_{31} = \frac{ig_{31}E_s^* E_p}{\gamma_{31}} \tag{2.53}$$

Inserting the coherence expression (2.53) into Eqs.(2.48) and (2.49), then the field Eqs. (2.43) and(2.44), we can get the CW Raman intra-cavity fields' time evolution equation:

$$\dot{E}_p = -\tfrac{1}{2}\left(\tfrac{\sigma_s}{\varepsilon_0}\right)E_p + ig_p\sigma_{31}E_s + K(E_{p_{in}},t) \tag{2.54}$$

$$\dot{E}_s = -\tfrac{1}{2}\left(\tfrac{\sigma_s}{\varepsilon_0}\right)E_s + ig_s\sigma_{31}^* E_p \tag{2.55}$$

where $g_p \equiv \dfrac{\omega_p N\mu_{21}^*\mu_{23}}{2\varepsilon_0\hbar\delta}$ and $g_s \equiv \dfrac{\omega_s N\mu_{23}^*\mu_{21}}{2\varepsilon_0\hbar\delta}$. Here we also neglect terms [Appendix C] oscillating faster than the cavity lost rate, which is on the order of 10^5, as shown later. Finally inserting Eq.(2.53) into the last two fields' equations, we get a set of pump and Stokes intra-cavity field equations describing the CW Raman laser with an established coherence

$$\dot{E}_p = -L_pE_p - \frac{g_pg_{31}}{\gamma_{31}}\left|E_s\right|^2 E_p + K(E_{p_{in}},t) \tag{2.56}$$

$$\dot{E}_s = -L_sE_s + \frac{g_sg_{31}}{\gamma_{31}}\left|E_p\right|^2 E_s \tag{2.57}$$

where $L_{p(s)} = \frac{1}{2}\frac{\sigma_{p(s)}}{\varepsilon_0}$ represents the cavity loss for pump and Stokes wavelengths and g_sg_{31} represents the gain for Stokes growth.

In this chapter, we first introduced the semiclassical laser theory and then used this theory to derive the far-off resonance CW Raman laser intra-cavity fields' equations.

Here we only deal with one pump and one Stokes mode. In the next chapter, we will extend the work to multiple pump and Stokes modes.

References

1. M Sargent, M. O. Scully and W. E. Lamb, "Semiclassical Laser Theory," in *Laser Physics,* (Addison-Wesley 1974), pp.96-114.

2. J. J. Sakurai, *Modern Quantum Mechanics,* (Addison-Wesley 1994).

3. Robert W. Boyd, "Nonlinear Optics in the Two-Level Approximation," in *Nonlinear Optics*, (Academic Press 2003), pp. 261-310.

4. J. K. Brasseur, Ph.D. thesis, "Construction and noise studies of a continuous wave Raman laser," Physics Department, Montana State University, pp. 19-31. November (1998).

5. L. Meng, Ph.D. thesis, "Continuous-wave Raman Laser in H_2: Semiclassical theory and diode-pumping Experiments," Physics Department, Montana State University, August (2002).

6. P. Roos, Ph.D. thesis, "The Diode-pumped Continuous-wave Raman Laser: Classical, Quantum and Thermo-optic Fundamentals," Physics Department, Montana State University, October (2002).

7. J. V. Moloney, J.S. Uppal and R.G. Harrison, "Origin of chaotic relaxation oscillations in an optically pumped molecular laser," *Phys. Rev. Lett.,* Vol. 59, pp. 2868-2871 (1997).

CHAPTER 3

SEMICLASSICAL THEORY FOR A FAR-OFF RESONANCE MODE-LOCKED RAMAN LASER

Mode-Locked Laser

A mode-locked (ML) laser is a laser in which multiple phase-locked laser cavity modes oscillate simultaneously, which results in a series of short pules at a repetition rate determined by the round trip time in the cavity. In the frequency domain, a ML laser is made of a series of spectral lines separated by the lasers' repetition rate or the free spectral range of laser cavity and the temporal pulse length is inversly proportional to the range spanned by the spectral lines. The temporal pulse widths vary from picosecond to attoseonds [1-4].

Laser Cavity Modes (Resonator Modes)

The laser is an optical oscillator which, for the simplest case, is made of two flat mirrors on both ends (known as a Fabry-Perot cavity) with a gain medium in between. The gain profile usually has a certain frequency bandwidth (Figure 3-1a), allowing the laser to emit over this bandwidth. When light bounces between the mirrors, the light will interfere with itself constructively or destructively, leading to many different standing waves between the mirrors. For constructive inteference, the allowed waves will have an integral number of half wavelengths between the cavity mirrors. The allowed standing

waves form a set of discrete frequencies, known as the longitudinal modes of the cavity. The frequencies can be calculated by $\upsilon_q = q\frac{c}{2nL}$ (Figure 3-1b), where q is the mode number, c is the speed of the light in vacuum, L is the separation distance between the mirrors and n is the refractive index of the medium. Note that the frequency spacing between adjacent resonator modes is defined as the free spectral range of cavity and calculated as $\upsilon_F = \frac{c}{2nL}$. These longitudinal modes are the only frequencies of light allowed to oscillate in the resonant cavity; all other frequencies of light are suppressed by destructive interference. So the ML laser output spectrum with the consideration of the gain medium bandwith and cavity modes is as shown in figure 1c.

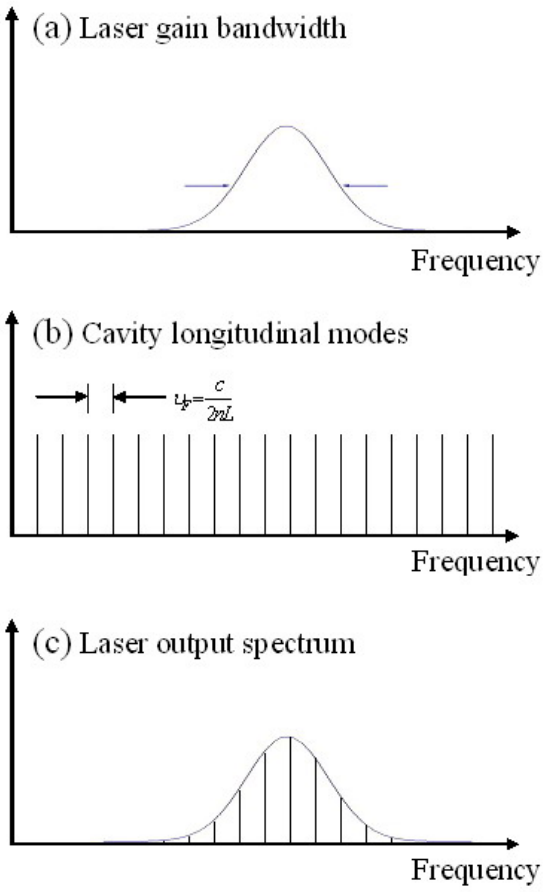

Figure 3-1 (a) Laser gain bandwidth, (b) Cavity longitudinal modes and (c) Laser output spectrum.

Mode Locking Theory

Mode locking is a technique for generating pulsed lasers and is obtained by phase locking the laser cavity modes together [5]. Since the frequency spacing of adjacent cavity modes is constant (it may slightly change because of the variation in *n*), when their phases are locked together, they behave like a periodic function in frequency domain, and therefore form a periodic pulse train in the temporal domain after applying a Fourier transform.

Assuming there are M cavity modes, all plane wave, propagating in the z direction with a velocity of $v = \frac{c}{n}$, we may write the total complex amplitude of the field in the form of:

$$U(z,t) = \sum_{q=-R}^{R} A_q \exp[\, j2\pi\upsilon_q (t - z/v)] \tag{3.1}$$

where $\upsilon_q = \upsilon_0 + q\upsilon_F$ $(q = -R, -R+1, \ldots 0, \ldots R-1, R, \quad M = 2R+1)$ is the frequency of mode q, A_q is the complex amplitude, and υ_0 is the center frequency when $q = 0$. The magnitude $|A_q|$ is determined by the gain profile and mirror loss; here for convenience, we assume that all the $A_q = A$. Substituting all these into Eq. (3.1) provides

$$U(z,t) = A\exp[\, j2\pi\upsilon_0 (t - z/v)] \sum_{q=-R}^{R} \exp[\, j2\pi q\upsilon_F (t - z/v)] \tag{3.2}$$

and by using the arithmetic power series $\sum_{n=1}^{N} ax^n = \frac{a(1-x^N)}{1-x}$, the intensity can be written

$$\begin{aligned} I(z,t) = |U(z,t)|^2 &= A^2 \left| \frac{\exp[\, j2\pi\upsilon_F (t-z/v)(-R)]\{1-\exp[\, j2\pi\upsilon_F (t-z/v)M\,]\}}{1-\exp[\, j2\pi\upsilon_F (t-\frac{z}{v})]} \right|^2 \\ &= A^2 \left| \frac{\exp[\, j2\pi\upsilon_F (t-z/v)(-R)]\exp[\, j\pi\upsilon_F (t-z/v)M\,]}{\exp[\, j\pi\upsilon_F (t-z/v)]} \frac{\{\exp[\, j\pi\upsilon_F (t-z/v)(-M\,)]-\exp[\, j\pi\upsilon_F (t-z/v)M\,]\}}{\{\exp[-j\pi\upsilon_F (t-z/v)]-\exp[\, j\pi\upsilon_F (t-z/v)]\}} \right|^2 \\ &= A^2 \left| \frac{\exp[\, j\pi\upsilon_F (t-z/v)(-2R+2R+1)]}{\exp[\, j\pi\upsilon_F (t-z/v)]} \frac{\sin[\, j\pi\upsilon_F (t-z/v)(M\,)]}{\sin[\, j\pi\upsilon_F (t-z/v)]} \right|^2 \\ &= A^2 \frac{\sin^2[M\pi(t-z/v)/T_F\,]}{\sin^2[\pi(t-z/v)/T_F\,]} \end{aligned} \tag{3.3}$$

where $T_F = \frac{1}{\upsilon_F} = \frac{2nL}{c}$ is the period of pulse train. The shape of mode-locked laser pulse train is therefore dependent on number of modes M. If $\Delta\upsilon = M\upsilon_F$, the pulse width $\tau = T_F / M = 1/\Delta\upsilon$. If M is large, very narrow pulses can be generated. The ratio of the

peak intensity to the average intensity is equal to mode number M, which can be quite large. Figure 3-2 shows three laser modes of equal magnitudes and phase and the intensity of the periodic pulse train resulting from the sum of those modes.

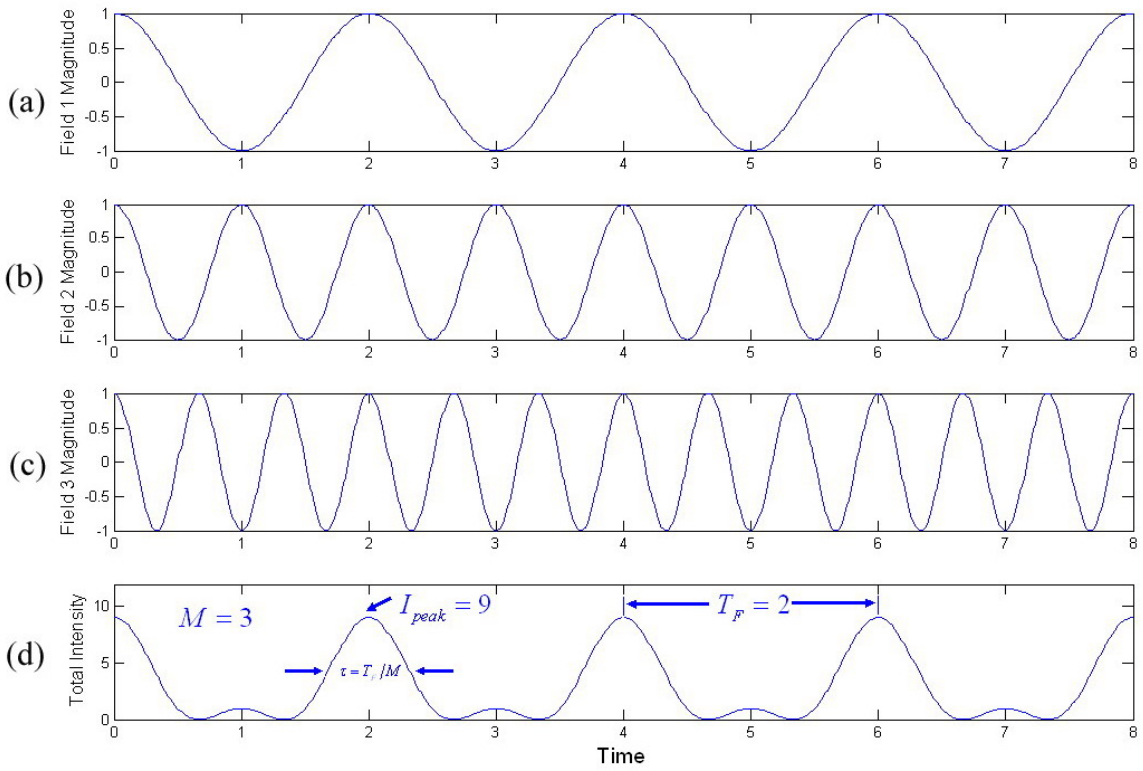

Figure 3-2. (a), (b) and (c) show three phase locked field magnitudes. (d) shows the result of summing then squaring the fields in (a), (b) and (c). In (d), each pulse has a width that is $T_F/3$ and peak intensity 3 times greater than the mean intensity.

Mode Locking Methods

In reality, cavity modes normally oscillate independently (called free-running modes) and the phase of these modes is not locked and may vary randomly due to thermal effects. There are two main methods to produce a ML laser: active and passive.

Active modelocking typically involves using an external signal to induce a modulation of the intra-cavity light, such as periodically modulating the intra-cavity loss with an acousto-optic or electro-optic modulator. Passive modelocking does not use an external signal, but is based on placing some element into the laser cavity which causes self-modulation of the light, such as a saturable absorber. Generally speaking, the active ML pulses are on the order of picoseconds [1,2], while passive ML can generate much shorter pulses, on the order of femtoseconds [3,4]. That is because the saturable absorber can modulate the cavity losses much faster than any electronic modulator.

Active Mode Locking Active mode locking (Figure 3-3) is a technique based on the active modulation of the intra-cavity losses or the round-trip phase change. Intra-cavity loss modulation is also known as amplitude modulation. It can be achieved by putting an acousto-optic [6] or electro-optic modulator [7], Mach-Zehnder integrated-optic modulator [8] or semiconductor electroabsorption modulator [9] inside the laser cavity. If the modulation signal is synchornized with laser cavity round-trip time, the short pulses can be generated. As to the round-trip phase modulation, it is also known as frequency modulation and can be achieved with a pockel cell, which can modulate the phase delay in the crystal. Sometimes both amplitude and frequency modulation are used simultaneously, for example when modulating the diode current in ML external cavity diode laser (ECDL).

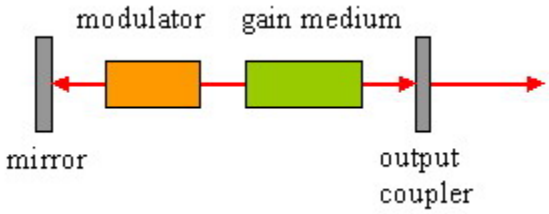

Figure 3-3 Schematic setup of an actively mode-locked laser.

Passive Mode Locking Passive mode locking (Figure 3-4) is a technique based on a saturable absorber inside the laser cavity. A saturable absorber is a medium whose absorption coefficient decreases as the intensity of the light passing through it increases; thus it transmits intense pulses with relatively low absorption and absorbs weak ones. Only when the phases of the different modes are related to each other, they form an intense pulse that can then pass through the saturable absorber medium.

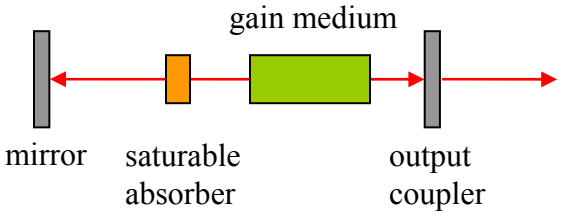

Figure 3-4 Schematic setup of a passively mode-locked laser with saturable absorber.

Mode-Locked Raman Laser Theory Derivation

The output of a ML laser consists of many in-phase continuous-wave (CW) fields. Our physical model of the general detuned (i.e. off resonance with the intermediate electronic state) case in a three-level system pumped with a ML laser is shown in figure 3-5, where n labels either the particular pump or Stokes mode, ω_{pn} is the optical

frequency of pump mode n and ω_{sn} is the optical frequency of Stokes mode n , $\omega_{pn} = \omega_{p1} + (n-1)\Omega$ and $\omega_{sn} = \omega_{s1} + (n-1)\Omega$ and Ω is the repetition rate of mode-locked laser or spacing between adjacent fields (in our case $\Omega \sim GHz$). In this section, for the first time to our knowledge, we develop the far-off resonance mode-locked Raman laser theory based on the semiclassical CW Raman laser theory.

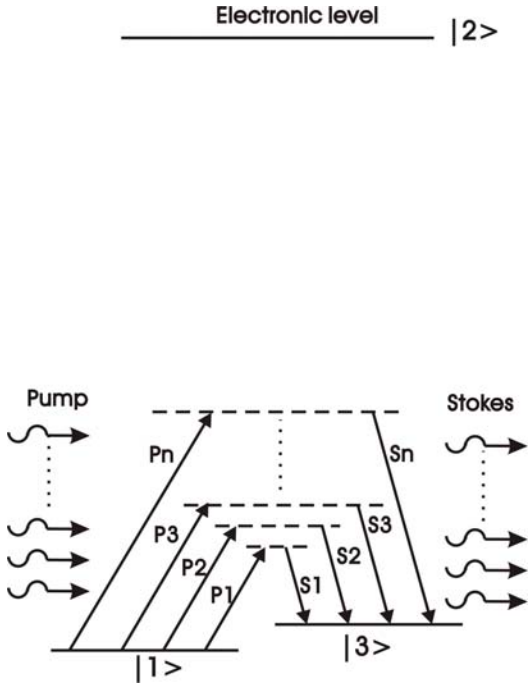

Figure 3-5 Mode-locked laser interaction with hydrogen.

For simplification and clarification, an example with two in-phase pump modes is used in the following mathematical derivation. This two-mode theory can then be extended to multi-mode mode-locked Raman theory. Since the system is far-off

resonance, the rotating wave approximation is not valid. The complex intra-cavity pump and Stokes field amplitudes can be written as:

$$\tilde{E}_p = \tfrac{1}{2}[E_{p1}(t)e^{-i\omega_{p1}t} + E_{p2}(t)e^{-i\omega_{p2}t}] + c.c \tag{3.4}$$

$$\tilde{E}_s = \tfrac{1}{2}[E_{s1}(t)e^{-i\omega_{s1}t} + E_{s2}(t)e^{-i\omega_{s2}t}] + c.c \tag{3.5}$$

where E_{pn} and E_{sn} are the amplitudes of the individual pump and Stokes fields and total electric field $\tilde{E} = \tilde{E}_p + \tilde{E}_s$.

The equations describing Raman laser action are a simple generalization of the semi-classical equations of Sargent, Scully and Lamb to a three-level system [10,11]. Based on the Eqs. (2.43)-(2.47) in chapter 2, the result for the general detuned case is the following set of coupled ordinary differential equations: [10-13]:

$$\dot{E}_{p1} = -L_{p1}E_{p1} + i\tfrac{\omega_{p1}}{\varepsilon_0}N\mu_{21}^{*}\sigma_{21} + K(E_{p_{in(1)}}, t) \tag{3.6}$$

$$\dot{E}_{p2} = -L_{p2}E_{p2} + i\tfrac{\omega_{p2}}{\varepsilon_0}N\mu_{21}^{*}\sigma_{21}e^{i\Omega t} + K(E_{p_{in(2)}}, t) \tag{3.7}$$

$$\dot{E}_{s1} = -L_{s1}E_{s1} + i\tfrac{\omega_{s1}}{\varepsilon_0}N\mu_{23}^{*}\sigma_{23} \tag{3.8}$$

$$\dot{E}_{s2} = -L_{s2}E_{s2} + i\tfrac{\omega_{s2}}{\varepsilon_0}N\mu_{23}^{*}\sigma_{23}e^{i\Omega t} \tag{3.9}$$

$$\begin{aligned}\dot{\sigma}_{21} = {} & [-i(\omega_{21} - \omega_{p1}) - \gamma_{21}]\sigma_{21} + e^{i\omega_p t}\frac{i}{\hbar}\mu_{21}(\rho_{11} - \rho_{22})\tilde{E} \\ & + e^{i\omega_p t}\frac{i}{\hbar}\mu_{23}\sigma_{31}e^{-i(\omega_p - \omega_s)t}\tilde{E}\end{aligned} \tag{3.10}$$

$$\begin{aligned}\dot{\sigma}_{23} = {} & [-i(\omega_{23} - \omega_{s1}) - \gamma_{23}]\sigma_{23} + e^{i\omega_s t}\frac{i}{\hbar}\mu_{23}(\rho_{33} - \rho_{22})\tilde{E} \\ & + e^{i\omega_s t}\frac{i}{\hbar}\mu_{21}\sigma_{31}^{*}e^{i(\omega_p - \omega_s)t}\tilde{E}\end{aligned} \tag{3.11}$$

$$\dot{\sigma}_{31} = \{-i[\omega_{31} - (\omega_{p1} - \omega_{s1})] - \gamma_{31}\}\sigma_{31} + e^{i(\omega_p - \omega_s)t}\frac{i}{\hbar}\mu_{23}^{*}\sigma_{21}e^{-i\omega_p t}\tilde{E} - e^{i(\omega_p - \omega_s)t}\frac{i}{\hbar}\mu_{21}\sigma_{23}^{*}e^{i\omega_s t}\tilde{E} \tag{3.12}$$

where L_{pn} and L_{sn} are the cavity loss constants for pump and Stokes fields; μ_{ij} is the dipole moment matrix element between level i and level j; $E_{pin(n)}$ is the input pump field where $k(t, E_{pin(n)})$ accounts for the pump beam's "leakage" into the cavity; the ρ_{ii} are the diagonal density-matrix elements representing the population of level i; σ_{ij} is the slowly varying part of the off-diagonal density-matrix element ρ_{ij} representing molecular coherences($\sigma_{21} = \rho_{21}\exp(i\omega_{p1}t)$, $\sigma_{23} = \rho_{23}\exp(i\omega_{s1}t)$ and $\rho_{31}(t) = \sigma_{31}(t)e^{-i(\omega_{p1}-\omega_{s1})t}$); ω_{ij} is the frequency difference between level i and j; γ_{ij} is the dephasing rate between level i and level j.

There are several approximations we can use to simplify these differential equations. First, the virtual level is far below the first electronic level 2 as shown in figure 2-2, so the Raman laser is far off the electronic resonance. As such, the coherences associated with level 2 will not be affected by the laser interaction, $\dot{\sigma}_{21} = \dot{\sigma}_{23} = 0$. $\rho_{22} = 0$ because the population of level 2 is not affected either. Another approximation we can make is that the ground-state is not depleted, as is typically the case for CW Raman lasers in H_2 [13, 14]. Thus, $\rho_{11} - \rho_{22} = 1$ and $\rho_{22} - \rho_{33} = 0$. We also set $\rho_{31} = \sigma_{31}e^{-i(\omega_{p1}-\omega_{s1})t}$, where σ_{31} varies much slower than the frequency difference $\omega_{p1} - \omega_{s1}$. With all these

approximations, we can write σ_{21} and σ_{23} in terms of σ_{31} by setting the left side of Eq. (3.10) and (3.11) to be zero and then insert them into Eq. (3.12)to get a equation for σ_{31}:

$$\dot{\sigma}_{31} = \{-i[\omega_{31} - (\omega_{p1} - \omega_{s1})] - \gamma_{31}\}\sigma_{31} + i(\tilde{E})^2 e^{i(\omega_{p1}-\omega_{s1})t} \frac{\mu_{23}^{*}\mu_{21}}{\hbar^2\delta} \tag{3.13}$$

The general solution to Eq.(3.13) shows that the significant terms are as those with variations slower than or comparable to γ_{31} [Appendix C]. Therefore, in using Eq. (3.4) and (3.5), we will safely drop all the terms from $(\tilde{E})^2$ that oscillate at ω_{pn} , ω_{sn} or $\omega_{pn} - \omega_{sn}$ because even at high pressures, γ_{31} will never be comparable to an optical frequency. We can then simplify Eq. (3.13) to:

$$\dot{\sigma}_{31} = (i\Delta - \gamma_{31})\sigma_{31} + ig_{31}(E_{s1}^{*}E_{p1} + E_{s2}^{*}E_{p2} + E_{s1}^{*}E_{p2}e^{-i\Omega t} + E_{s2}^{*}E_{p1}e^{i\Omega t}) \tag{3.14}$$

where $\Delta = (\omega_{pn} - \omega_{sn}) - \omega_{31}$ and $g_{31} \equiv \frac{\mu_{23}^{*}\mu_{21}}{2\hbar^2\delta}$. For simplicity, in the remaining discussion and simulations we set $\Delta \approx 0$ or $\omega_{31} \approx \omega_{pn} - \omega_{sn}$, assuming that the two-photon Raman detuning is zero.

At long times ($t \gg \frac{1}{\gamma_{31}}$), the pump and Stokes fields will approach steady-state, while the coherence σ_{31} continues to oscillate. The solution for the coherence equation at $t \gg \frac{1}{\gamma_{31}}$ (or $e^{-\gamma_{31}t} \to 0$) is simple to obtain from the general solution to a first order linear differential equation:

$$\sigma_{31} = ig_{31}[(E_{s1}^{*}E_{p1} + E_{s2}^{*}E_{p2})(\frac{1}{\gamma_{31}}) + (E_{s1}^{*}E_{p2})(\frac{e^{-i\Omega t}}{\gamma_{31} - i\Omega}) + (E_{s2}^{*}E_{p1})(\frac{e^{i\Omega t}}{\gamma_{31} + i\Omega})] \tag{3.15}$$

Recall that σ_{31} is the slowly varying portion of the total coherence which oscillates near ω_{31}:

$$\begin{aligned}\rho_{31} &= \sigma_{31} e^{-i(\omega_{p1}-\omega_{s1})t} = \sigma_{31} e^{-i\omega_{31}t} \\ &= ig_{31}[(E_{s1}^{*}E_{p1} + E_{s2}^{*}E_{p2})(\frac{e^{-i\omega_{31}t}}{\gamma_{31}}) + (E_{s1}^{*}E_{p2})(\frac{e^{-i(\omega_{31}+\Omega)t}}{\gamma_{31}-i\Omega}) + (E_{s2}^{*}E_{p1})(\frac{e^{-i(\omega_{31}-\Omega)t}}{\gamma_{31}+i\Omega})]\end{aligned} \quad (3.16)$$

The first term on the right-hand side of Eq. (3.16) oscillates at ω_{31} and is completely resonant with the two photon transition. The second and third terms on the right-hand side oscillate at $\omega_{31} \pm \Omega$ and are off-resonance with the two photon transition by an amount equal to $\pm\Omega$. These terms are less strong than the on-resonance term because they fall in the wings of the Lorentzian profile of the Raman gain $\frac{\gamma_{31}}{\gamma_{31}^2+\Omega^2}$ where γ_{31} is the half width half maximum (HWHM) of the Raman gain, and also have a dispersion term proportional to $\frac{\pm i\Omega}{\gamma_{31}^2+\Omega^2}$ that affects the phase associated with them.

As we mentioned earlier, due to being far-off resonance and the ground-state non-depletion, $\dot{\sigma}_{21} = \dot{\sigma}_{23} = 0$, $\rho_{22} = 0$, $\rho_{11} - \rho_{22} = 1$ and $\rho_{22} - \rho_{33} = 0$. With these conditions, set the left side of Eq. (3.10) and (3.11) to be zero and ρ_{21} and ρ_{23} can be expressed in terms of ρ_{31}, then plug these expressions into Eq. (3.6)-(3.9). Basically using the same type of approximations and simplifications used for σ_{31}, Eqs. (3.6)-(3.9) can be simplified to:

$$\dot{E}_{p1} = -L_{p1}E_{p1} - ig_{p1}\rho_{31}e^{i\omega_{31}t}(E_{p1} + E_{p1}e^{-i\Omega t}) + k(t, E_{pin(1)}) \quad (3.17)$$

$$\dot{E}_{p2} = -L_{p2}E_{p2} - ig_{p2}\rho_{31}e^{i\omega_{31}t}(E_{p1}e^{i\Omega t} + E_{p2}) + k(t, E_{pin(2)}) \quad (3.18)$$

$$\dot{E}_{s1} = -L_{s1}E_{s1} - ig_{s1}\left(\rho_{31}e^{i\omega_{31}t}\right)^{*}(E_{p1}+E_{p2}e^{-i\Omega t}) \tag{3.19}$$

$$\dot{E}_{s2} = -L_{s2}E_{s2} - ig_{s2}\left(\rho_{31}e^{i\omega_{31}t}\right)^{*}(E_{p1}e^{i\Omega t}+E_{p2}) \tag{3.20}$$

where all the fast optical frequency oscillation terms are dropped in the field equations because the optical frequency is much larger than $L_{pn(sn)}$, which is about 10^5 when the reflectivity of both the mirrors is about 0.99988 ($L_{pn(sn)} = -(c/2l)\ln(R_{pn(sn)})$ [15, 16]). $g_{pn} \equiv \frac{\omega_{pn}N\mu_{21}^{*}\mu_{23}}{2\varepsilon_0\hbar\delta}$ and $g_{sn} \equiv \frac{\omega_{sn}N\mu_{23}^{*}\mu_{21}}{2\varepsilon_0\hbar\delta}$ are constants related to the Raman gain.

Plugging the solution of ρ_{31} Eq. (3.16) into Eqs. (3.17)-(3.20), gives after dropping all the fast oscillation terms compared with $L_{pn(sn)}$ including $e^{\pm i\Omega t}$ and $e^{\pm i2\Omega t}$:

$$\dot{E}_{p1} = -L_{p1}E_{p1} - g_{p1}g_{31}[\tfrac{E_{s1}(E_{p1}E_{s1}^{*}+E_{p2}E_{s2}^{*})}{\gamma_{31}} + \tfrac{E_{s2}(E_{p1}E_{s2}^{*})}{\gamma_{31}+i\Omega}] + K(E_{p_{in1}},t) \tag{3.21}$$

$$\dot{E}_{p2} = -L_{p2}E_{p2} - g_{p2}g_{31}[\tfrac{E_{s2}(E_{p1}E_{s1}^{*}+E_{p2}E_{s2}^{*})}{\gamma_{31}} + \tfrac{E_{s1}(E_{p2}E_{s1}^{*})}{\gamma_{31}-i\Omega}] + K(E_{p_{in2}},t) \tag{3.22}$$

$$\dot{E}_{s1} = -L_{s1}E_{s1} + g_{s1}g_{31}[\tfrac{E_{p1}(E_{p1}^{*}E_{s1}+E_{p2}^{*}E_{s2})}{\gamma_{31}} + \tfrac{E_{p2}(E_{p2}^{*}E_{s1})}{\gamma_{31}+i\Omega}] \tag{3.23}$$

$$\dot{E}_{s2} = -L_{s2}E_{s2} + g_{s2}g_{31}[\tfrac{E_{p2}(E_{p1}^{*}E_{s1}+E_{p2}^{*}E_{s2})}{\gamma_{31}} + \tfrac{E_{p1}(E_{p1}^{*}E_{s2})}{\gamma_{31}-i\Omega}] \tag{3.24}$$

From these equations, it can be seen there are two ways to generate the desired Stokes mode. For generating Stokes mode 1, the first term in the square brackets on the right-hand side of Eq. (3.23) represents the interaction between pump mode 1 and the on-resonance piece of the coherence, in which $E_{p1}(E_{p1}^{*}E_{s1})$ is the regular Raman process and $E_{p1}(E_{p2}^{*}E_{s2})$ is a four-wave-mixing process (phase mismatch can be ignored [Appendix

D]). The second term in the square brackets results from the interaction between pump mode 2 and the off-resonance piece of the coherence.

Now we can easily extend the two-mode case to the general mode-locked case,

$$\sigma_{31} = ig_{31} \sum_{\beta=-M+1}^{M-1} \frac{e^{i\beta\Omega t} \sum_{\alpha=1}^{M} E_{s\alpha}^{*} E_{p(\alpha-\beta)}}{\gamma_{31}+i\beta\Omega} \tag{3.25}$$

$$\dot{E}_{pn} = -L_{pn}E_{pn} - g_{pn}g_{31} \sum_{\beta=1}^{M} \frac{E_{S\beta} \sum_{\alpha=1}^{M} E_{s\alpha}^{*} E_{p[\alpha-(\beta-n)]}}{\gamma_{31}+i(\beta-n)\Omega} + K(E_{p_{in(n)}}, t) \tag{3.26}$$

$$\dot{E}_{sn} = -L_{sn}E_{sn} + g_{sn}g_{31} \sum_{\beta=1}^{M} \frac{E_{p\beta} \sum_{\alpha=1}^{M} (E_{s[\alpha-(\beta-n)]}^{*} E_{p\alpha})^{*}}{\gamma_{31}+i(\beta-n)\Omega} \tag{3.27}$$

where M is the total number of pump modes and n labels the particular mode under consideration For this case, the coherence is composed of an on-resonance piece and many off-resonance pieces separated from the resonant piece by $\pm\Omega$, $\pm 2\Omega$, $\pm 3\Omega \cdots$. As we mentioned before, both on-resonance and off-resonance coherences can interact with different pump modes to generate the desired Stokes mode.

Mode-Locked Raman Laser Numerical Simulation

In this section, we present calculations relevant to our current experimental work and all the numerical simulations are based on MATLAB programs [Appendix E]. In our experimental set-up, the pump laser wavelength is approximately 800 nm and the Stokes light is at about 1200 nm. The HFC mirrors have a reflectivity (transmissivity) of $R_{pn(sn)}$ =0.99988 ppm ($T_{pn(sn)}$ =40 ppm) at both the pump and Stokes wavelengths, giving a cavity finesse of about 26,000 for both wavelengths. The cavity length is

l=17.78 cm, yielding a free spectral range (FSR) of 844 MHz. In order to simultaneously couple all the pump laser's oscillating modes into the HFC, these modes must also be spaced by 844 MHz (or some integral multiple thereof). Therefore the repetition rate of the mode-locked laser is also Ω=844 MHz.

Due to the difference in wavelength of the various modes, dispersion in the H2 also needs to be considered. With 100 longitudinal modes spanning 84 GHz (or 0.18 nm at the ~800 nm pump wavelength in vacuum), the additional refractive shift in the cavity resonant frequencies between the first and the hundredth mode is only about 0.6 kHz at 10 atm.[17-19] For comparison, the linewidth of the HFC is about 28 kHz. Thus the dispersion due to H_2 can be neglected in this case.

The cavity loss coefficient is defined as $L_{pn(sn)} = -(c/2l)\ln(R_{pn(sn)})$. Over the ~90 GHz range of optical frequencies, L_{pn} and L_{sn} (~10^5 Hz) can be considered the same for all the longitudinal modes. The optical-pumping constant $K(t, E_{pin(n)}) = (c/l)\sqrt{T_{pn}}E_{pin(n)}$ and the Raman gain coefficient $G = (1/8)\gamma_{31}\alpha c(\varepsilon_0/\mu_0)^{1/2}\left(\frac{\lambda_p}{\lambda_p+\lambda_s}\right)$ [13-16, 20], where α=1.5×10^{-11} m/W at 800 nm is the plane-wave gain coefficient [20], $E_{pin(n)}$ is the input pump field amplitude and c is the speed of light in vacuum. Also, we define $g_{pn}g_{31} = \frac{\omega_{pn}}{\omega_{s1}}G$, $g_{sn}g_{31} = \frac{\omega_{sn}}{\omega_{s1}}G$.

In this section, using all the numbers and coefficients mentioned earlier along with τ, the mode-locked pulse duration ($\frac{1}{\tau} \approx M\Omega$), we compare Ω with the dephasing rate γ_{31} in three different regimes: low pressure ($\gamma_{31} \ll \Omega$), high pressure ($\gamma_{31} \gg M\Omega$)

and medium pressure (γ_{31} does not satisfy either $\gamma_{31} \ll \Omega$ or $\gamma_{31} \gg M\Omega$) to determine the Stokes threshold. The dephasing rate γ_{31} is the half width half maximum (HWHM) of the Lorentzian distribution describing Raman gain [21]. The different possible relationships between γ_{31} and Ω are illustrated in figure 3-6.

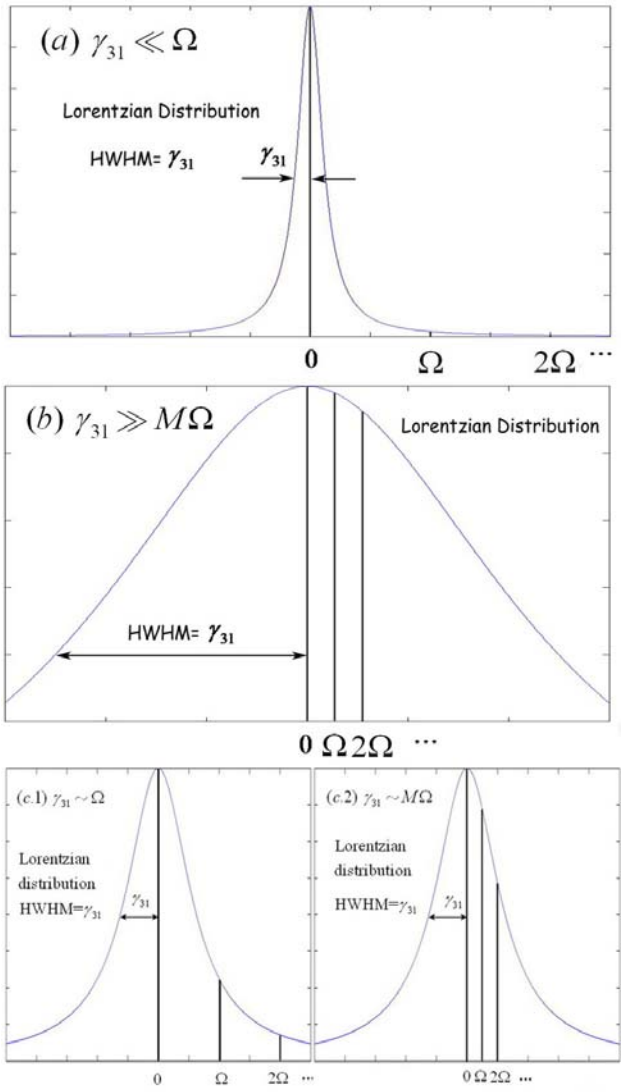

Figure 3-6. Three different regimes in the relation between γ_{31} and Ω. (a)Low pressure ($\gamma_{31} \ll \Omega$), (b) High pressure ($\gamma_{31} \gg M\Omega$) and (c) Medium pressure, two cases: $\gamma_{31} \sim \Omega$ and $\gamma_{31} \sim M\Omega$.

Low pressure ($\gamma_{31} \ll \Omega$)

Mathematically when $\gamma_{31} \ll \Omega < M\Omega \approx \frac{1}{\tau}$, the coherence equation only has the term with γ_{31} as the denominator left and all the other terms with $\gamma_{31} + i\beta\Omega$ as the denominator is much smaller due to the comparatively large Ω in the denominator. Because of the same reason, in Eqs. (3.26)-(3.27), only the terms with $\beta = n$ needs to be kept. So the coherence and field equations can be simplified to:

$$\sigma_{31} = ig_{31} \sum_{\alpha=1}^{M} \frac{E_{s\alpha}^{*} E_{p\alpha}}{\gamma_{31}} \tag{3.28}$$

$$\dot{E}_{pn} = -L_{pn} E_{pn} - g_{pn} g_{31} E_{sn} \sum_{\alpha=1}^{M} \frac{E_{s\alpha}^{*} E_{p\alpha}}{\gamma_{31}} + K(E_{p_{in(n)}}, t) \tag{3.29}$$

$$\dot{E}_{sn} = -L_{sn} E_{sn} + g_{sn} g_{31} E_{pn} \sum_{\alpha=1}^{M} \frac{(E_{s\alpha}^{*} E_{p\alpha})^{*}}{\gamma_{31}} \tag{3.30}$$

Physically when $\gamma_{31} \ll \Omega$, all the off-resonance pieces of the coherence are small compared with the on-resonance piece, as shown in Figure 3-6(a). In other words, the mode-locked temporal pulse width is much shorter than the coherence dephasing time, $\tau \gg \frac{1}{\gamma_{31}}$, and the coherence growth is not fast enough to follow the short pulses. Thus only the average power determines the growth of the coherence and Stokes modes, and the mode-locked case will have the same gain and same threshold as the CW case [14, 15]. Figure 3-7 shows a plot of the average intra-cavity Stokes intensity versus the average input pump intensity for one, two and three in-phase pump modes. For this plot, the following definition has been used for the average intensity $I = |E|^2 = \sum_{n=1}^{M} |E_{(n)}|^2$,

where I is either the input pump or intra-cavity Stokes intensity (I_{pin} or I_s) respectively, E is either the input pump or intra-cavity Stokes field (E_{pin} or E_s) respectively, and the index n represents the nth mode of either field. In this regime, the three curves completely overlap, indicating that the threshold is independent of the number of modes and that the average output is proportional to the square root of the average input pump power [15,16].

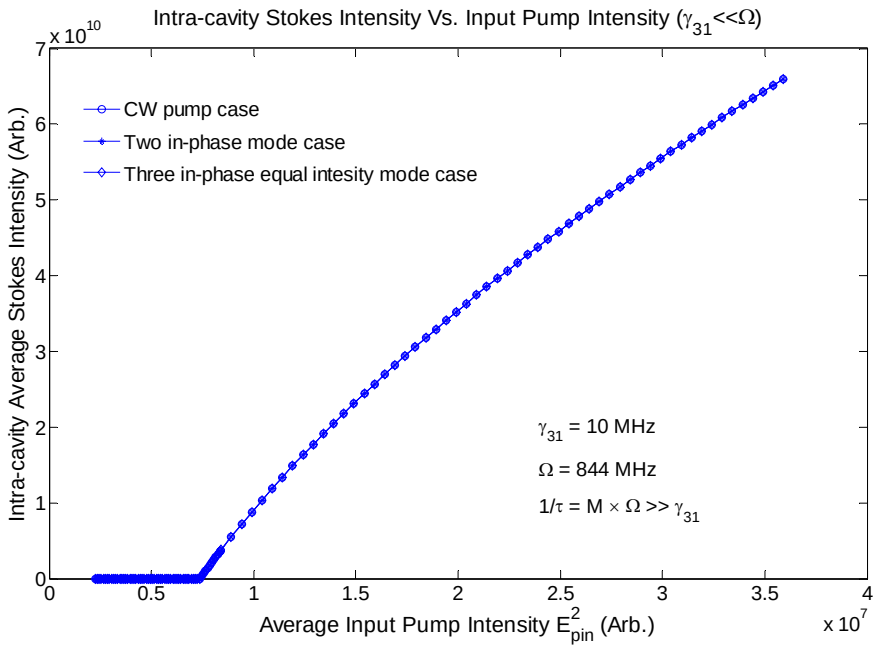

Figure 3-7. Intra-cavity Stokes Intensity versus outside input pump Intensity. In this simulation γ_{31}=10 MHz and Ω=844 MHz. The three curves are totally overlapped, which means in the region where $\gamma_{31} << \Omega$, there is no gain enhancement for the mode-locked case.

We also give plots of the intra-cavity fields' amplitude and phase evolution with equal and unequal amplitudes of the three pump modes in figure 3-8 and figure 3-9. Once the system reaches steady-state, all the Stokes fields' phases have evolved to be in-phase,

so that mode-locked Stokes is generated. With equal amplitude pump modes ($\left|E_{pin1}\right|^2=\left|E_{pin2}\right|^2=\left|E_{pin3}\right|^2=\frac{1}{3}\left|E_{pin}\right|^2$), final Stokes phase is the vectorial summation of all the Stokes fields' initial phases as shown in figure 3-8. If the initial pump modes are different in amplitude the Stokes field's phase evolution will not be a simple vecotrial summation of all the Stokes field's initial phase, but the steady-state average Stokes intensity will be the same as an equal amplitude case, as shown in figure 3-9.

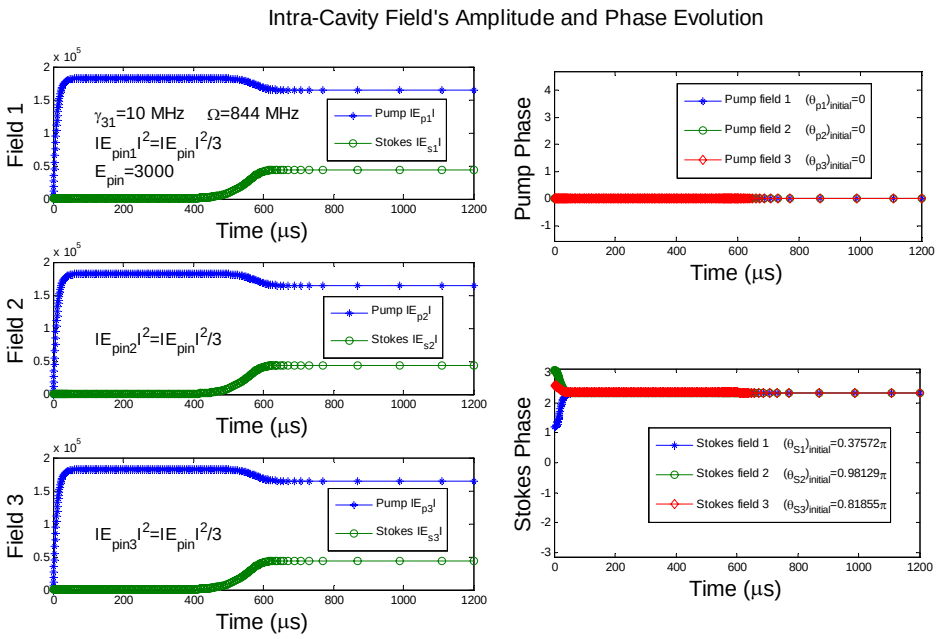

Figure 3-8. Intra-cavity fields' magnitude and phase evolution with three equal in-phase pump modes. Since the pump modes are in-phase, we set $(\theta_{p1})_{initial}=(\theta_{p2})_{initial}=(\theta_{p3})_{initial}=0$ and they remain the same for all the time as seen in the figure. The initial Stokes phases are random, we set $(\theta_{s1})_{initial}=0.3757\pi$, $(\theta_{s2})_{initial}=0.9813\pi$ and $(\theta_{s3})_{initial}=0.8186\pi$. Once the system reaches steady-state, the final phase of Stokes 0.746π is the vectorial summation of all the Stokes initial phases, mode-locked Stokes formed. At steady-state, with $E_{pin}=3000$, the total average Stokes intensity is $I_s=\left|E_{s1}\right|^2+\left|E_{s2}\right|^2+\left|E_{s3}\right|^2=5.78\times10^9$.

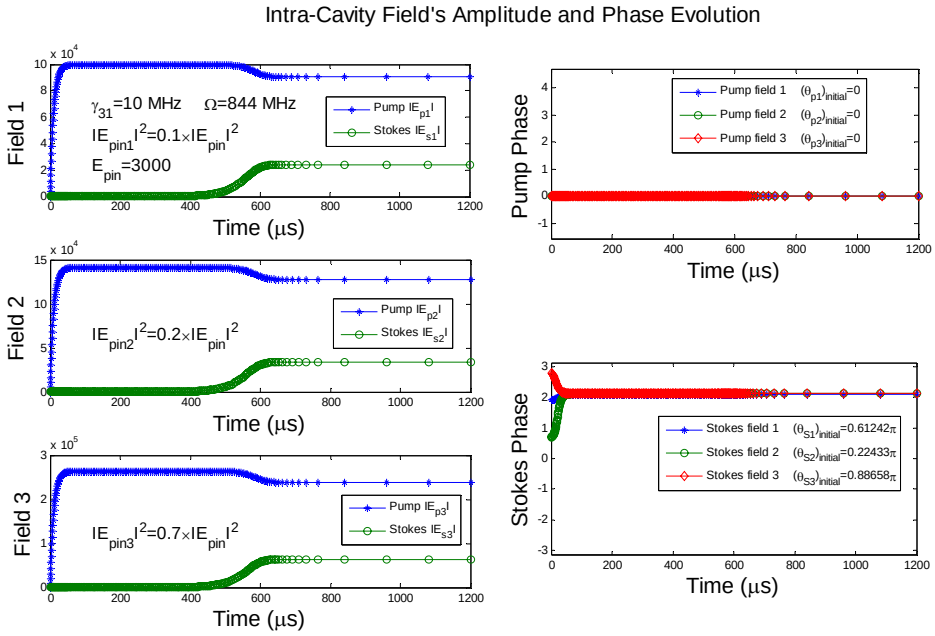

Figure 3-9. Intra-cavity fields' amplitude and phase evolution with three unequal in-phase pump modes. Since the three pump modes are not equal in magnitude, the final Stokes phase is not the vectorial summation of all the initial Stokes phases, but still evolve to the same phase. At steady-state, with $E_{pin} = 3000$, the total average Stokes intensity ($I_s = |E_{s1}|^2 + |E_{s2}|^2 + |E_{s3}|^2 = 5.78 \times 10^9$) is same as previous case.

<u>High pressure</u> ($\gamma_{31} \gg M\Omega$)

Mathematically when $\gamma_{31} \gg M\Omega$, we drop the $i\beta\Omega$ term in the denominator. Thus, the coherence and field equations are simplified to:

$$\sigma_{31} = ig_{31} \sum_{\beta=-M+1}^{M-1} \frac{e^{i\beta\Omega t} \sum_{\alpha=1}^{M} E_{s\alpha}^* E_{p(\alpha-\beta)}}{\gamma_{31}} \tag{3.31}$$

$$\dot{E}_{pn} = -L_{pn} E_{pn} + K(E_{p_{in(n)}}, t) - g_{pn} g_{31} \sum_{\beta=1}^{M} \frac{E_{s\beta} \sum_{\alpha=1}^{M} E_{s\alpha}^* E_{p[\alpha-(\beta-n)]}}{\gamma_{31}} \tag{3.32}$$

$$\dot{E}_{sn} = -L_{sn}E_{sn} + g_{sn}g_{31}\sum_{\beta=1}^{M}\frac{E_{p\beta}\sum_{\alpha=1}^{M}(E^{*}_{s[\alpha-(\beta-n)]}E_{p\alpha})^{*}}{\gamma_{31}} \tag{3.33}$$

Physically when $\gamma_{31} \gg M\Omega$, from the Lorenztian distribution, all the off-resonance pieces of the coherence will contribute about the same as the on-resonance piece as shown in Figure 3-6(b). It also means that the mode-locked pulses are like CW light when compared with the even shorter coherence dephasing time. In other words the coherence growth is fast enough to follow the short pulses. Thus, the high peak power from the mode-locked laser will contribute to the Raman gain. Thus, in the regime of $\gamma_{31} \gg M\Omega$, the mode-locked case will have much smaller average threshold power than the CW case as shown in figure 3-10. But at high input pump power, the CW case has more average Stokes output than mode-locked case, for the following reason. Consider two possible pumping scenarios that have the same average power. The first is a constant input pump with intensity of 1, which produces constant Stokes of intensity of 1. The second is an input pump intensity that is four times bigger but is only on for one-fourth of the time, giving an average input power of 1 as well. However, because for the time it is on, it is four times bigger and because the Stokes average output intensity is proportional to the square root of average input pump intensity, it produces only twice the Stokes power, which when averaged over the time span is 2/4=0.5, less than CW case.

With two equal intensity pump modes, the pulse peak intensity is twice bigger than the average pump intensity for CW case, which should lead to a threshold value that is twice as small. However the ratio between two thresholds shown in figure 3-10 is smaller than 2, at about 1.33. This is because the mode-locked pulse temporal width is

much smaller than the cavity build up time (tens of μs). Therefore the pulses can not build up as high an intra-cavity power as the CW case. In other words, taking into the consideration of the cavity build up time, we expect the threshold for the two equal intensity mode case to not quite be two times smaller than the CW case. If these two modes have unequal intensity, for example, if the two modes' intensities differ by a lot, then the threshold for this two mode case will almost have the same threshold plot as CW case. So in region ($\gamma_{31} \gg M\Omega$), the gain enhancement gets maximized and threshold gets minimized only when the pump modes have same intensity. We also find these three curves cross each other, that is because when the input pump power reaches four times threshold, the conversion efficiency will decrease [22]. The three in-phase equal intensity mode case reaches the threshold first, so the efficiency will decrease first, crossing the other two curves, as shown in the figure 3-10.

In figure 3-11 the time evolution of the pump and Stokes field amplitude and phases can be seen. The Stokes phases all evolve to the same steady-state value, indicative of mode-locked Stokes being generated.

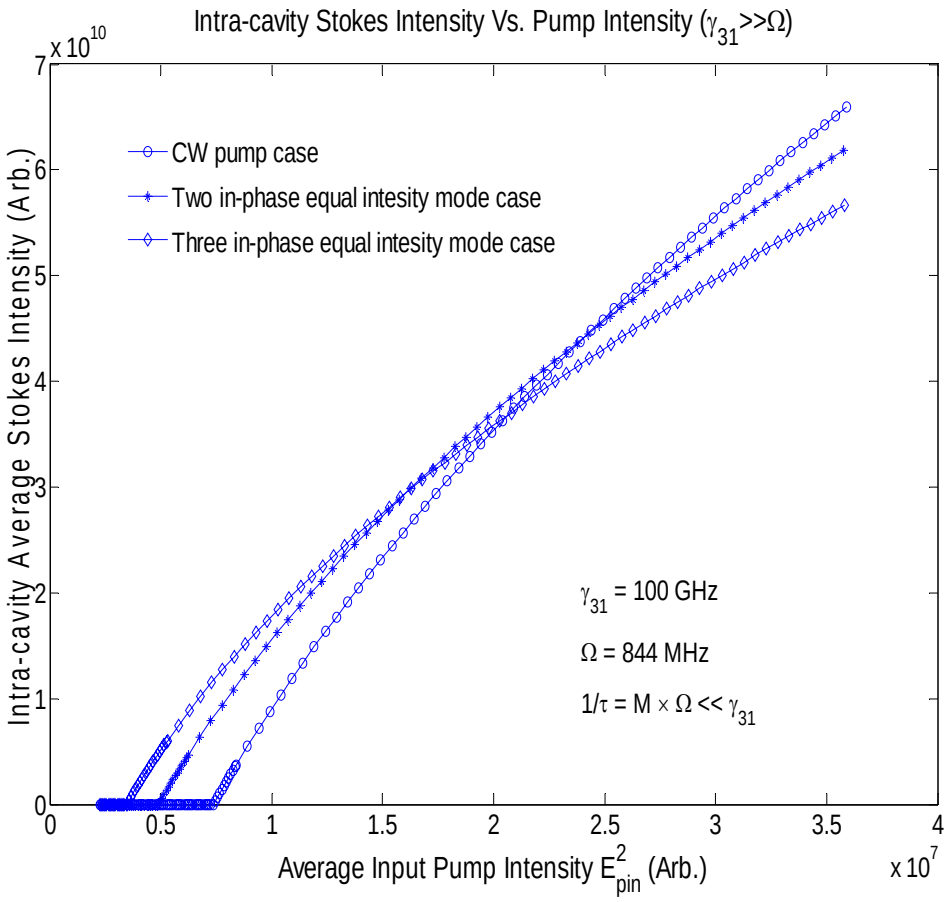

Figure 3-10. Intra-cavity Stokes field magnitudes versus outside input pump field. In this simulation γ_{31}=100 GHz and Ω=844 MHz. It is obvious that more modes give a smaller threshold.

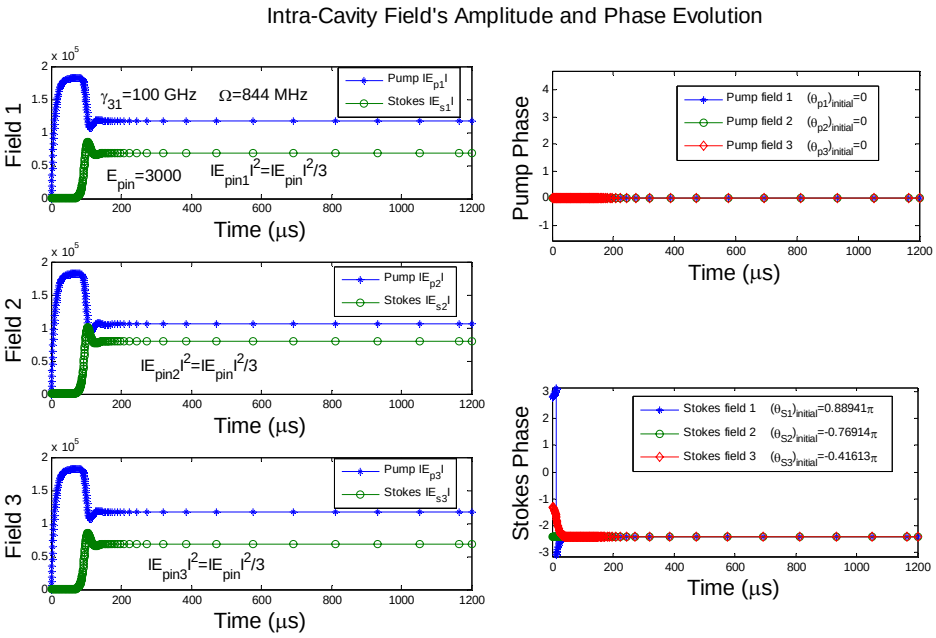

Figure 3-11. Intra-cavity fields' amplitude and phase evolution with three in-phase pump modes. Since the pump modes are in-phase, we set $(\theta_{p1})_{initial} = (\theta_{p2})_{initial} = (\theta_{p3})_{initial} = 0$. The pump phases do not evolve from their initial values. In this example we set the initial random Stokes phases to $(\theta_{s1})_{initial} = 0.8894\pi$, $(\theta_{s2})_{initial} = -0.7691\pi$ and $(\theta_{s3})_{initial} = -0.4161\pi$. The Stokes' phases evolve from their initial value to a final value that is the vectorial summation of the initial Stokes phases because input pump fields have the same amplitude. At steady-state, with $E_{pin} = 3000$, the total average intracavity Stokes intensity is ($I_s = |E_{s1}|^2 + |E_{s2}|^2 + |E_{s3}|^2 = 1.561 \times 10^{10}$).

Medium pressure (from $\gamma_{31} \sim \Omega$ to $\gamma_{31} \sim M\Omega$)

If γ_{31} does not satisfy either $\gamma_{31} \gg \Omega$ or $\gamma_{31} \ll M\Omega$, then this is an intermediate pressure case. From figure 3-6(c.1) and (c.2), some of the off-resonance pieces of coherence will contribute while some of them are too small to contribute to the build-up of the coherence needed in generating Stokes. Thus, the gain is bigger than the low pressure case but smaller than the high pressure case, giving an average threshold that is

smaller than the low pressure case but bigger than the high pressure case as shown in figure 3-12. In this regime, the Stokes phases do not evolve to the same steady-state values and the pump phases evolve slightly away from their initial values, as shown in figure 3-13. This is due to the extra dispersion phase term $\frac{\pm i\beta\Omega}{\gamma_{31}^2+(\beta\Omega)^2}$ introduced from the off-resonance piece of the coherence, which degrades the pulse shape, peak power and Raman gain.

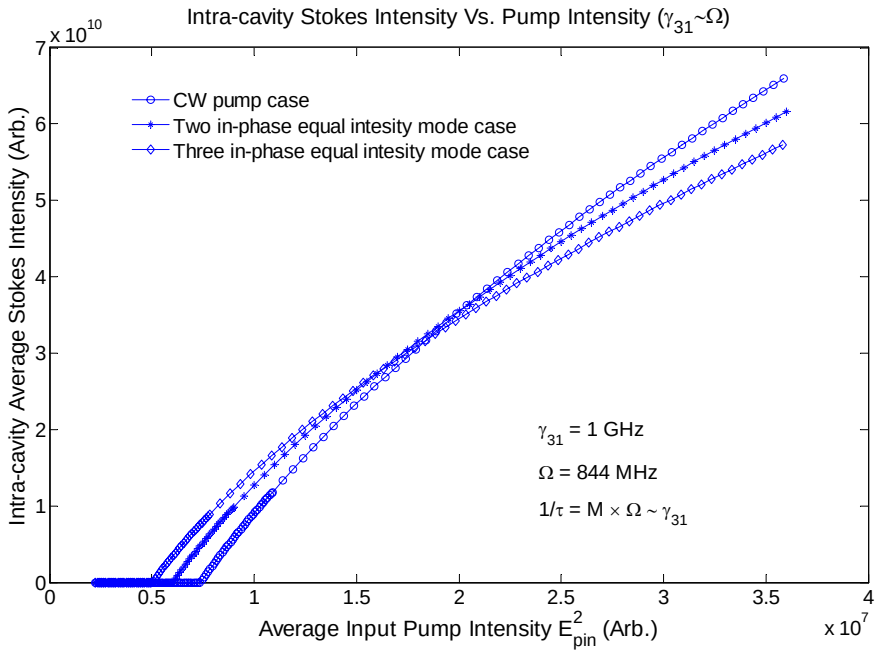

Figure 3-12. Intra-cavity Stokes field versus outside input pump field. In this simulation γ_{31}=1 GHz and Ω=844 MHz. The gain enhancement in this plot is not as big as shown in figure 3-10.

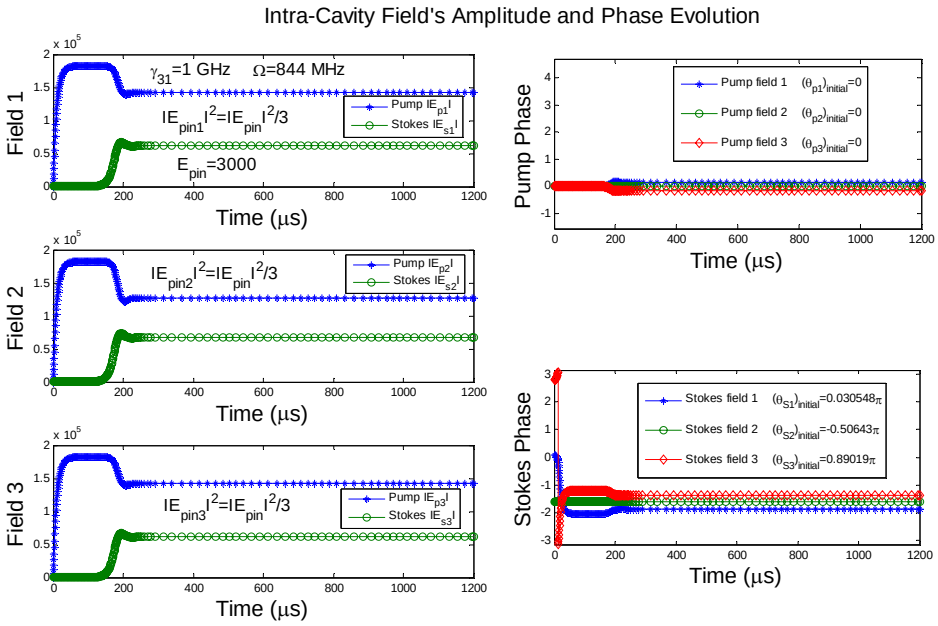

Figure 3-13. Intra-cavity fields' magnitude and phase evolution with three in-phase pump modes. Since pump modes are in-phase, we set $(\theta_{p1})_{initial} = (\theta_{p2})_{initial} = (\theta_{p3})_{initial} = 0$ and they evolve slightly away from their initial values. Here we set the initial random Stokes phases $(\theta_{s1})_{initial} = 0.03\pi$, $(\theta_{s2})_{initial} = -0.506\pi$ and $(\theta_{s3})_{initial} = 0.8902\pi$. When the system reaches steady-state, the Stokes fields are not quite in-phase due to the extra phase terms introduced from the off-resonance pieces of the coherence.

Conclusion of the Simulations

From these numerical calculations, we can tell the Raman gain or threshold for the far-off resonance mode-locked Raman laser in H_2 with HFC enhancement is dependent on the relations between γ_{31} and Ω. In the low-pressure regime ($\gamma_{31} \ll \Omega$), only the on-resonance pieces of coherence contribute to coherence build-up and mode-locked Stokes generation, and the mode-locked pumping will have the same threshold value as CW pumping. When pumping with the average power above threshold, even if

the individual modes from the mode-locked pump source are below threshold; the corresponding Stokes modes can still emit Stokes due to the four-wave-mixing-process.

In the high-pressure regime ($\gamma_{31} \gg M\Omega$), all the on-resonance and off-resonance pieces of coherence contribute about the same to Raman process, providing large gain enhancement to generate mode-locked Stokes and thus significantly lowering the threshold compared with CW pumping.

In the medium-pressure regime, where γ_{31} does not satisfy either $\gamma_{31} \ll \Omega$ or $\gamma_{31} \gg M\Omega$ (i.e. γ_{31} can vary from $\sim\Omega$ to $\sim M\Omega$), besides the on-resonance pieces of the coherence, part of the off-resonance pieces also help to build up the coherence and generate Stokes light, which leads to enhanced gain compared with the low-pressure mode-locked case or CW pumping. Further, for γ_{31} varying from $\sim\Omega$ to $\sim M\Omega$, some extra dispersion terms are introduced from these off-resonance pieces of the coherence, degrading the pulse shape, peak power and Raman gain. Stokes output in this case is "near mode-locked".

References

1. L. E. Hargrove, R. L. Fork, and M. A. Pollack, "Locking of He-Ne laser modes induced by synchronous intracavity modulation", *Appl. Phys. Lett*. 5, p. 4 (1964).

2. Yariv, "Internal modulation in multimode laser oscillators", *J. Appl. Phys*. 36, p. 388 (1965).

3. J. DeMaria, D. A. Stetser, and H. Heynau, "Self mode-locking of lasers with saturable absorbers", *Appl. Phys. Lett*. 8, p. 174 (1966).

4. E. P. Ippen, C. V. Shank, and A. Dienes, "Passive mode locking of the cw dye laser", *Appl. Phys. Lett*. 21, p. 348 (1972).

5. B. E. A. Saleh and M. C. Teich, "Fundamentals of Photonics," (John Wiely & Sons, 1991), pp.531-536.

6. J. M. Harris, R. W. Chrisman, and F. E. Lytle, "Pulse generation in a cw dye laser by mode–locked synchronous pumping", *Appl. Phys. Lett*. 26, p. 16 (1975).

7. B. Pelz, M. K. Schott, and M. H. Niemz, "Electro-optic mode locking of an erbium:YAG laser with a rf resonance transformer", *Appl. Opt.* 33, p. 364 (1994).

8. J. B. Schlager, S. Kawanishi and M. Saruwatari, "Dual wavelength pulse generation fibre ring laser", *Electronics Letters*, Vol. 27, No. 22, p. 2072 (1991).

9. Kenji Sato, Hiroyuki Ishii, Isamu Kotaka, Yasuhiro Kondo and Mitsuo Yamamoto, "Frequency Range Extension of Actively Mode-Locked Lasers Integrated with Electroabsorption Modulators Using Chirped Gratings", *IEEE Journal of Selected Topics in Quantum Electronics,* Vol. 3, No. 2 (1997).

10. Murray Sargent, Marlan O. Scully and Willis E. Lamb, "Semiclassical Laser Theory," in *Laser Physics,* (Addison-Wesley 1974), pp.96-114.

11. Robert W. Boyd, "Nonlinear Optics in the Two-Level Approximation," in *Nonlinear Optics*, (Academic Press 2003), pp. 261-310.

12. J. V. Moloney, J.S. Uppal and R.G. Harrison, "Origin of chaotic relaxation oscillations in an optically pumped molecular laser," *Phys. Rev. Lett*. Vol. 59, 2868-2871 (1997).

13. Jason K. Brasseur, Ph.D. thesis, "Construction and noise studies of a continuous wave Raman laser," Physics Department, Montana State University, pp. 19-31. November (1998).

14. Lei Meng, Ph.D. thesis, "Continuous-wave Raman Laser in H_2: Semiclassical theory and diode-pumping Experiments," Physics Department, Montana State University, pp. 17-22. August (2002).

15. J. K. Brasseur, P. A. Roos, K. S. Repasky and J. L. Carlsten, "Characterization of a continuous-wave Raman laser in H_2", *J. Opt. Soc. Am. B*, Vol. 16, no. 8, pp. 1305-1312 (1999).

16. P. A. Roos, J. K. Brasseur, and J. L. Carlsten, "Diode-pumped, non-resonant, cw Raman laser in H_2 using resonant optical feedback stabilization," *Opt. Lett.* 24, 1130 (1999).

17. W., E. W. "International critical tables of numerical data, physics, chemistry and technology," (Edward Wight), 1881-1934. Vol. 7 pp.11.

18. "*American Institute of Physics Handbook,*" second edition, (McGraw-Hill), pp.6-95.

19. At 10 atm, $\lambda_{p(1)}$ =800 nm, n_1 =1.00127005738702; 100 modes away $\lambda_{p(100)}$ =800.18 nm, n_{100} = 1.00127005036724. $100\times\left[c/\left(2n_1 l\right)-c/\left(2n_{100}l\right)\right]$=0.59 kHz.

20. W. K. Bischel and mark J. Dyer, "Wavelength dependence of the absolute Raman gain coefficient for the Q (1) transition in H_2," *J. Opt. Soc. Am. B*, vol. 3, No. 5, May (1986).

21. W. k. Bischel and Mark J. Dyer, "Temperature dependence of the Raman lindewidth and line shift for the Q (1) and Q (0) transitions in normal and para-H_2," *Phys. Rev. A,* Vol. 33, No. 5, May (1986).

22. J. K. Brasseur, P. Roos, L. Meng and J. L. Carlsten, "Frequency tuning characteristics of a continuous-wave Raman laser in H_2," *J. Opt. Soc. Am. B*, Vol. 17, no. 7, pp. 1229-1232 (2000).

CHAPTER 4

RAMAN LASER EXPERIMENTS

Mode-Locked External Cavity Diode Laser

Introduction to a Diode Laser (Semiconductor Laser)

Figure 4-1 is a simplified diagram of a semiconductor laser. Lasing occurs in the gain region. When a bias current is applied to the structure, holes from the p-region will be injected into the n-region and electrons from the n-region will be injected into the p-region. When holes and electrons are in the same region, crossing the p-n junction, they may recombine by spontaneous emission, emitting a photon with energy equal to the energy difference between the electron and hole states. Spontaneous emission is necessary to initiate laser oscillation, but it is inefficient because the emitted light goes in all directions. Then optical feedback is introduced by using an optical resonator, which is formed by two parallel facets that result from cleaving the substate along crystal planes. With the spontaneous emission, sufficient gain medium and optical feedback, lasing will occur.

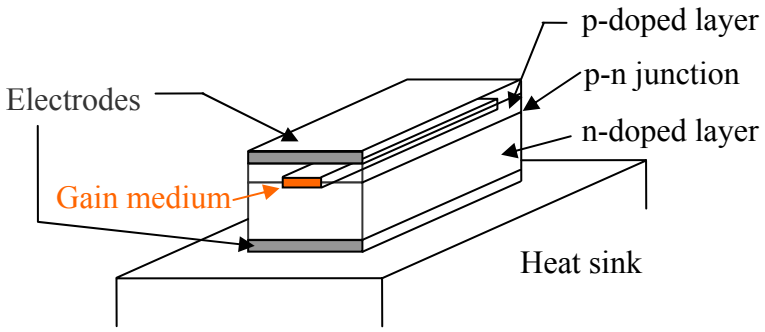

Figure 4-1. Schematic diagram of a smiconductor laser diode.

Introduction to an External Cavity Diode Laser (ECDL)

By changing the diode's temperature or injection current, we can coarsely tune laser diode's frequency over ~nm. While if we want to fine tune or continuously tune the laser diode, some tuning element, and most often, a diffraction grating is used for this purpose. Here we introduce an idea of external cavity diode laser (ECDL).

ECDLs are widely used in many optical experiments because of the advantage of low cost, precise tunability and narrow linedwith. Frequency selective feedback is typically achieved via a diffraction grating in either the Littman-Metcalf [1, 2] (Figure 4-2) or the Littrow [3-5] configuration (Figure 4-3).

In the Littman-Metcalf configuration, first order diffracted light from the grating hits a tuning mirror. Only light that hits the mirror at normal incidence is coupled back to the grating and into the diode. This provides frequency selection. The laser output is the zeroth-order reflection from the grating. In the Littrow configuration, no mirror is needed. Light of some particular wavelength is diffracted in the first order from grating and fed back directly into the diode later. Again, zeroth-order reflected light is the output beam.

General speaking, the Littman configuration is more complicated than the Littrow due to the extra turning mirror, while it normally has less linewidth than the Littrow and also has a fixed output direction [1-5].

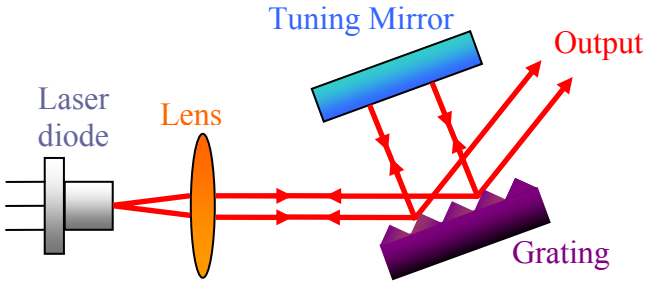

Figure 4-2. Littman-Metcalf configuration.

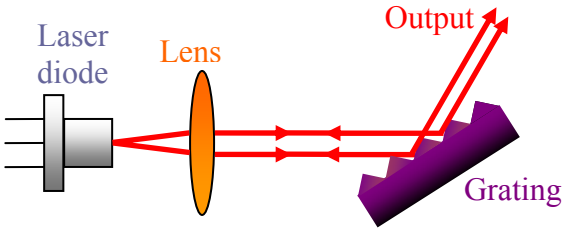

Figure 4-3. Littrow configuration.

Characteristic of Mode-Locked External Cavity Diode Laser

In our ECDL setup, for simplicity, we choose to use Littrow configuration and we also add a turning mirror, which is mounted on a same base as grating, for fixed output direction [3]. Figure 4-4 shows the ML-ECDL setup. The ML-ECDL is in the Littrow configuration, with an 820 nm semiconductor laser at one end and a grating and a turning mirror at the other end. The typical reflectivity of a diode laser's back facet is 95%, and the grating provides approximately 40% feedback to the laser diode, which makes the finesse of this external laser cavity as low as 5. The reflectivity of the diode's front facet is not given from the manufacture data, but we think it is small (<5%) because the wavelength selectivity is determined by the grating feedback and not by the diode facet modes. So we can neglect the cavity inside diode laser. The grating has 600 grooves/mm and the center wavelength of the ECDL can be tuned 25 nm by tilting the grating.

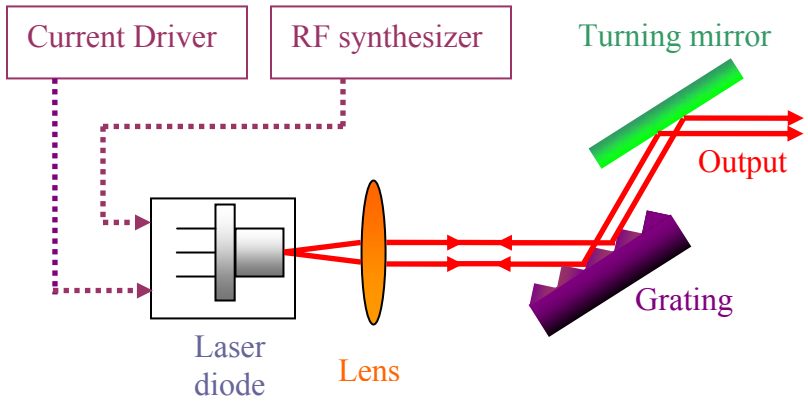

Figure 4-4. ML-ECDL setup. The drive current to the laser diode is the summation of DC current with RF modulation current from a synthesizer.

Mode-locking is achieved by modulating the laser threshold DC current with a 21 dBm RF signal at 840.667 MHz, which is near the free spectral range associated with the 17.78 cm long cavity. To operate the mode locked laser, the modulation frequency does not have to exactly equal the free spectral range (FSR) or fundamental harmonic of the laser external cavity because the laser cavity's finesse is low and the mode-locked laser repetition rate is determined by the modulation frequency instead of the FSR of lasers' external cavity. This flexibility in the modulation frequency is extremely important when we proceed to couple this laser into the HFC.

Figure 4-5 shows the optical spectrum of the continuous wave external cavity diode laser (CW-ECDL) (modulation off) and ML-ECDL (modulation on). The spectral width of ML-ECDL is, as expected, broader than the CW-ECDL. Its full width half maximum (FWHM) is 0.16 nm, which is determined by the depth of the modulation and the number of grooves illuminated on the grating. This width indicates that the ML-ECDL is supporting about 72 longitudinal modes, since the longitudinal modes are separated by 0.00224 nm (～ 840 MHz).

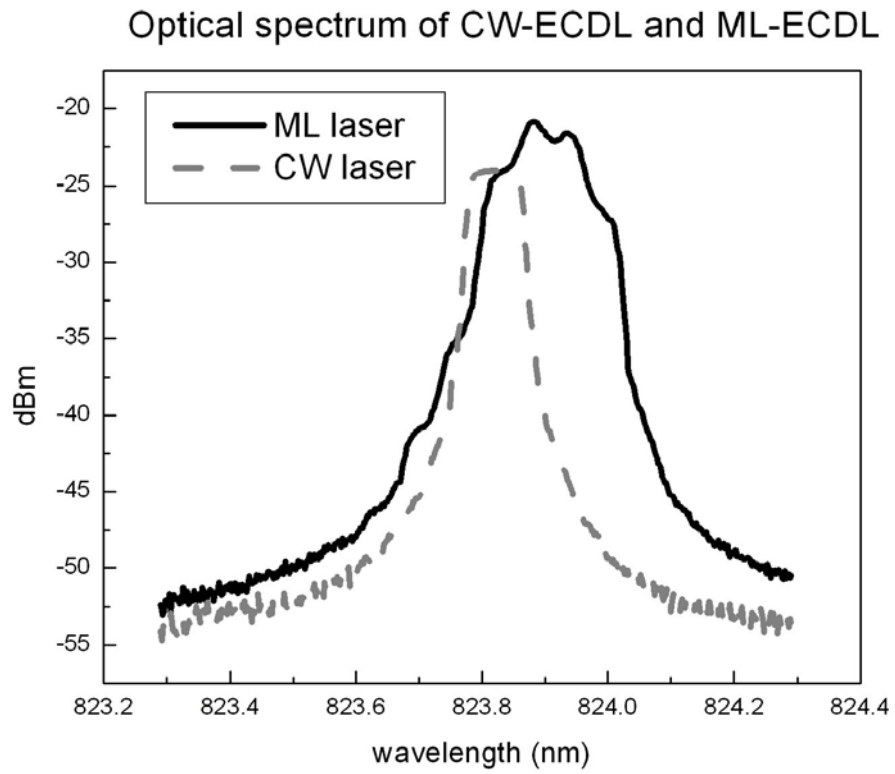

Figure 4-5. Optical spectrum of CW-ECDL and ML-ECDL. The spectrum width of ML-ECDL is wider than CW-ECDL due to more longitudinal modes contributing to the laser output.

We have also measured the temporal pulse width of the mode locked pulse using an autocorrelator, as shown in figure 4-6. The autocorrelator is based on a Michelson interferometer with one arm fixed and the other scanned. Once the two pulses from the two paths overlap perfectly, they generate the highest power of the second harmonic in the KTP crystal. In figure 4-7, the horizontal axis shows the conversion of scanning distance to delay time taking into the consideration of the double passing of the arms of the autocorrelator and also the coefficient $\sqrt{2}$ due to autocorrelation of a Gaussian pulse with itself. Thus the temporal pulse width of the mode locked pulses is 63 ps.

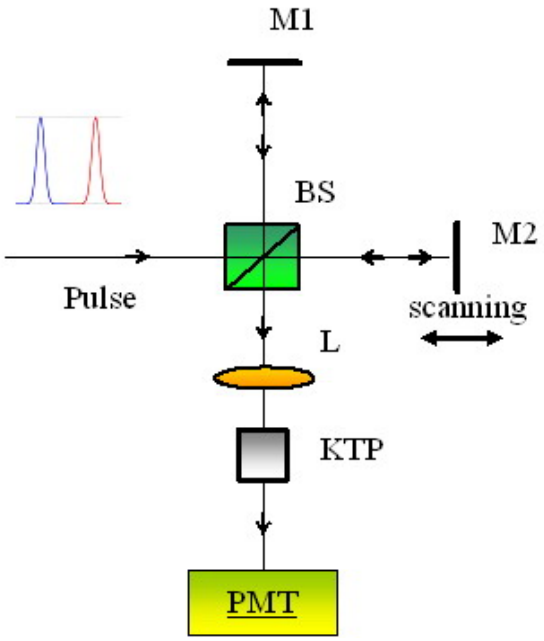

Figure 4-6. Intensity autocorrelator setup (M1---mirror 1, M2---scanning mirror 2, BS---beam splitter, L---lens, KTP---nonlinear optical crystal, PMT—photo multiplier tube). This was used to measure the mode locked pulse width.

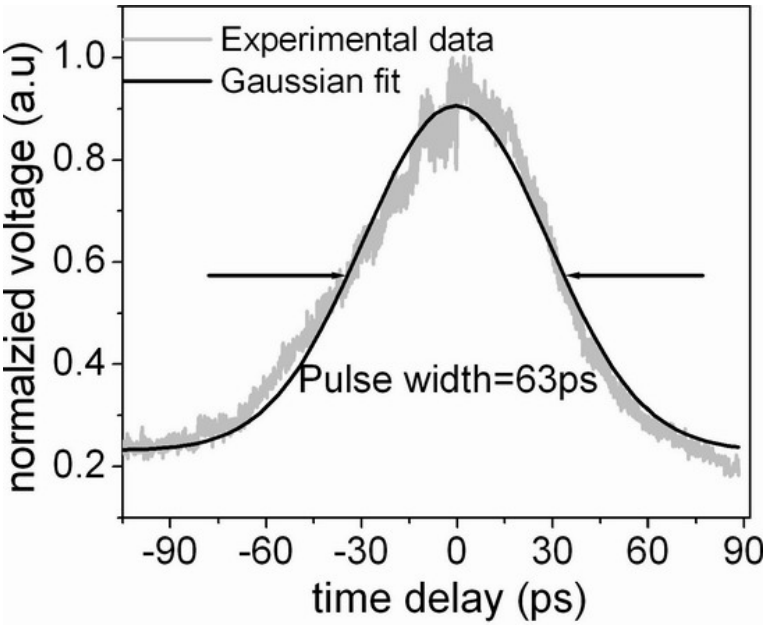

Figure 4-7. Pulse temporal width.

Frequency Locking the Mode-Locked Laser to the High Finesse Cavity

In order to adequately couple all of the laser's longitudinal modes into the HFC, three steps are taken [6]. First the ML-ECDL noise level must be minimized as shown below. Next the RF frequency driving the mode locked laser must be close to the FSR of the HFC. Finally, the laser cavity's length must be finely tuned to match the HFC length to optimize the whole system.

The noise of the ML-ECDL plays a big role in our ability to couple all the longitudinal modes into the HFC. To see this noise, a New Focus 1554 12 GHz photoreceiver is placed after the laser external cavity and a Tektronix 2794 RF spectrum analyzer is used to monitor the noise. First the translation stage under the grating is coarsely tuned to closely match the FSR of external cavity to the RF modulation. It does not have to be a perfect match because, as stated earlier, the laser external cavity has low finesse; i.e. the modulation frequency determines the repetition rate of pulses, not the ECDL length. Then the piezoelectric transducer (PZT) which is placed after the grating is adjusted. It is used to finely tune the grating alignment and also slightly tune the laser center frequency and the length of external cavity. Figure 4-8(a) and 4-8(b) show the noise spectrum of this mode-locked laser at different PZT tuning voltages on the grating. The resolution bandwidth of the spectrum analyzer was set to 3MHz with a full range of about 1.7 GHz for these measurements. Figure 4-8 (a) shows the noise spectrum when the FSR of the ECDL and the repetition rate of the mode-locked laser are mismatched and the grating alignment is non-perfect. Before coupling this mode-locked laser into the

HFC, the noise spectrum needs to be similar to 4-8(b); otherwise, not all the longitudinal modes can be coupled into the HFC simultaneously.

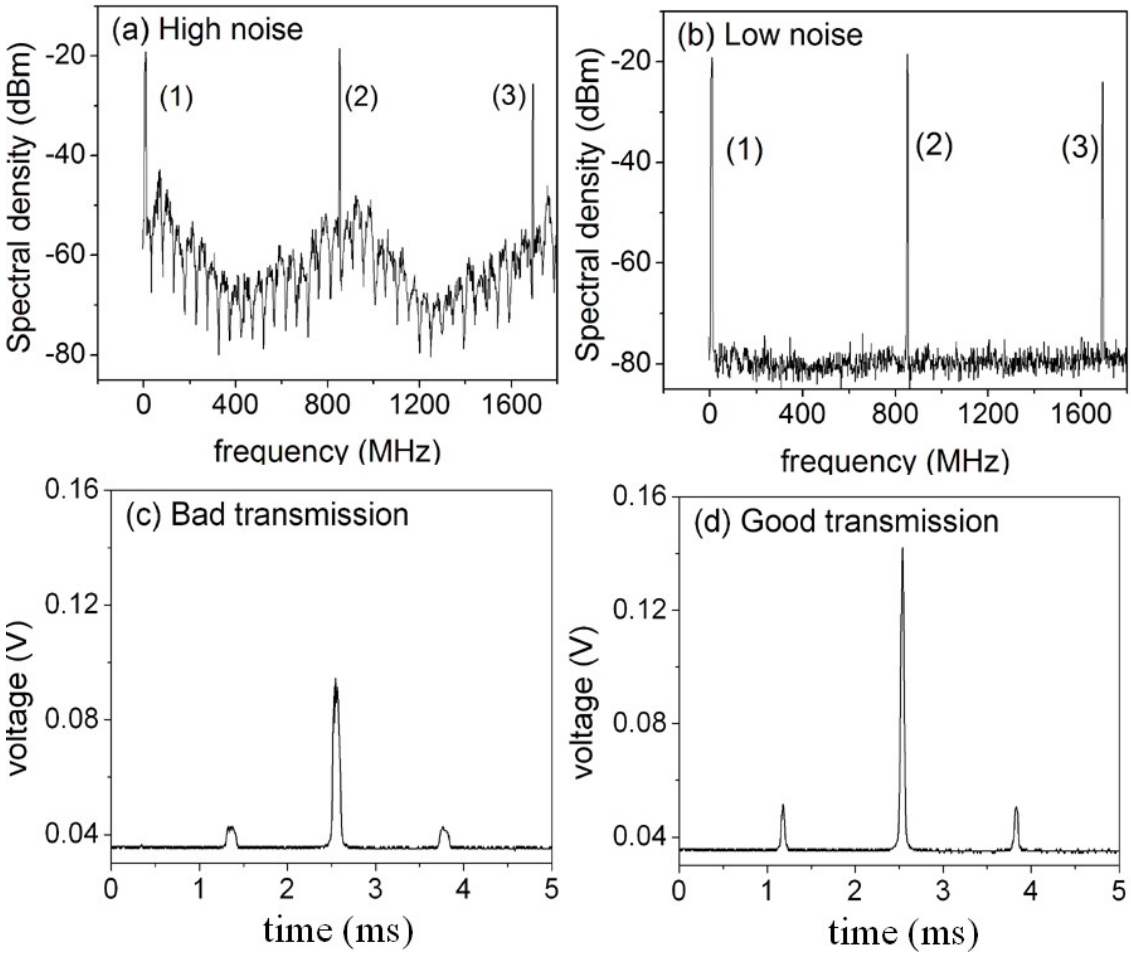

Figure 4-8. It shows the intermediate and final result of frequency locking on noise level and transmission mode when the HFC is being scanned. (a) and (b) show the noise spectrum of ML-ECDL at different PZT voltages. (1) DC. (2) 840.843MHz component. (3) Second harmonic component. The noise level of the laser needs to be as shown in (b) to achieve good coupling to the HFC. Figure 4-8(c) shows the scanning transmission of the HFC when the FSR and RF do not match. Figure 4-8(d) shows the scanning transmission when the FSR and RF match.

Next one needs to match the RF modulation frequency as close as possible to the FSR of the HFC. This process is monitored by maximizing the height of the transmission peak while the cavity is being scanned at 10 Hz. By dividing the HFC FSR (~840 MHz) by its finesse (~10,000), we determined the HFC linewidth to be ~84 KHz. Since the linewidth divided by the number of longitudinal modes is ~ kHz, the RF synthesizer that modulates the laser current needs to have kHz resolution, consistent with our experimental observations.

To further increase the peak height of the cavity transmission, one can finely tune the ECDL length as well. The sidebands in both Figure 4-8(c) and Figure 4-8(d) are due to modulation by an electro-optic modulator (EOM). Figure 4-8(d) shows the transmission when everything is optimized. Figure 4-8(c) shows the transmission at an intermediate step in this process. When the system is optimized, all the laser longitudinal modes are transmitted from the HFC simultaneously, giving one sharp peak. When it is not optimized, the modes transmit at slightly different times, broadening the peaks and dropping the peak power as seen in Figure 4-8(c). During the entire process, the noise influence can guide us in the optimization of the system's alignment.

The HFC is frequency locked to the ML-ECDL by the Pound-Drever-Hall [7, 8] technique for which the electronic locking servo system has a bandwidth of roughly 1MHz. Thus, any laser fluctuation faster than ~MHz will not be able to get corrected. The error signal obtained at the mixer output when the HFC length is scanned with PZT and the servo loop is open looks exactly the same as the error signal due to single mode laser. [9] However, in the ML-ECDL case, the curve represents the summation of all the error

signals from the different longitudinal modes. Since the modes are separated by the FSR of the HFC, this error signal is virtually indistinguishable from the one due to the CW-ECDL. Figure 4-9(a) shows the Pound-Drever-Hall error signal obtained at the mixer output when the HFC length is scanned and the servo loop is open. The original voltage versus time trace obtained from the oscilloscope was converted to arbitrary voltage versus frequency offset. The curve represents the summation of all the error signals from the different longitudinal modes. Figure 4-9(b) shows the broadening of the transmission peak of the HFC when feedback is being applied by the fast servo to the laser current while the HFC is still being scanned. Comparison with figure 4-8(d) shows that the center transmission is not a sharp peak anymore because the fast servo causes the peak to broaden as it tries to keep all the laser longitudinal modes on resonance with the HFC.

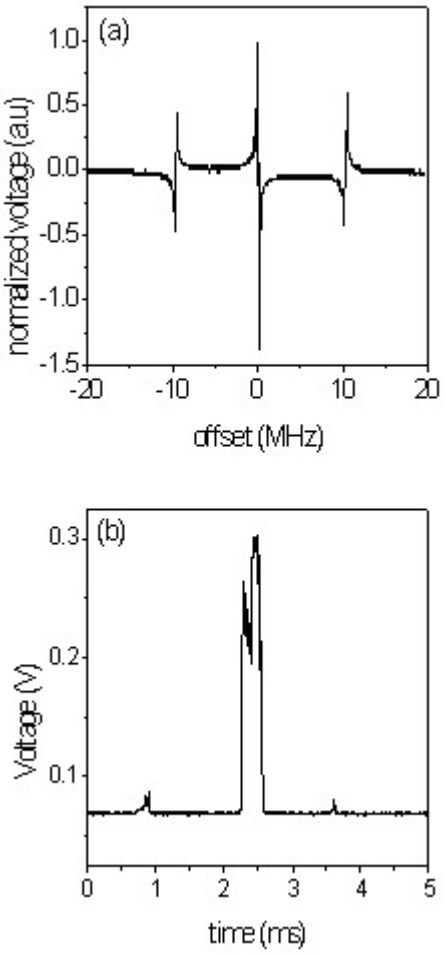

Figure 4-9. (a) Error signal obtained at the mixer output when the HFC was scanning. (b) transmission mode broadening with error signal feeding back to fast servo. The trace in (b) indicates that the fast servo is trying to lock the laser to the HFC as the cavity is scanned.

Figure 4-10 shows the transmitted power when the system is locked and not locked. Since this is a HFC, the linewidth is ~84 kHz, while the lindwidth of the ML-ECDL is ~56 GHz. When the system is not locked, almost no light can get through the high finesse cavity. When the system is locked, with 400 μW average input power before the HFC, or roughly 260 μW coupled power by considering the window loss and non-

perfect mode matching in the HFC, about 22 μW is transmitted and the whole system can stay frequency locked for hours. No temperature control servo is used for the HFC and the system can remain locked in the lab environment with room temperature fluctuations of ±2°C. The vibration isolation was considered in the design of the HFC. The HFC is composed of two nested cylinders. The outer cylinder is sealed from the lab environment. The inner cylinder contains the high-finesse mirrors and is vibrationally and thermally isolated from the outer cylinder by means of some rubber padding. The system can maintain lock when the optical table is lightly tapped.

Figure 4-11 shows the optical spectrum of the ML-ECDL before and after the HFC. The spectra are similar, showing that, after optimization of the laser to the HFC, most of the laser's longitudinal modes are simultaneously transmitted by the HFC when the system is locked.

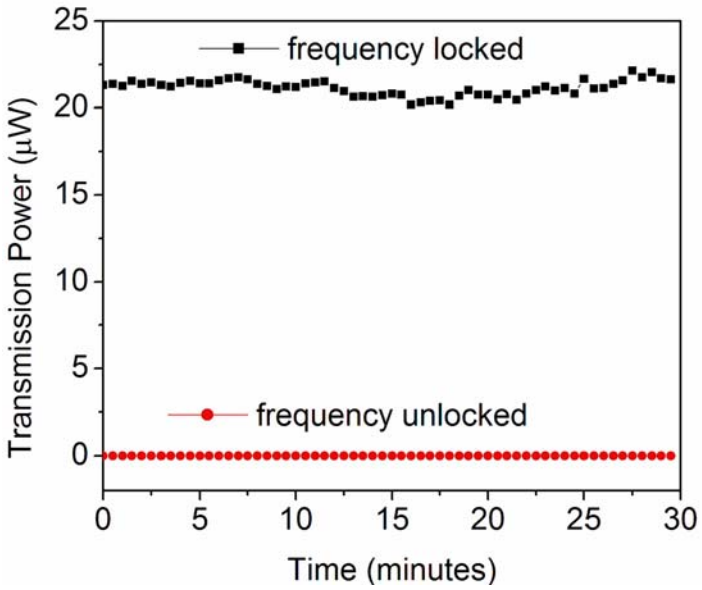

Figure 4-10. Transmission power of the mode locked diode laser when it is locked to the HFC.

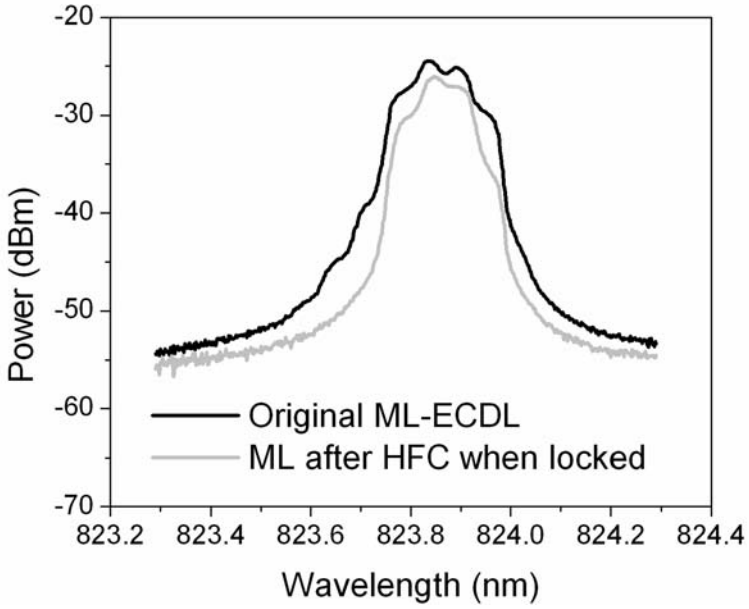

Figure 4-11. Optical spectrum of original ML-ECDL and frequency locked ML taken using the optical spectrum analyzer. The similarity of the spectra indicates that many longitudinal modes are being transmitted by the HFC as would be expected with good stabilization to the cavity.

Tapered Amplifier Diode Laser

The typical CW-ECDL output power is 5-20 mW. After beam-shaping, Faraday isolation and fiber coupling, only 3-10 mW remain. Similarly, the typical average output power of a ML-ECDL is only 1-2 mW [10]. However for the ML Raman experiments, we would like to have pump power on the order of tens of mW. A tapered amplifier (TA) diode can make the optical power much higher while maintaining all the optical properties of the seeding ECDL.

In the past, most optical amplifiers were either extremely expensive or difficult to make reliable. Recently lower cost tapered amplifier diodes have become commercially available, making diode optical amplifiers more practical. With improvements in anti-

reflection (AR) coating technology, laser action of the tapered amplifier itself can be avoided by coating both the front and back facets, giving the laser system the best possible performance. Here we investigate a TA diode system that can amplify either a CW-ECDL or a ML-ECDL. The TA diode is manufactured by a German company called Eagleyard Photonics. The gain region of the TA diode as shown in Figure 4-12 is 2.75 mm long with 3 μm and 190 μm input and output 1D apertures respectively. As for the height of the gain region, the manufacture does not provide any number, but we think it is about 2.4 μm using single slit diffraction limit. According to the manufacturer's datasheet, the maximum output power is about 500 mW within a wavelength range from 790 to 810 nm. Figure 4-13 shows the amplified spontaneous emission (ASE) spectrum of the TA diode without any seeding light. Due to the nice AR coating on both facets, the spectrum can cover more than 20 nm.

This section is organized as follows: we first give detail on the TA diode system design and alignment; next we discuss the experimental setup and then describe the measured performance of this TA diode system. We finish with some conclusions about such systems.

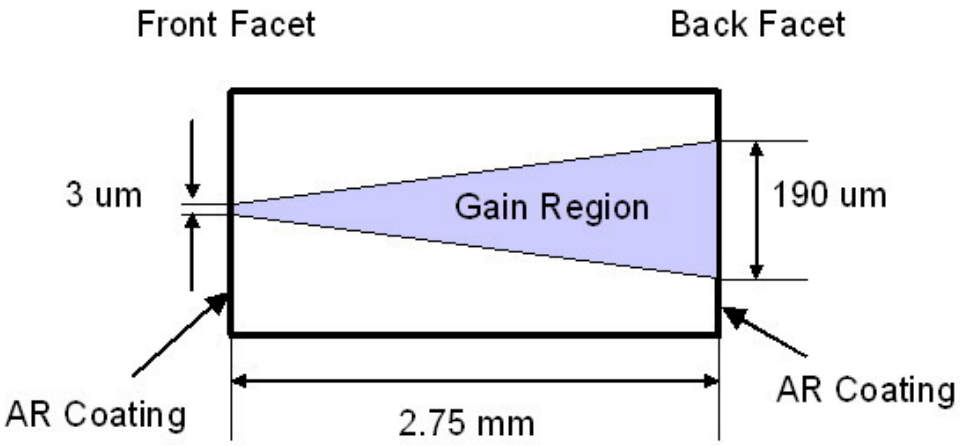

Figure 4-12. Tapered amplifier's gain region structure.

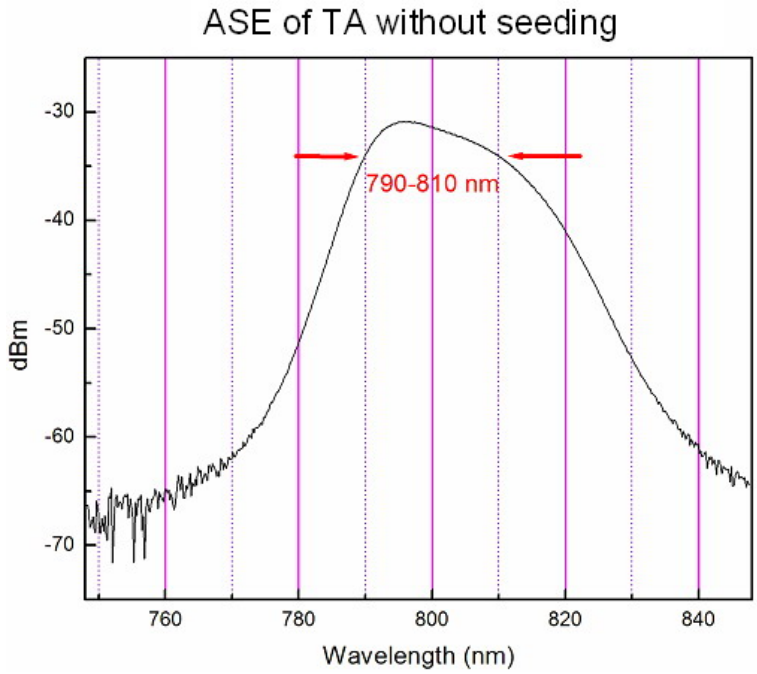

Figure 4-13. Amplified spontaneous emission spectrum of the TA diode without seeding. Due to the nice AR coating, the TA diode can operate from 790-810 nm.]

Tapered Amplifier Diode System Design and Alignment

We designed a simple, stable and compact TA diode system (Figure 4-14 and 4-15) which consists of a TA diode, two aspheric collimation lenses (f = 4.5 mm, 0.55 NA, Thorlabs C230TM-B) threaded into home-made tubes inserted into a modified fiber holder (Newport F-91-C1-T), a plano-convex cylindrical lens (f = 50 mm) and a 4×3×2.2 inch aluminum heat sink. The details about the mechanical design are in Appendix F. The C-Mount TA diode has an anti-reflection coating on both ends and a 2.75 mm long tapered gain region, which allows for a weak signal to be injected into the narrow end and the amplified light to come out from the broad end after traveling through the gain region. It is necessary to have a compact and stable mount for the TA diode and the collimators because the input aperture of the TA diode is only 3μm. The C-Mount TA diode is screwed onto a home-made brass diode holder. The modified commercially available fiber holders with collimation lenses in them are attached on both sides of the diode holder. These fiber holders allow adjustments in three dimensions, ensuring good coupling of the input light and collimation of the output light. In earlier work [11], the z direction of the output collimator was not accessible from the outside. However in our design, all these adjustments are accessible from the outside of the housing surrounding the TA diode mount.

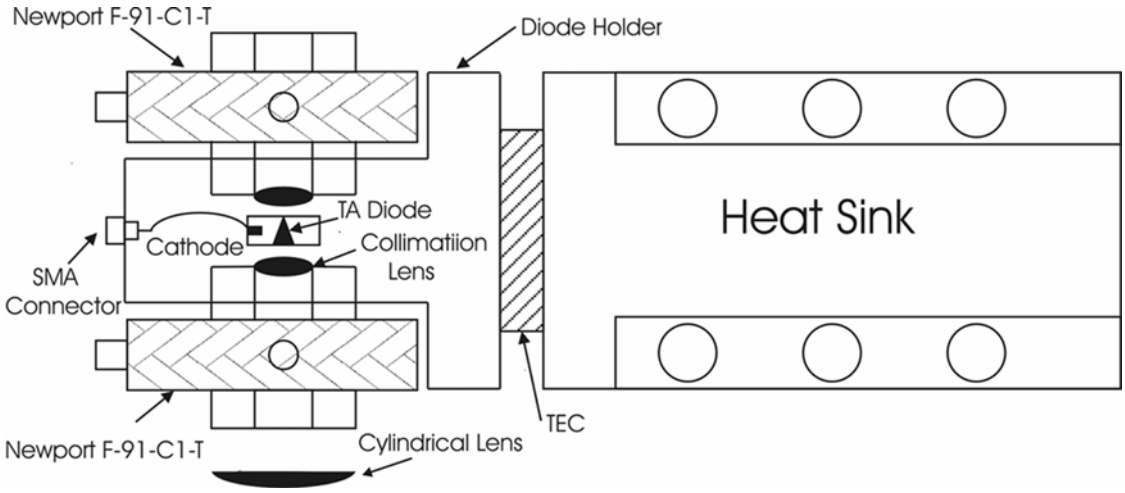

Figure 4-14. Top view of the TA diode system. The heat sink and TEC are for cooling the TA diode; Newport F-91-C1-T and Cylindrical lens are for collimation adjustment; the SMA connector is for strain release.

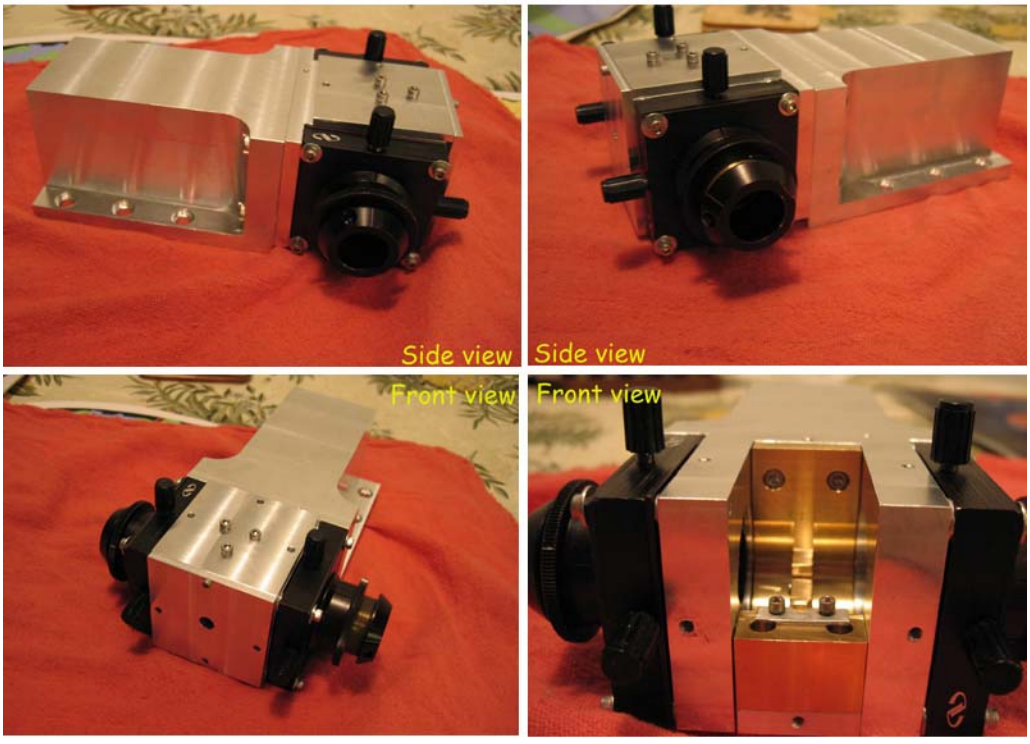

Figure 4-15. Side and front view of the TA diode system. In the lower right photo, the cases are removed to show the inside diode mounting region.

Temperature variations can cause the output power of the TA to fluctuate. To thermally control this system, we attached the brass diode holder mount to an aluminum heat sink with a 2×2 inch thermoelectric cooler in between. In addition, the aluminum housing that surrounds the TA is designed to minimize the amount of air around the TA to help reduce any thermal variations that air movement could cause. Water cooling was not needed or used in our design.

The soldered connection of the diode cathode tab on the C-Mount is very fragile and needs to be attached quickly in order to prevent damage to the TA diode by overheating. Therefore, in addition to screwing the TA diode onto the home-made brass diode holder, we also soldered the cathode tab to a wire from a SMA connector attached to the front case of TA diode system in order to serve as a strain release. This helps to prevent accidental damage to this fragile connection.

Good alignment plays a big role on the amplification performance. In this system, we first turn on the TA without injecting any seeding light; because of the AR coatings, the ASE power is only from 0.8 to 3 mW depending on the TA drive current. On the input side, the three dimensional adjustments of the input lens allow the emitted ASE to be collimated. The ASE beam profile on the input side is roughly circular and can therefore be fiber coupled with about 45-55% efficiency into a single mode fiber, where the seeding light comes through. This high efficiency ensures good portion of the seeding light coupling into TA diode.

In the output side, the manufacture datasheet lists the perpendicular divergent external half angle as 14^{o} and the parallel divergent external half angle as 5^{o}. In order to

collimate such a beam, a spherical and a cylindrical lens are needed. Figure 4-16 shows the side and top view of the geometrical trace of collimating the TA output beam with these two lenses. A 4.5 mm spherical lens was used to collimate the perpendicular divergent beam. Using geometric optics, we calculated a perpendicular collimated beam size of 2.242 mm and the location where the parallel beam focuses. Knowing these two numbers, we determined that a 54 mm focal length cylindrical lens would be needed to collimate the parallel divergent beam to the same size as the collimated perpendicular beam [Appendix G].

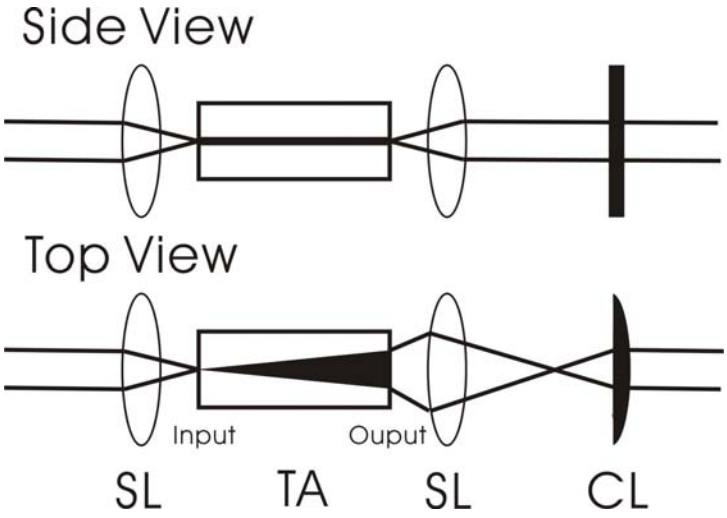

Figure 4-16. Side and top view of the geometrical trace of collimating the TA output beam with a spherical and a cylindrical lens. (SL---spherical lens, TA—tapered amplifier, CL---cylindrical lens)

We used the closest commercially available cylindrical lens which has a 50 mm focal length. In this way, the beam shape will be close to circular before going through the Faraday isolator and being fiber coupled. Figure 4-17 gives details about the beam shape after the TA diode and both lenses. The parallel and perpendicular beam widths

were measured with BeamView software to be 2.51 mm and 2.153 mm respectively, very close to the 2.242 mm calculated earlier. The ratio of parallel to perpendicular is about 5:4.3; not a perfectly circular beam, but close enough to give 45-55% fiber coupling efficiency into a single mode fiber. Improvements to the circularity of the beam may be possible by changing the focal length of the cylindrical lens. The whole alignment process is quite simple because of the easy access to the three-dimensional adjustments on both collimation lenses.

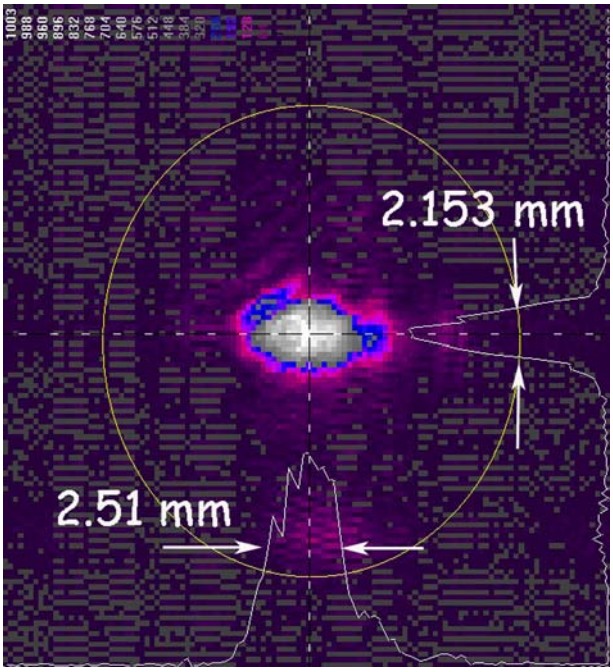

Figure 4-17. Beam shape after the TA. The beam viewer software shows the parallel and perpendicular widths are 2.51 mm and 2.153 mm. The beam shape is not perfectly circular, but good enough to give 45-55% coupling efficiency to a single mode fiber.

Experimental Setup

The experimental setup is shown in figure 4-18. Both DC and AC current supplies are connected to the ECDL via a bias tee. A 5 dBm AC Sine wave modulation at 840

MHz is produced by a signal generator (HP 8648A) and is amplified to 23 dBm (Mini-Circuits ZQL-900LNW) before being combined with the DC current and applied to the ECDL. With only the DC current on, it behaves as a CW-ECDL; while with the sinusoidal AC current at 840 MHz in addition to the DC current, it acts as a ML-ECDL. Output light from the CW-ECDL (or ML-ECDL) goes through a Faraday isolator, half wave plate, polarizing beam splitter and then is coupled into a single mode fiber with a collimation lens, the output of which is the seeding power for the TA diode system. An ILX Lightwave LDC-3744B diode current controller is used as the current source for the TA diode. This instrument provides a maximum DC current of 4 A. The amplified light after another Faraday isolator is considered as the output power from TA diode system.

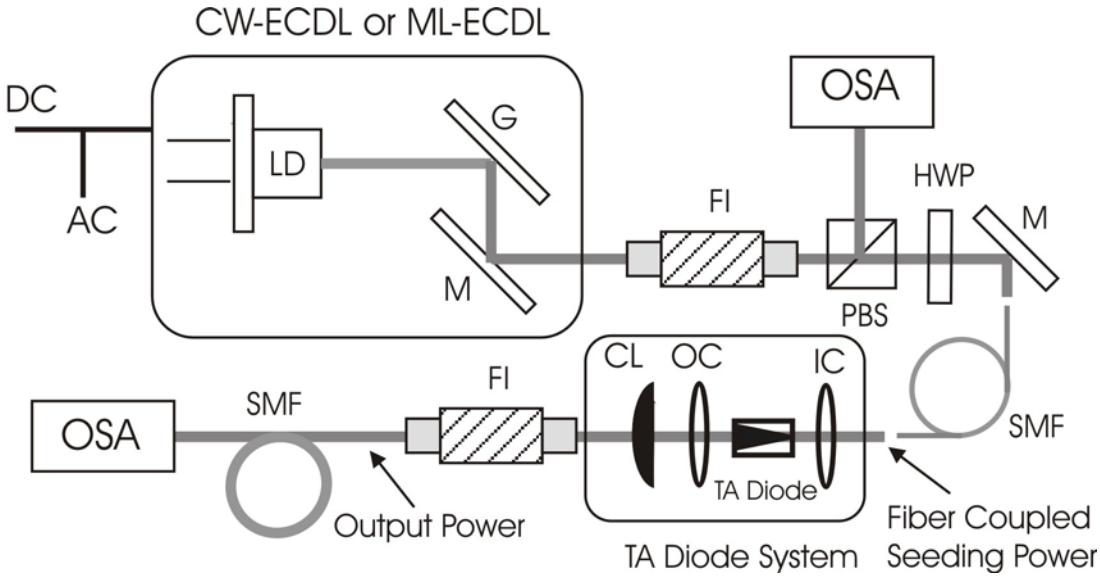

Figure 4-18. Experimental setup. G: Grating; LD: Laser Diode; M: Mirror; FI: Faraday Isolator; HWP: Half Wave Plate; PBS: Polaring Beam Splitter, SMF: Single Mode Fiber; IC: Input Collimator; OC: Output Collimator; CL: Cylindrical Lens; OSA: Optical Spectrum Analyzer.

Characteristics of the Tapered Amplifier Diode System

With CW-ECDL seeding, figure 4-19 shows plots of the TA output power as a function of drive current for two different temperatures, 18^{o}C and 22^{o}C. Since both the TA diode and the collimation lens are mounted to the same piece, they will tend to have the same thermal expansion rate. Thus we expect that even with a 4^{o}C change in temperature, only a small misalignment will occur. However we did readjust the fiber coupler for the seeding power after every temperature adjustment to maximize the coupling efficiency of the seeding power into the TA diode and found very little correction was needed. Both plots show that for a higher TA drive current, higher amplification is achieved. By comparing the amplification for the same TA drive current at different temperatures, it can be seen that by lowering the temperature from 22^{o}C to 18^{o}C, the amplification increases by roughly 10-20%. With 5 mW seeding power at 18^{o}C, 240 mW is achieved after TA and 115 mW (48%) can be coupled into a single mode fiber.

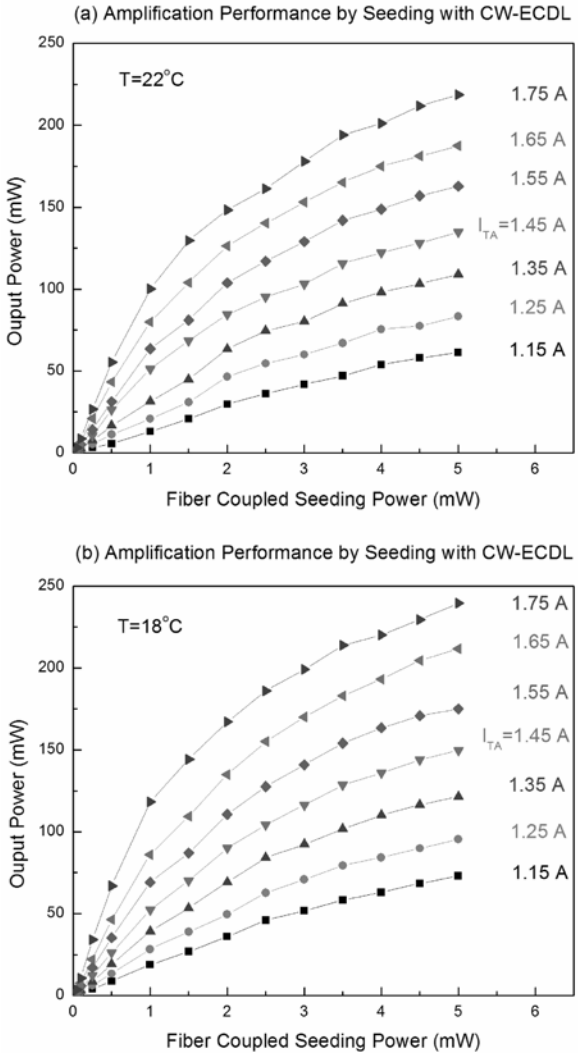

Figure 4-19. Temperature and current dependence of TA amplification by seeding with the CW-ECDL. Both plots show the amplification when the TA is operated at seven different currents. (a) T=22°C, (b) T=18°C. Lower temperature and higher drive current give higher amplification.

Figure 4-20 shows the TA output power versus drive current at 18°C after seeding with the ML-ECDL. With 0.75 mW average seeding power, 80 mW average power can be achieved by driving the TA at 1.75 Amps and 18°C, 39 mW (49%) of which can be coupled into a single mode fiber [10, 12]. A typical interferometric autocorrelation

trace[13] is shown in figure 4-21, which displays a pulse with a full width at half maximum (FWHM) measurement of 12 ps in duration. Deconvolving this measurement with a Gaussian pulse shape yields a temporal pulse width of 9 ps. With a repetition rate of 840 MHz (or 1.19 ns), the 80 mW average mode-locked power corresponds to a peak power of about 11 W. The 15μm actuator step size of our autocorrelator is not fine enough to resolve the details of the electric field modulation under the fitting curve, but still shows the field modulation properties. This autocorrelation trace looks different than the figure 4-7 due to different optical alignment. In order to get interferometric trace, a collinear alignment is required, which means that two different paths of the beam have to totally overlap. According to my personal experience, this is not easy to achieve and most case, an intensity autocorrelation trace like figure 4-7 is achieved.

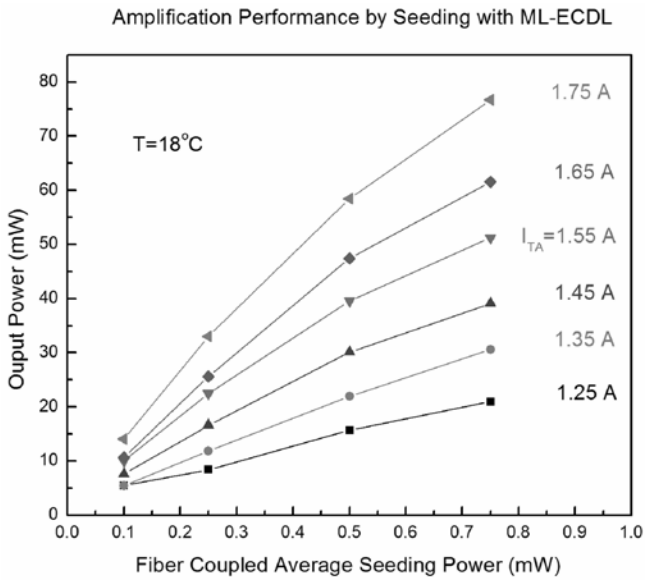

Figure 4-20. Amplification performance by seeding with ML-ECDL at different TA currents.

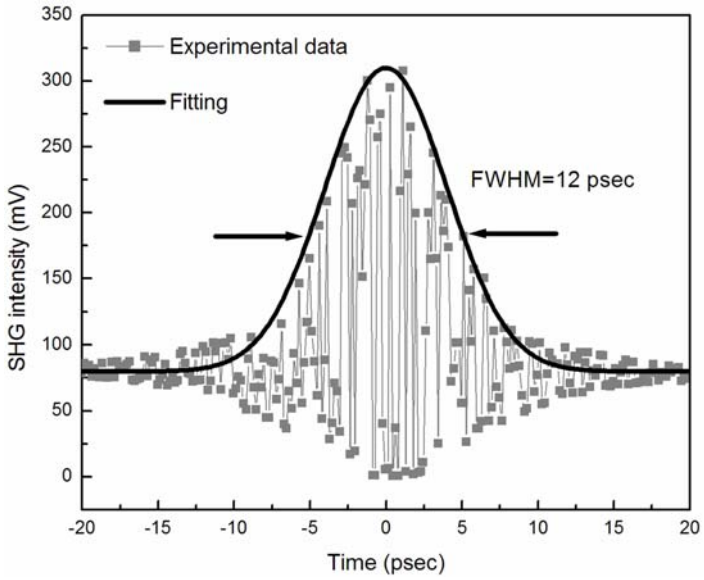

Figure 4-21. Interferometric autocorrelation trace of the amplified pulses. Autocorrelation of the ML laser pulse shows a FWHM of 12 ps. This corresponds to pulse duration of approximately 9 ps by taking the deconvolution between pulse shapes. Since the stepping of the autocorreltor is not fine enough, the structure underneath the fitting curve does not represent the details of the electric field modulation, but still shows the field modulation property.

Figure 4-22 shows the optical spectrum of the seeding light and the light after amplification. In both the CW and ML cases, the amplified light keeps the same optical spectrum as the seeding light. Since the TA diode is AR coated at both ends, with a drive current from 1.15 A to 1.75 A, the ASE varies from 0.8 mW to 3mW and the optical spectrum is flat over about 20 nm. By comparing the ASE with the output power in figure 4-18, we can tell that except when the seeding power is small, the ASE is negligible compared to the amplified light. After being amplified by the TA, the mode suppression is roughly 38 dB for CW seeding and 32 dB for ML seeding, which equal the mode suppression of the seeding CW-ECDL and the ML-ECDL. The spectral width of

amplified ML-ECDL is 0.16nm, roughly corresponding to 72 longitudinal modes, which also maintains the spectral width of the seeding ML-ECDL. The fraction of ASE background in the TA output is obtained by integrating the power spectral density on a linear scale in figure 4-22, yielding 1.65% for CW seeding and 2.92% for ML seeding at 22^{o}C. We can see obvious improvement of our system when compared to the results of previous experiments [11], which achieved, with CW seeding, 5.6% at 16^{o}C and 1.4% at 5^{o}C. The improvement in our case is probably due to a better AR coating on our TA diode. In general, thermal instabilities make the output power fluctuate; however with the considerations mentioned earlier, the output power after this TA diode system is very stable once the system reaches thermal equilibrium. As shown in figure 4-23, with 2 mW CW seeding power at 22^{o}C, during the first couple of minutes after turning on the TA, the power reaches 160 mW and then drops immediately due to sudden temperature changes associated with turning on the TA diode. After about 15 minutes, when the system reaches the thermal equilibrium, the output power remains at 140 mW for more than the 50 minutes measured.

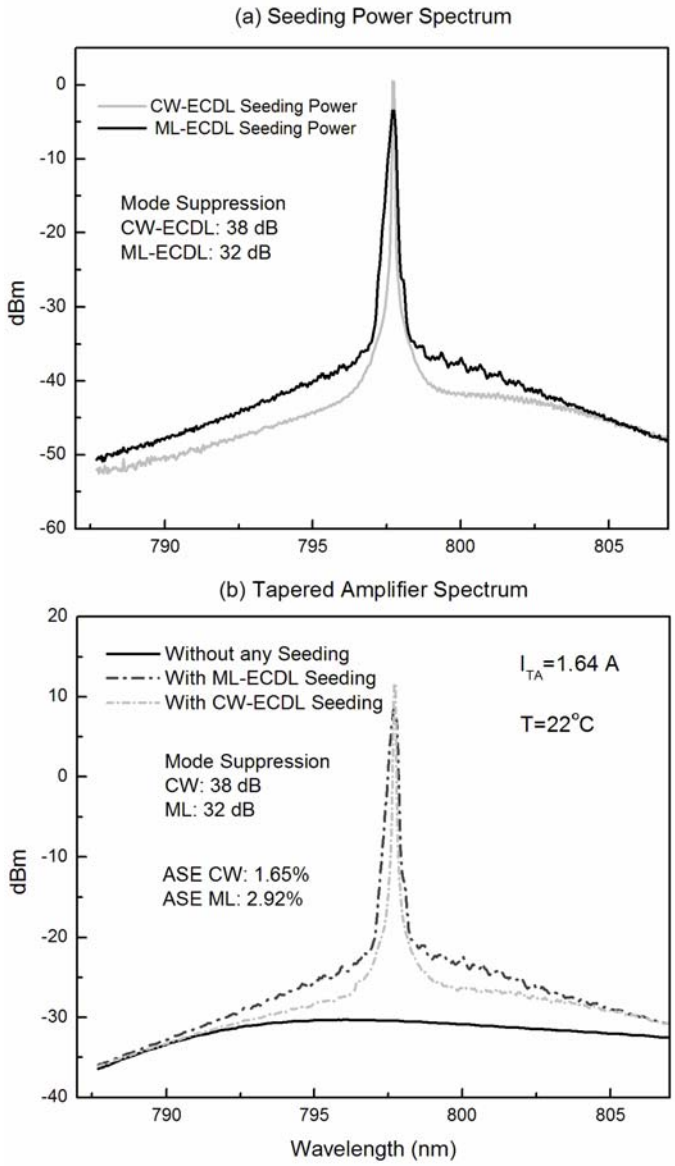

Figure 4-22. TA optical spectrum with ML and CW seeding. Mode suppression is about 32 dB and 38 dB respectively.

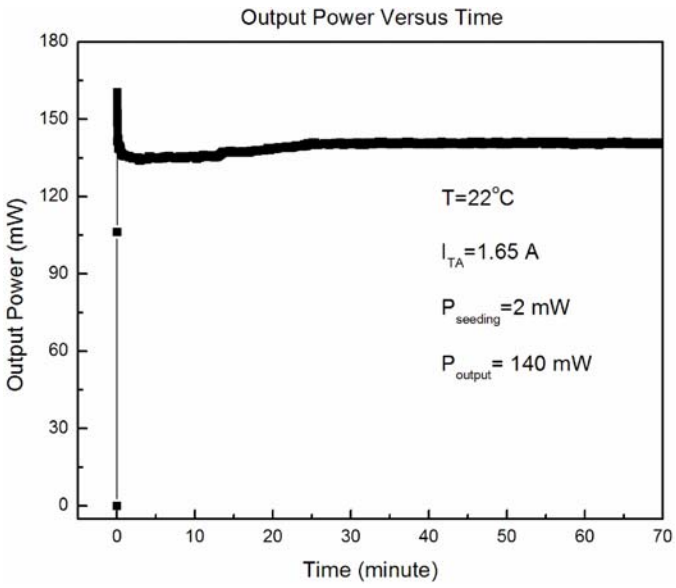

Figure 4-23. TA output power versus time. TA diode system reaches thermal equilibrium 20 minutes after turning on the TA diode, and the output power remains 140 mW for more than 50 minutes.

Summary of the Tapered Amplifier Diode System

We have shown a simple and stable design for a tapered amplifier diode system, taking into consideration the thermal management of the heat dissipation, three-dimensional collimation adjustments and strain release. The easily accessible three-dimensional collimation adjustments allow us to precisely align the input and output with the TA diode, giving better output amplification performance. Both CW-ECDL and ML-ECDL were constructed and used to inject optical power into the TA diode system. CW power after amplification reached 240 mW with 5 mW seeding power. This can be used as a tunable laser source for a Lidar project, like water vapor profiles in atmosphere [14] or any other system that requires high power while maintaining the narrow linewidth and frequency tunability. With 0.75 mW average seeding power, ML average powers after

amplification exceeded 80 mW with 9 ps pulse duration, translating to a peak power of around 11 W. These power levels should be sufficient to investigate nonlinear optical phenomena, such as self phase modulation in a fiber or the Raman effect in high finesse cavity with hydrogen. We also showed the optical spectrum after the TA maintains the same characteristics as the seeding light, and that the output spatial mode quality allowed 45-55% coupling efficiency into a single mode fiber.

CW and Mode-Locked Raman Laser Experiments

Experimental setup

The pump source in this setup is an ECDL with Littrow configuration, and by turning on or off the RF synthesizer signal, we can switch the pump source between the ML-ECDL and the CW-ECDL. The estimated optical spectra of both the ECDLs are shown in figure 4-24. For the Littrow cavity, the optical spectrum of the CW-ECDL is made of a single longitudinal mode with the linewidth of 1~ 2 MHz [3]. For the ML-ECDL, the optical spectrum is made of several longitudinal modes, each of which has the same linewidth as the mode of the CW-ECDL and are roughly separated by a GHz. The details of the ML spectra will be discussed later in the paper in connection with the beating measurements.

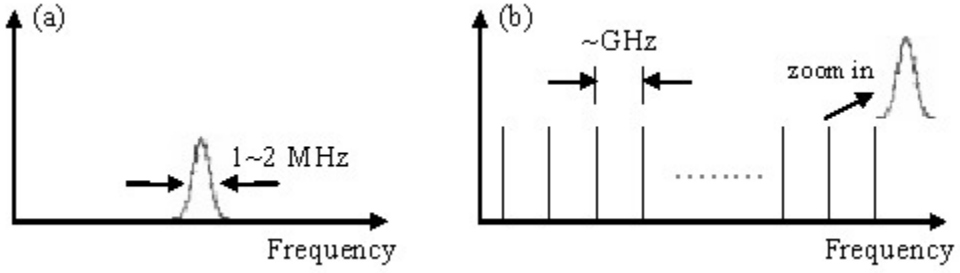

Figure 4-24. Estimated optical spectrums of CW-ECDL and ML-ECDL. (a) For the Littrow configuration, the CW-ECDL has a linewidth of 1~2 MHz. (b) For the ML-ECDL, the optical spectrum is made of several longitudinal modes, each of which has the same linewidth as the mode of the CW-ECDL and are roughly separated by a GHz.

Of the three pressure regions, only the medium pressure region (~10 atm) is easily accessible to us experimentally because the high pressure region would require a complete redesign of the Raman cavity and in the low pressure region, the Raman gain profile narrows, making it difficult to find a cavity mode at the Stokes wavelength that will be above threshold. Thus, we were only able to compare our experimental results for the medium pressure region.

Figure 4-25 illustrates the experimental setup. Two Faraday isolators are used to minimize the optical feedback to the ECDL. An optical spectrum analyzer (OSA) is used to monitor the pump laser optical spectrum. Then the beam travels through a tapered amplifier (TA) diode system to increase the power [15]. Another isolator is used to prevent feedback to the TA diode. The output coupler and the cylindrical lens in the TA diode system mode match the beam to the HFC. The combination of a polarizing beam splitter (PBS) and a quarter-wave plate (QWP) before the HFC allows a photodetector D1 to receive the reflected light from the front mirror of the HFC, which is used to generate the Pound-Drever-Hall error signal. A half wave plate (HWP) is placed before the PBS to

vary the incident pump power on the HFC. An electro-optic modulator (EOM) is driven by a 12 MHz sine-wave generator and is used to add RF sidebands on the optical frequency as required for Pound-Drever-Hall locking [6,7,9]. The mixer multiplies the 12 MHz sine-wave signal with the reflected signal from D1 to produce the error signal. The error signal is then input to two servos. The fast servo feeds the error signal back to the ECDL's DC current controller for fast corrections to the laser's frequency. At the same time, the slow servo sends feedback to the HFC's piezoelectric transducer for slow corrections to the HFC's length. For good frequency locking, the RF modulation to the ECDL has to match the free spectral range (FSR) of the HFC very well, the details of which are in Ref 15 and earlier in this chapter. The HFC in this setup is made of two mirrors with high reflectivity ($R \approx 0.9999$ at both pump and Stokes wavelengths) on both ends and is filled with 10 atm of H_2 gas.

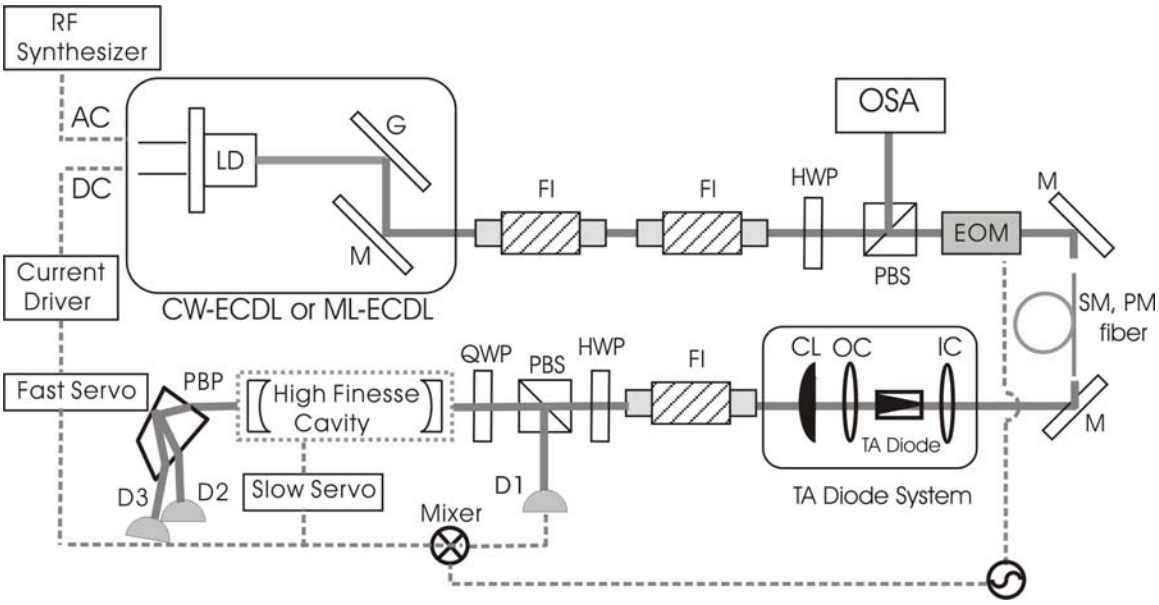

Figure 4-25. Schematic of experimental setup. (G---grating, M---mirror, FI---Faraday isolator, HWP---half wave plate, PBS---polarizing beam splitter, SM---single mode, PM---polarization maintaining, OSA---optical spectrum analyzer, QWP---quarter wave plate, EOM---electro-optic modulator, TA---tapered amplifier, IC---input coupler, OC---output coupler, CL---cylindrical lens, PBP---pellin broca prism, D1---detector for error signal, D2 and D3---detectors for the pump and Stokes transmission). Dotted lines represent electronic wires.

Results and Analysis

We showed the intra-cavity field Equations 3.28-3.29 in chapter 3. To find the fields outside the Raman cavity we multiply by $(1/2)\sqrt{T}$, since light can escape from either of two mirrors. Therefore the fields exiting the HFC become:

$$E_{pn(f)} = -\sqrt{R_{p(f)}}E_{p_{in(n)}} + 1/2\sqrt{T_{p(f)}}E_{pn} \tag{4.1}$$

$$E_{pn(b)} = 1/2\sqrt{T_{p(b)}}E_{pn} \tag{4.2}$$

$$E_{sn(f)} = 1/2\sqrt{T_{s(f)}}E_{sn} \tag{4.3}$$

$$E_{sn(b)} = 1/2\sqrt{T_{s(b)}}E_{sn} \tag{4.4}$$

where the first term on the right-hand side of Eq. (4.1) accounts for the reflected incident pump field and f and b indicate the front and back of the Raman cavity.

Now it is necessary to convert the fields into powers so that we can compare the experimental data with the theory. We define the power by the following equation:

$$\mathrm{P} = \frac{1}{2}\left(\frac{\varepsilon_0}{\mu_0}\right)^{1/2} |E|^2 A \tag{4.5}$$

with the scaled area A for both the pump and Stokes fields given by [16-18]

$$A = \frac{l\lambda_p}{4\tan^{-1}(l/b)} \tag{4.6}$$

where l is the length of the cavity, $b = \sqrt{l(2R_0 - l)}$ is the confocal parameter [19] of the beam and R_0 is the radius of the cavity mirrors.

First we study the growth of the Raman laser in the CW regime by turning off the RF synthesizer. The pump laser is at 799 nm and the output Stokes is at 1196 nm. Through cavity ringdown measurements, the HFC's mirror reflectivity at the pump wavelength is measured to be $R_p = 0.99983$ [Appendix H]. The HFC's length is $l = 17.84$ cm, the radius of the mirror $R_0 = 50$ cm and the Raman plane-wave gain coefficient [20, 21] is α=1.53×10^{-9} cm/W at 10 atm. Figure 4-26 shows the transmitted pump and Stokes power as a function of input pump power. As the input pump power increases, the transmitted pump increases until the system reaches the threshold, then the transmitted Stokes starts to grow while the transmitted pump power clamps. To fit the

theory to experimental data, we used the following parameters: $R_p = 0.99983$, $R_s = 0.99980$, $T_p \approx 43$ ppm and $T_s \approx 25$ ppm, which are very close to the manufacturer's data [22]. The apparent (top scale of the figure 4-26) threshold, which does not account for mode-matching losses into the HFC, is measured to be 4.79 mW. From the behavior of the system below threshold, the coupling efficiency into HFC is about 81.3% [23, 24]. So the real threshold is about 3.89 mW.

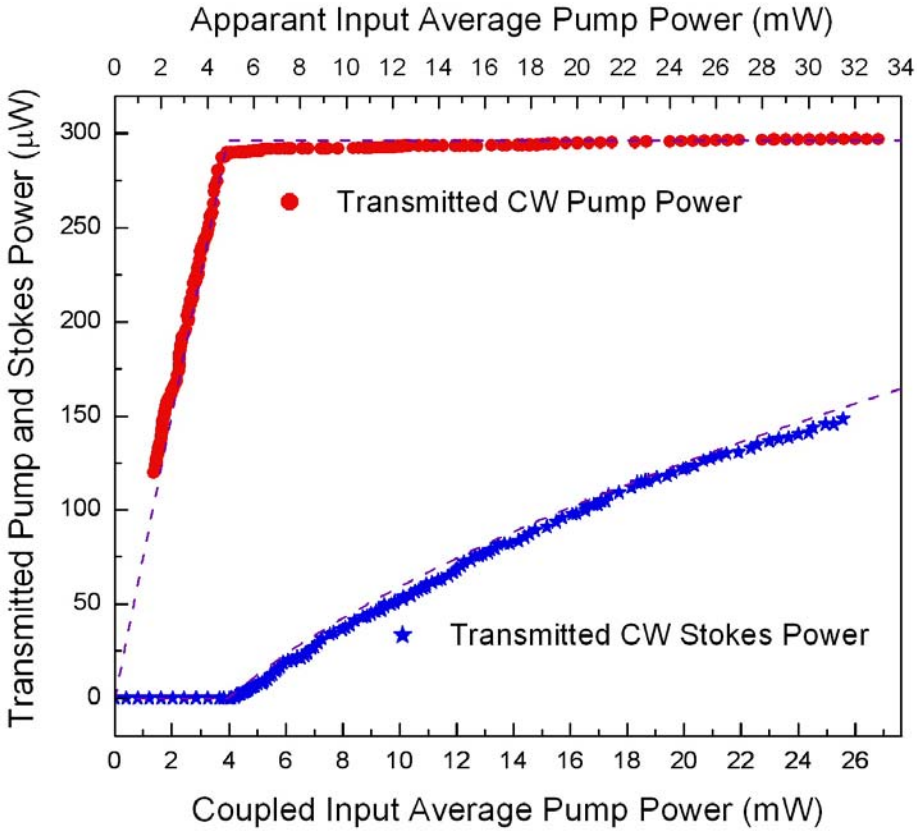

Figure 4-26. Experimental data and theoretical fits of the CW-ECDL pumped Raman laser. Solid circles and stars represent the cavity transmitted CW pump (799 nm) and Stokes (1196 nm) power. The dashed lines are the theoretical fitting. The measured threshold is 4.79 mW; the actual threshold is 3.89 mW because of the 81.3% coupling efficiency.

Next we study the growth of the Raman laser in the ML regime. To do this, we turn on the RF synthesizer, instead of pumping with a CW-ECDL, now the pump source is a ML-ECDL. The estimated input pump spectrum is shown in figure 4-24(b). Back in the TA diode system test, higher RF power (23 dBm) was used. For the amplification test, we wanted to see if the TA diode system works for the short pulse and the noise of the system was not the main concern. Here we decrease the RF modulation power to 18 dBm because less RF power produces less noise in the ML laser which gives relatively easy time to do frequency locking. For this experiment, there were roughly 9 longitudinal modes due to the 18 dBm RF modulation [25, 26].

The transmitted ML Stokes and pump average power is shown in figure 4-27. The threshold is around 5.4 mW. We noticed the transmitted pump after threshold is not clamping as in the CW case. We feel that this is because of the thermal lens effect in the Raman gas seen previously [27]. In other words, when the Stokes lasing starts to build up, the vibrational energy deposited in the gas causes hydrogen to expand in the region of laser beam, forming a negative lens effect. Due to this effect, the beam size becomes bigger and the Stokes power decreases, equivalent to a decrease in the Raman gain.

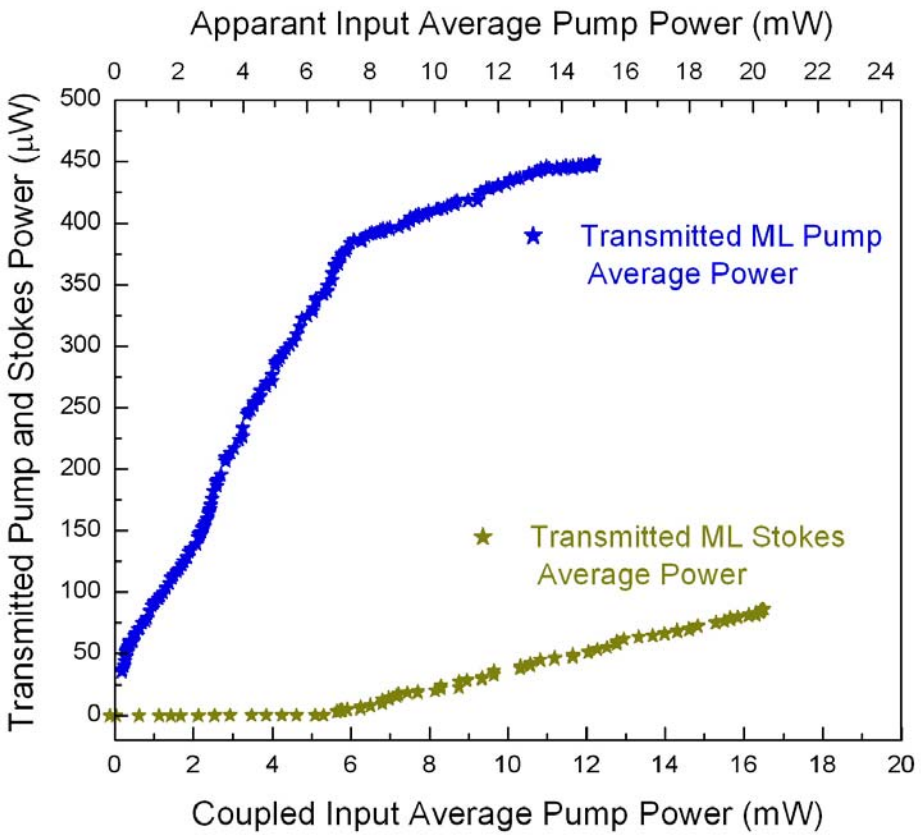

Figure 4-27. Experimental data of transmitted ML pump and ML Stokes.The measured threshold is 6.75 mW; the actual threshold is 5.4 mW because of the 81.3% coupling efficiency.

The experimental and theoretical Stokes output is plotted in figure 4-28. From the theoretical prediction as shown in figure 4-28, if all the longitudinal modes are on the Raman gain line center (α=1.51×10^{-9} cm/W), the threshold for this case should be 2.48 mW, 36% less then the CW pumping threshold. However the experimental data showed the threshold is at 5.4 mW. To account for this discrepancy, we considered many possibilities. We began by looking at the dispersion of the hydrogen, which could lead to a mismatch between some of the pump laser frequencies and the cavity resonance

frequencies. However, the calculation of the index of refraction variation across these 9 longitudinal modes showed the dispersion effect is negligible. Then we calculated the coupling efficiency into HFC for the CW and ML case when operating below the system threshold, which we determined to be the same. After eliminating the above possibilities, we think the discrepancy is probably because the combination of the Raman thermal lens effect and the fact that the Stokes longitudinal modes are not on the center of Raman gain distribution, as explained below.

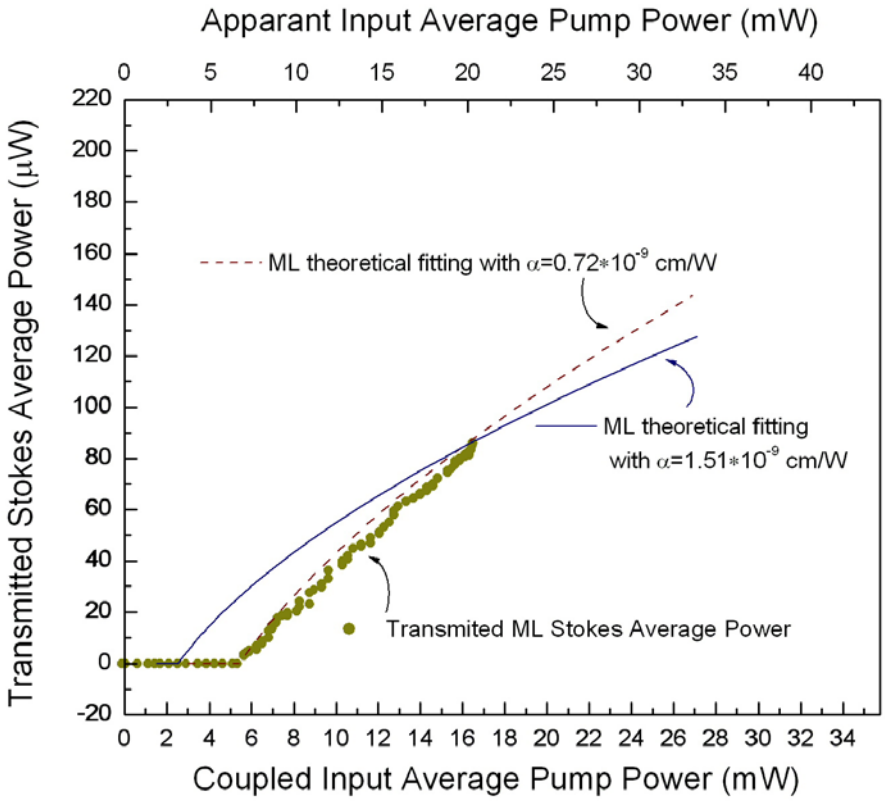

Figure 4-28. Experimental data and theoretical fits of the ML-ECDL pumped Raman laser. Solid circles are the cavity transmitted ML Stokes power. The solid line is the theoretical fit with plane wave gain coefficient α=1.51×10^{-9} cm/W . The dashed line is the theoretical fit with α=0.72×10^{-9} cm/W . In this case, the actual threshold is about 5.4 mW.

In order to achieve good frequency lock of the ML-ECDL to the HFC, it is necessary to match the FSRs of both the Raman cavity and the ECDL to the RF modulation frequency. Since the RF frequency is 840.66 MHz, the length of both these cavities needs to be 17.84 cm. This long length makes continuous tuning of the ECDL extremely difficult, even when running CW. Often, the laser needs coarse adjustments to the alignment. Even with this difficulty, when running CW, it is possible to tune the pump laser across the Raman gain profile because we can monitor the pump laser frequency on a wavemeter as we tune the pump laser. By checking both the frequency of the laser and the output Stokes power, we can tune the CW laser to the frequency that maximizes the output Stokes power, which, at powers below 4x threshold, is the line-center frequency of the Raman gain profile [28]. However, the wavemeter cannot determine the frequency of a ML laser because it is multi-mode. The loss of this tool makes it virtually impossible to tune the ML-ECDL to the line-center of the Raman profile since we have no reliable way to tune back to the previous frequency. In addition, the ML system is inherently a noisier system than the CW system, making it harder to determine if the output Stokes power is increasing or decreasing. There is also the added difficulty of keeping the RF modulation frequency matched with both cavity lengths, but especially the HFC, where a mismatch between the Raman cavity FSR and the RF frequency decreases the Stokes output because of the mismatch between the input pump frequency comb and cavity's resonance frequencies. After about 20 tries, the best alignment that we could achieve between the Stokes frequency and the Raman gain profile required that the plane-wave gain coefficient be decreased by a factor of 2.125 (to

α=0.72×10^{-9} cm/W) in order to obtain agreement between our theory and data, indicating that the Stokes was detuned from the line center frequency by roughly 250 MHz [20, 21]. In the future, a new method of tuning the ML-ECDL across the Raman resonance will be needed in order to maximize the output Stokes power.

The center wavelength of this ECDL is about 799 nm and we can obtain Stokes emission around 1196 nm as shown in figure 4-29. The resolution of the OSA is about 0.01 nm, larger than the separation between adjacent Stokes modes, and thus the OSA is unable to resolve the longitudinal modes.

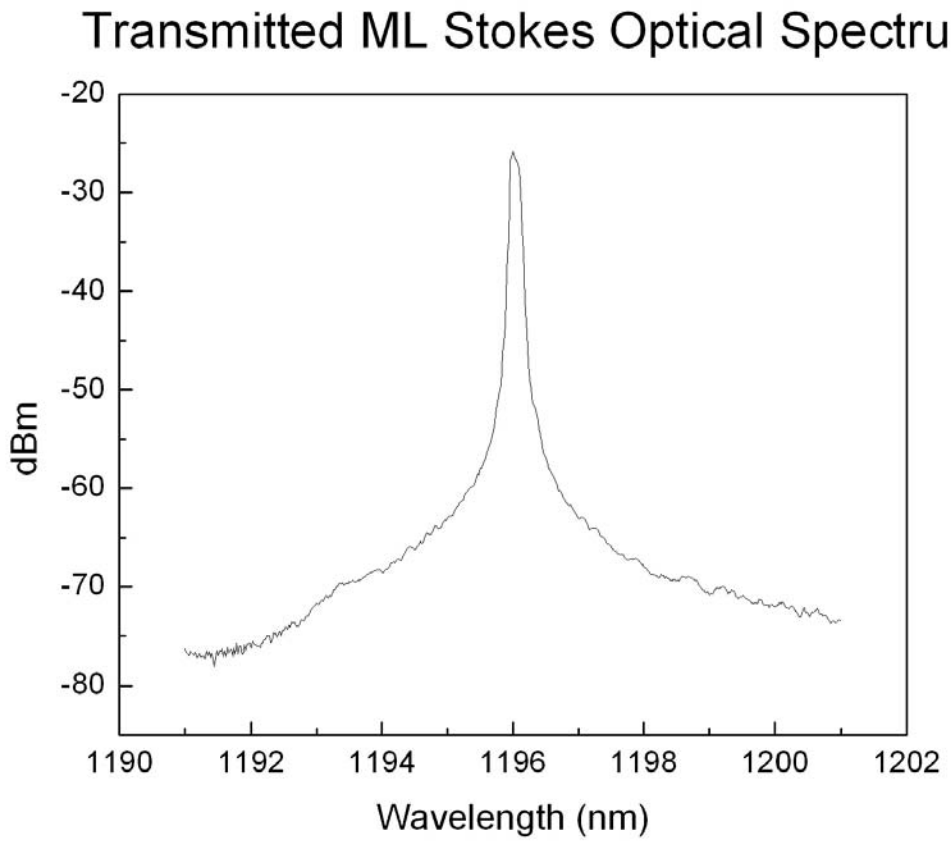

Figure 4-29. Transmitted ML Stokes optical spectrum.

However we can use a high speed photoreceiver and a RF spectrum analyzer to do a beat signal analysis between the Stokes modes. When the average input pump power is about twice the CW threshold power, figure 4-30 shows the beat signals of the transmitted pump with 50 KHz bandwidth. The eight harmonic signals correspond to at least nine longitudinal pump modes. If those nine modes are random in phase or without four-wave-mixing enhancement, then the average input pump power needs to be at least nine times the threshold of CW case in order to make all the modes lase. Figure 4-31 shows the seven harmonic beat signals from the transmitted Stokes, which means eight Stokes modes are lasing through four-wave-mixing processes. The eighth harmonic beat signal (or the ninth Stokes mode) is not shown here, we think this signal is too week for the RF spectrum analyzer. The Stokes harmonic beat signal is strong evidence to show that if the pump modes are in-phase, they can augment each other through four-wave-mixing processes causing all of them to lase. We also considered producing Stokes optical spectrum based on the beating signal, however due to the uneven frequency response of the photoreceiver, challenge of long-term stable frequency locking and the Stokes output power fluctuation, the result can not be very accurate. Figure 4-32 shows the temporal pulses of the input pump, transmitted pump and transmitted Stokes beams measured by a digital real time oscilloscope (Tektronix TDS 694C). With roughly 220ps input pump pulse full width half maximum (FWHM), the transmitted pump and Stokes pulses are 260ps and 310ps. According to our theory, the widths of the output pump and Stokes beams are wider than the input because, in this pressure region, the transmitted longitudinal modes are slightly out of phase [29].

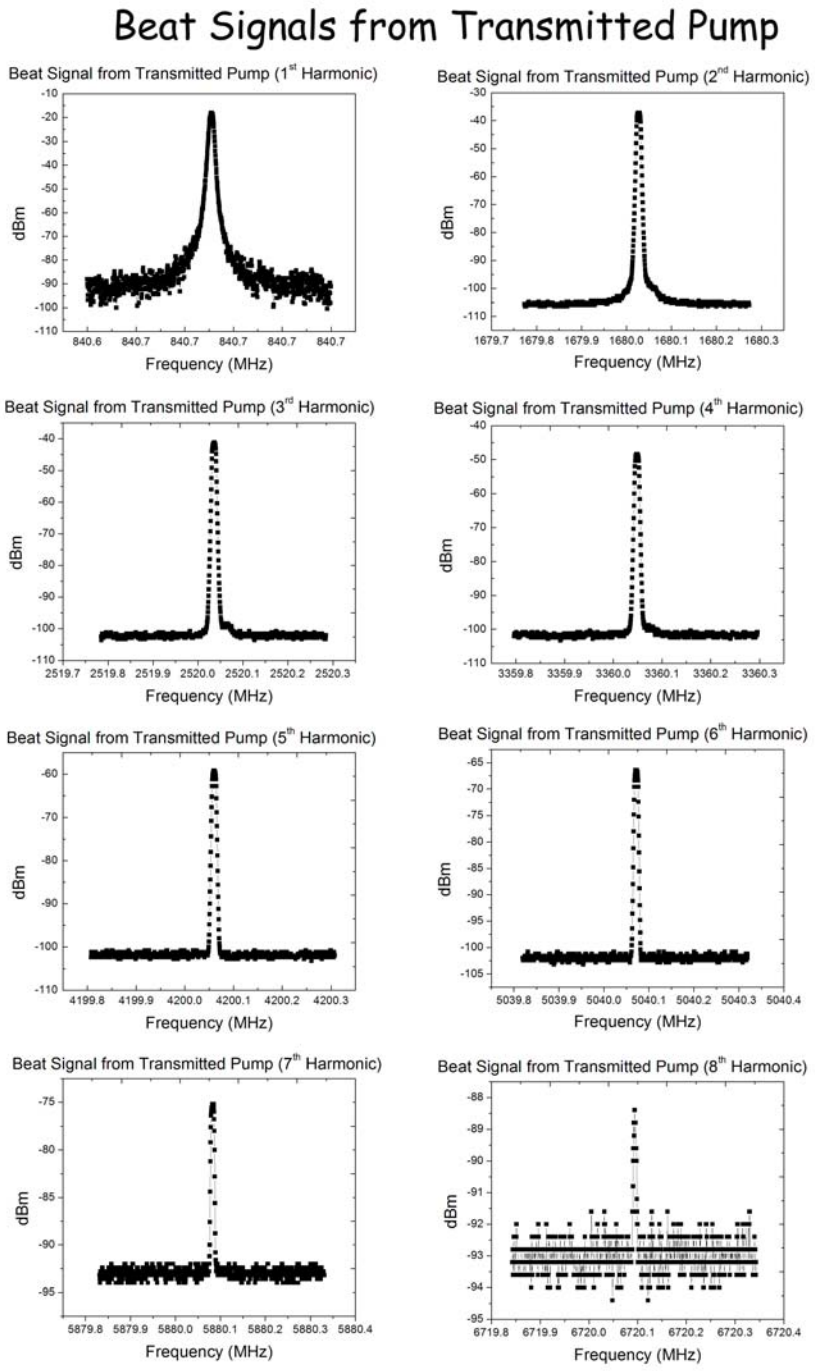

Figure. 4-30. Beat signals from the transmitted pump. There are eight harmonic signals with the first at around 840.66 MHz (RF modulation frequency), which means the transmitted pump pulse is made of at least nine longitudinal modes.

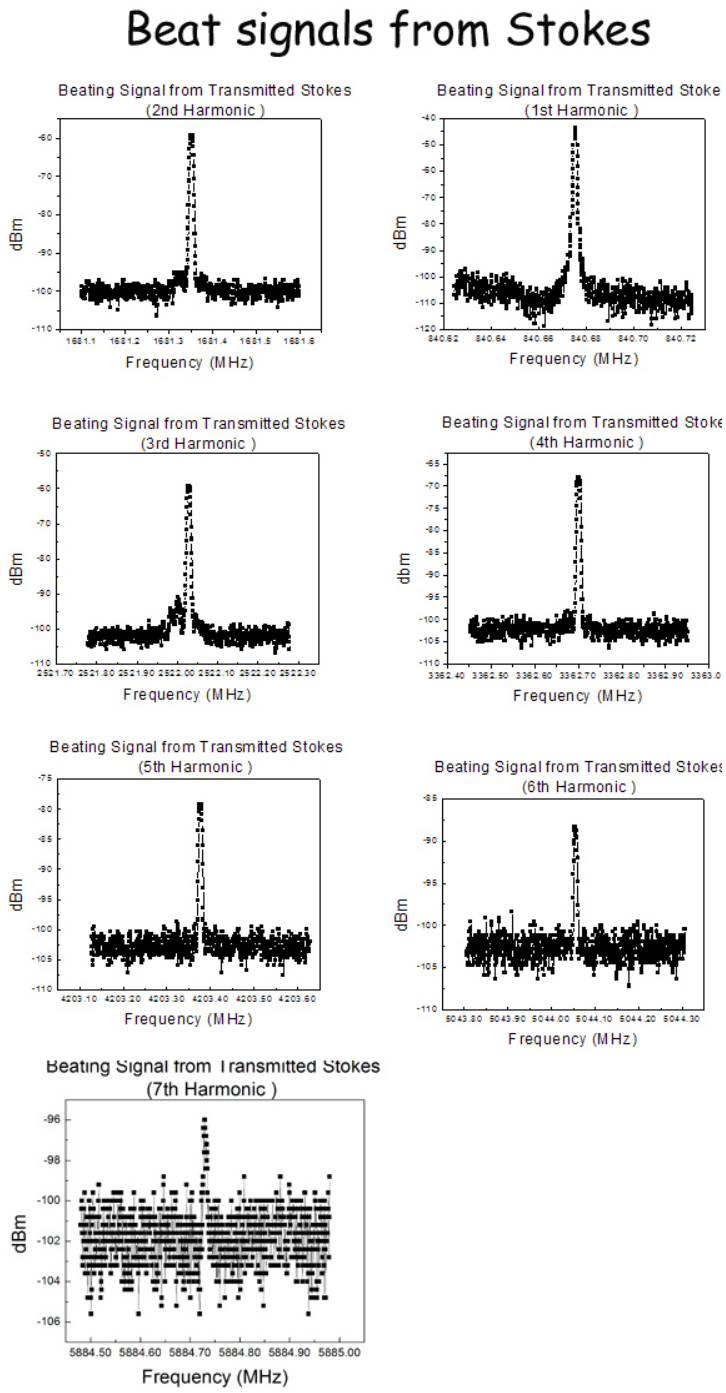

Figure 4-31. Beat signals from the transmitted Stokes. There are seven harmonic signals with the first at around 840.66 MHz (RF modulation frequency), which means the transmitted Stokes pulse is made of at least nine longitudinal modes.

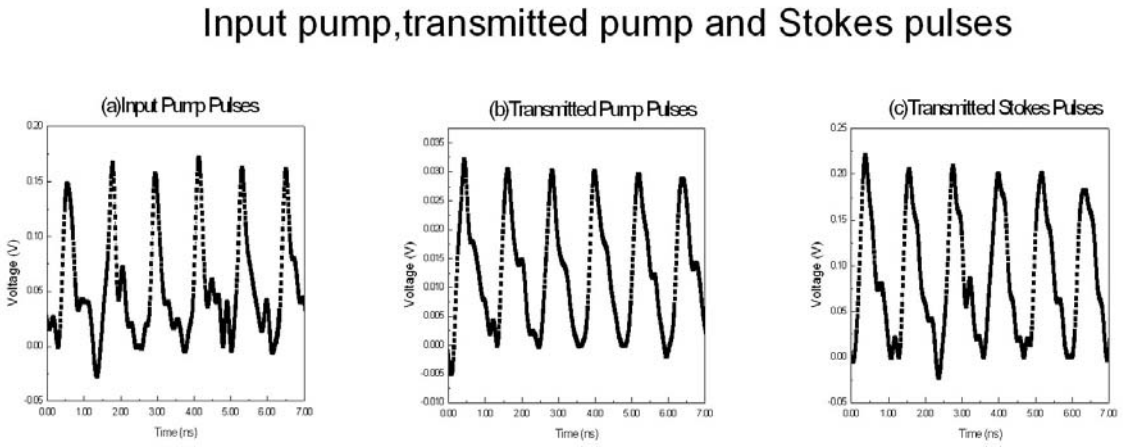

Figure 4-32. Temporal pulses of the input pump, transmitted pump and transmitted Stokes beams.

Conclusion of the Raman Experiments

In this chapter, we experimentally demonstrated a far off resonance mode-locked Raman laser pumped by an actively ML-ECDL in the medium pressure region. First we built a ML-ECDL as a pump source at 800 nm which can be tuned 25 nm by tilting the grating. Mode-locking is achieved by modulating the laser threshold DC current with an 18 dBm RF signal at 840.667 MHz, which is near the free spectral range associated with the 17.78 cm long cavity. The output power of this ML-ECDL is about 2 mW. In order to increase the pump power (2－35 mW), a simple, stable and compact TA diode system was designed and built. The amplified light maintained the same optical spectrum of the seeding light. After being amplified by the TA, the mode suppression was roughly 38 dB for CW seeding and 32 dB for ML seeding, which equals the mode suppression of the

seeding CW-ECDL and the ML-ECDL. With 0.75 mW average seeding power, 80 mW average power can be achieved by driving the TA at 1.75 Amps and 18^{o}C. Then the ML-ECDL was frequency locked to the HFC by the Pound-Drever-Hall technique. In order to adequately couple all of the laser's longitudinal modes from the ML-ECDL into the HFC, three steps were taken. First the ML-ECDL noise level must be minimized. Next the RF frequency driving the mode locked laser must be close to the FSR of the HFC (within kHz). Finally, the laser cavity's length must be finely tuned to match the HFC length to optimize the whole system.

Our first Raman laser experiments were done with a CW pump laser. This allowed us to compare with previous experiments done in this laboratory. As found in these earlier experiments, we verified that the CW Raman laser performance agreed very well with the CW Raman theory and found the threshold is 3.89 mW.

In studying the mode-locked Raman laser in the medium pressure region, we started with nine longitudinal pump modes, which when operating at an average power level slightly above the CW threshold (3.89 mW), each of the pump modes, taken on its own, was below the CW lasing threshold. If these nine pump modes were independent of each other, they would each have a threshold of 3.89 mW giving a combined threshold of ~35mW. However, because the pump modes were phase-locked together, they could augment each other through four-wave-mixing processes, decreasing the mode-locked threshold from 35 mW to 5.4 mW.

For the medium pressure regime that we could study, the threshold expected for our mode-locked diode laser was 36% below the CW threshold, while experimentally we

observed 38.8% above the CW threshold. In support of this conclusion, we found that when we decreased the Raman gain in our theory by a factor of 2.125 (α=0.72×10^{-9} cm/W), the theory agreed well with the experimental data. A possible explanation for this discrepancy lied in a combination of the Raman thermal lens effect and the Stokes cavity modes not being perfectly centered under the Raman gain profile. After many experimental attempts, we concluded that a new method of tuning the mode locked diode pump laser across the Raman resonance will be needed to verify the theory more accurately.

During our experiments we also studied the predicted spectral output for the mode-locked Raman laser. To do this we studied the beat signal from the mode-locked Raman laser output on a RF spectrum analyzer. The Stokes harmonic beat signal was strong evidence to show that even though the individual pump modes are below threshold, if the pump modes are in-phase, they can augment each other through four-wave-mixing processes causing all of them to lase. In addition, the observed 310 ps temporal pulse train on a fast oscilloscope was further evidence that Stokes output was mode-locked.

References

1. K. C. Harvey, C. J. Myatt, "External-cavity diode laser using a grazing-incidence diffraction grating," *Opt. Lett.* 16, 910-912 (1991).

2. S. Lecomte, E. Fretel, G. Mileti and P. Thomann, "Self-Aligned Extended-Cavity Diode Laser Stabilized by the Zeeman Effect on the Cesium D 2 Line," *Appl. Opt.* 39, 1426-1429 (2000).

3. S. Arnold, J. S. Wilson, and M. G. Boshier, "A simple extended-cavity diode laser," *Rev. Sci. Instrum.* 69, 1236-1239 (1998).

4. L. Ricci, M. Weidemüller, T. Esslinger, A. Hemmerich, C. Zimmermann, V. Vuletic, W. König and T. W. Hänsch, "A compact grating-stabilized diode laser system for atomic physics," *Opt. Commun.* 117, 541-549 (1995).

5. T. Hof, D. Fick and H. J. Jänsch, "Application of diode lasers as a spectroscopic tool at 670 nm," *Opt. Commun.* 124, 283-286 (1996).

6. Y. Xiong, S. Murphy, K. Repasky and J. L. Carlsten, "Frequency Stabilization of a Mode-locked External Cavity Diode Laser to a High Finesse Cavity," *Opt. Eng*. 46(5), 054203, 2007.

7. E. D. Black, "An introduction to Pound-Drever-hall laser frequency stabilization," *Am. J. Phys*. 69 (1), January 2001.

8. M. Zhu and J. L. Hall, "Stabilization of optical phase/frequency of a laser system: application to a commercial dye laser with an external stabilizer," *JOSA B*, Volume 10, Issue 5, 802, May 1993.

9. T. Yilmaz, C. M. DePriest, P. J. Delfyett, J. H. Abeles, A. M Braun, "Stabilization of a mode-locked semiconductor laser optical frequency comb using the Pound-Drever-Hall scheme," Enabling Photonic Technologies for Aerospace Applications V. Edited by Pirich, Andrew R.; Taylor, Edward W.; Hayduk, Michael J. *Proceedings of the SPIE*, Volume 5104, pp. 18-23, 2003.

10. P. J Delfyett and C.H Lee, "High peak power picosecond pulse generation for AlGaAs external cavity mode-locked semiconductor laser and traveling-wave amplifier," *Appl. Phys. Lett,* 57(10), 971-973(1990).

11. D. Voigt, E.C. Schilder, R.J.C. Spreeuw, H.B Van Linden van den Heuvell, "Characterization of a high-power tapered semiconductor amplifier system," *Appl. Phys. B* 72, 279-284 (2001).

12. S. Gee, G Alphonse, J. Connolly, and Peter J. Delfyett, "High-power Mode-locked External Cavity Semiconductor Laser Using Inverse Bow-Tie Semiconductor Optical Amplifiers," *IEEE Journal of Selected Topics in Quantum Electronics*, 4(2), 209-215 (1998).

13. Baltuska, Z. Wei, M. S. Pshenichnikov, and D. A. Wiersma, "Optical pulse compression to a 5 fs at 1-MHz repetition rate," *Opt. Lett.* 22(2), 102-104 (1997).

14. K. Repasky, J. Shaw, J. Carlsten, M. Obland, L. Meng and D. Hoffman, "Diode laser transmitter for water vapor DIAL measurements," IEEE International Geoscience and Remote Sensing, 3, 1947-1950 (2004).

15. Y. Xiong, S. Murphy, K. Repasky and J. L. Carlsten, "Design and characteristics of a tapered amplifier diode system by seeding with continuous-wave and mode-locked external cavity diode laser," *Opt. Eng*. 45(12), 124205, 2006.

16. G. D. Boyd, W. D. Johnson and I. P. Kaminow, *IEEE J. Quant. Elec., Vol. 4, p. 203*, 1969.

17. J. K. Brasseur, P. A. Roos, K.S. Repasky and J. L. Carlsten, "Characterization of a continuous-wave Raman laser in H_2," *J. Opt. Soc. Am. B*, vol. 16, No. 8, August 1999.

18. To conserve energy the areas for the pump and the Stokes beams, used to calculated power, need to be identical and are normalized to the pump beam.

19. H. Kogelnik and T. Li, "Beams, modes, and resonators," in Handbook of Lasers, R. J. Pressley, Ed. Cleveland, OH: Chemical rubber Co., p. 426, 1971.

20. W. K. Bischel and M. J. Dyer, "Wavelength dependence of the absolute Raman gain coefficient for the Q (1) transition in H_2," *J. Opt. Soc. Am. B*, vol. 3, No. 5, May 1986.

21. W. K. Bischel and M. J. Dyer, "Temperature dependence of the Raman lindewidth and line shift for the Q (1) and Q (0) transitions in normal and para-H_2," *Phys. Rev. A*, Vol. 33, No. 5, May 1986.

22. Manufacture's data shows $R_{p(s)} \approx 0.99980$, $T_p = 40 \pm 5$ ppm and $T_s = 30 \pm 5$ ppm.

23. L. S. Meng, K. S. Repasky, P. A. Roos, and J. L. Carlsten, "Widely tunable continuous wave Raman laser in diatomic hydrogen pumped by an external cavity diode laser," *Opt. Lett*. 25, 472 2000.

24. Below the Stokes threshold, the reflected pump power P_r and the transmitted pump power P_t are both linear functions of the incident pump power: $P_r = K_r P_{io}$ and $P_t = K_t P_{io}$, where $K_r = [R(1-T-R)^2/(1-R)^2]C + R(1-C)$ and $K_t = [T^2/(1-R)^2]C$ are two constants related to mirror reflectivity R, transmission T, and cavity coupling efficiency C. From the data below threshold in figure 4-25, we found that $K_t = 0.057$. Using $R = 0.99983$ from the ringdown measurement and $T \approx 45$ ppm from the manufacture, we get C=81.3%.

25. We see eight harmonic beat signals from the pump source through RF spectrum analyzer, so the number of pump mode is at least nine.

26. The power ratio of these nine pump modes can get through scanning the HFC to resolve different modes when mismatching the RF synthesizer signal to the FSR of HFC. The ratio we use here is 0.4315:0.2538:0.2031:0.0761:0.01692:0.0152: 0.0017:0.0008:0.0008.

27. J. Bienfang, W. Rudolph, P. A. Roos, L. S. Meng, and J. L. Carlsten, "Steday-state thermo-optics model of a continuous-wave Raman laser," *J. Opt. Soc. Am. B* Vol. 19, pp. 1318-1325, 2002.

28. J. K. Brasseur, P. A. Roos, L. S. Meng and J. L. Carlsten, "Frequency tuning characteristics of a continuous-wave Raman laser in H_2," *J. Opt. Soc. Am. B* Vol. 17, No. 7, 1229-1232, 2000.

29. Y. Xiong, S. Murphy, K. Repasky and J. L. Carlsten, "Theory of a Far-Off Resonance Mode-Locked Raman Laser in H_2 with High Finesse Cavity Enhancement," *J. Opt. Soc. Am. B*, (accepted in April 2007).

CHAPTER 5

CONCLUDING REMARKS

In the past several years, the CW far-off resonance Raman laser with HFC enhancement has been studied both theoretically and experimentally. Because of the high reflectivity mirrors, the intra-cavity power can be enhanced by factor of tens of thousands and the threshold of the CW Raman laser system is on the mW level. Then instead of using CW pumping, if a pulsed source is used, the intra-cavity peak power may reach thousands of watts, which may lead to some interesting phenomena, like electromagnetically induced transparency. One way to build a pulse source is through mode-locking. Though we had a good understanding about how a single (CW) Stokes mode built up inside the cavity, we needed to investigate how the many modes from the mode-locked laser could help each other to grow through four-wave-mixing processes and also if the threshold of the mode-locked Raman laser system would still have a low threshold on the mW level.

In order to understand these phenomena, in this thesis, we studied for the first time a far-off-resonant mode-locked Raman laser in hydrogen with high finesse cavity enhancement. To do this we expanded the previous CW theory to include the effects of the mode locked pumping. Experimentally we designed and built a mode-locked Raman laser and to achieve the high powers needed for the experiment, developed a new design for a very stable and easy to align diode amplifier. We then used this mode-locked diode

oscillator-amplifier system to measure the experimental behavior of the mode-locked Raman laser and compared these measurements to our theoretical predictions.

Based on semiclasscial laser theory, the theory of this far-off resonance mode-locked Raman laser was derived in chapter 3. Depending on the relationship between the Raman linewidth and repetition rate of the pump source, we classified this problem into three regions: low pressure, medium pressure and high pressure. Simulation results, including time-dependent intra-cavity fields' amplitude and phase evolution and Stokes power versus input pump power, are shown in these different regions. All these pressure regions indicated that the individual longitudinal modes of the Raman laser would couple strongly to enhance the Raman gain over what would be expected from an individual longitudinal mode. However, the amount of this enhancement was predicted to depend on the pressure. The Raman gain profile is widest in the high pressure region and narrowest in the low pressure region; therefore, we predict that the high pressure region will have the strongest four-wave-mixing enhancement.

Of the three pressure regions, only the medium pressure region (~10 atm) was easily accessible to us experimentally because the high pressure region would require a complete redesign of the Raman cavity and in the low pressure region, the Raman gain profile narrows, making it difficult to find a cavity mode at the Stokes wavelength that will be above threshold. Thus, we were only able to compare our experimental results for the medium pressure region. Nonetheless, we still expected the threshold of the Raman laser in the medium pressure region to be lower than a single longitudinal mode (CW) pump.

Our first experiments were done with a CW pump laser. This allowed us to compare with previous experiments done in this laboratory. As found in these earlier experiments, we verified that the CW Raman laser performance agreed very well with the CW Raman theory.

In studying the mode-locked Raman laser, however, we found less agreement between the theory and the experiment. While the experiments indeed showed that there was significant gain enhancement between the longitudinal modes of the mode-locked Raman laser, the enhancement was not as much as the theory predicted. For the medium pressure regime that we could study, the threshold expected for our mode-locked diode laser was 36% below the CW threshold, while experimentally we observed 38.8% above the CW threshold. In support of this conclusion, we found that when we decreased the Raman gain in our theory by a factor of 2.125, the theory agreed well with the experimental data. A possible explanation for this discrepancy lied in a combination of the Raman thermal lens effect and the Stokes cavity modes not being perfectly centered under the Raman gain profile. After many experimental attempts we concluded that a new method of tuning the mode locked diode pump laser across the Raman resonance will be needed to verify the theory more accurately.

During our experiments we also studied the predicted spectral output for the mode-locked Raman laser. To do this we studied the beat signal from the mode-locked Raman laser output on a RF spectrum analyzer. The Stokes harmonic beat signal is strong evidence to show that even though the individual pump modes are below threshold, if the pump modes are in-phase, they can augment each other through four-wave-mixing

processes causing all of them to lase. In addition, the observed temporal pulse train on a fast oscilloscope is further evidence that Stokes output is mode-locked.

As mentioned earlier, in the future, a new method of tuning the ML-ECDL across the Raman resonance will be needed in order to maximize the output Stokes power and to probe the accuracy of the developed mode-locked Raman theory. Finally, we think there may be some interesting phenomena, like electromagnetically induced transparency, accessible in the high pressure region.

APPENDICES

APPENDIX A

DIVERGENCE OF THE POLARIZATION

The definition of the electric displacement in the medium is $\tilde{D} = \varepsilon_0 \tilde{E} + \tilde{P}$, where $\tilde{P}$ is the induced polarization. From Maxwell equations, we have $\nabla \bullet \tilde{D} = 0$ when there is no free charge.

In our case, the medium is hydrogen, which is isotropic, then the induced $\tilde{P}$ is parallel to $\tilde{E}$ with a coefficient of proportionality that is independent of direction: $\tilde{P} = \varepsilon_0 \chi_e \tilde{E}$. The constant χ_e is called the electric susceptibility of the medium. The displacement $\tilde{D}$ is therefore proportional to $\tilde{E}$, $\tilde{D} = \varepsilon \tilde{E}$, where $\varepsilon = \varepsilon_0 (1 + \chi_e)$ is the electric permittivity. The hydrogen gas is also uniform in the cavity, then ε is independent of position, $0 = \nabla \bullet \tilde{D} = \nabla \bullet (\varepsilon \tilde{E}) = \varepsilon \nabla \bullet \tilde{E}$, so $\nabla \bullet \tilde{E} = 0$ and $\nabla \bullet \tilde{P} = 0$.

APPENDIX B

LAPLACIAN OF THE ELECTRIC FIELD

Let us assume the laser field is propagating along the $\hat{z}$ direction, we have $\tilde{E} = (E_x\hat{x} + E_y\hat{y} + E_z\hat{z})e^{i(k_z z-\omega t)}$. From the definition, $\nabla^2\tilde{E} = \frac{\partial^2\tilde{E}}{\partial x^2} + \frac{\partial^2\tilde{E}}{\partial y^2} + \frac{\partial^2\tilde{E}}{\partial z^2}$. The three second derivatives are as following:

$$\frac{\partial^2\tilde{E}}{\partial x^2} = (\frac{\partial^2 E_x}{\partial x^2}\hat{x} + \frac{\partial^2 E_y}{\partial x^2}\hat{y} + \frac{\partial^2 E_z}{\partial x^2}\hat{z})e^{i(k_z z-\omega t)} \tag{B.1}$$

$$\frac{\partial^2\tilde{E}}{\partial y^2} = (\frac{\partial^2 E_x}{\partial y^2}\hat{x} + \frac{\partial^2 E_y}{\partial y^2}\hat{y} + \frac{\partial^2 E_z}{\partial y^2}\hat{z})e^{i(k_z z-\omega t)} \tag{B.2}$$

$$\begin{aligned}\frac{\partial^2\tilde{E}}{\partial z^2} = &[\frac{\partial^2 E_x}{\partial z^2} + (2ik_z)\frac{\partial E_x}{\partial z} + (ik_z)^2 E_x]e^{i(k_z z-\omega t)}\hat{x} \\ &+[\frac{\partial^2 E_y}{\partial z^2} + (2ik_z)\frac{\partial E_y}{\partial z} + (ik_z)^2 E_y]e^{i(k_z z-\omega t)}\hat{y} \\ &+[\frac{\partial^2 E_z}{\partial z^2} + (2ik_z)\frac{\partial E_z}{\partial z} + (ik_z)^2 E_z]e^{i(k_z z-\omega t)}\hat{z}\end{aligned} \tag{B.3}$$

In the $\hat{x}$ component of the $\frac{\partial^2\tilde{E}}{\partial z^2}$, we have $\frac{\partial^2 E_x}{\partial z^2} \ll (ik_z)^2 E_x \sim \frac{E_x}{\lambda^2}$ because E_x along the $\hat{z}$ direction is slowly varying on the scale of an optical wavelength, so is the reason for $(2ik_z)\frac{\partial E_x}{\partial z} \ll (ik_z)^2 E_x$. In other words, the dominant term for the $\hat{x}$ component of the $\frac{\partial^2\tilde{E}}{\partial z^2}$ is $(ik_z)^2 E_x e^{i(k_z z-\omega t)}$.

Now let us compare the $\hat{x}$ component of the $\frac{\partial^2\tilde{E}}{\partial x^2}$ and $\frac{\partial^2\tilde{E}}{\partial y^2}$ with $(ik_z)^2 E_x e^{i(k_z z-\omega t)}$. We also have $\frac{\partial^2 E_x}{\partial x^2} \ll (ik_z)^2 E_x \sim \frac{E_x}{\lambda^2}$ and $\frac{\partial^2 E_x}{\partial y^2} \ll (ik_z)^2 E_x \sim \frac{E_x}{\lambda^2}$

because $E_{x(y)}$ along the $\hat{x}(\hat{y})$ direction is slowly varying on the scale of an optical wavelength too.

The same arguments can be used for $\hat{y}$ and $\hat{z}$ components. So we can say the dominant term of the $\nabla^2\tilde{E}$ is from $\frac{\partial^2\tilde{E}}{\partial z^2}$, or $\nabla^2\tilde{E}=\frac{\partial^2\tilde{E}}{\partial z^2}$.

APPENDIX C

SOLUTION TO THE COHERENCE QUEATION

For the linear first order differential equation $y' + f(t)y = g(t)$, the general solution is $y(t) = e^{-\int^t f(x)dx}[\int^t e^{\int^z f(x)dx} g(z)dz + C]$. Rewrite Eq. (3.13) as $\dot{\sigma}_{31} = (-\gamma_0)\sigma_{31} + i(A + B_1 e^{-i\omega_1 t} + B_2 e^{i\omega_1 t} + C_1 e^{-i\omega_2 t} + C_2 e^{i\omega_2 t})$, where A, B_1, B_2, C_1 and C_2 are constants and $A \approx B_1 \approx B_2 \approx C_1 \approx C_2$, $\gamma_0 \sim \omega_1 \ll \omega_2$. The solution for this equation is

$$\begin{aligned}
\sigma_{31} &= e^{-\int^t \gamma_0 dx}[\int^t e^{\int^z \gamma_0 dx} i(A + B_1 e^{-i\omega_1 z} + B_2 e^{i\omega_1 z} + C_1 e^{-i\omega_2 z} + C_2 e^{i\omega_2 z})dz + C] \\
&= ie^{-\gamma_0 t}[\int^t e^{-\gamma_0 z}(A + B_1 e^{-i\omega_1 z} + B_2 e^{i\omega_1 z} + C_1 e^{-i\omega_2 z} + C_2 e^{i\omega_2 z})dz + C] \\
&= -ie^{-\gamma_0 t}[\frac{Ae^{-\gamma_0 t}}{\gamma_0} + \frac{B_1 e^{-(\gamma_0+\omega_1)t}}{(\gamma_0+\omega_1)} + \frac{B_2 e^{-(\gamma_0-\omega_1)t}}{(\gamma_0-\omega_1)} + \frac{C_1 e^{-(\gamma_0+\omega_2)t}}{(\gamma_0+\omega_2)} + \frac{C_2 e^{-(\gamma_0-\omega_2)t}}{(\gamma_0-\omega_2)}]
\end{aligned}$$

If $A \approx B_1 \approx B_2 \approx C_1 \approx C_2$ and $\gamma_0 \sim \omega_1 \ll \omega_2$, then $\frac{C_1 e^{-(\gamma_0+\omega_2)t}}{(\gamma_0+\omega_2)} \ll \frac{B_1 e^{-(\gamma_0+\omega_1)t}}{(\gamma_0+\omega_1)}$ and $\frac{C_2 e^{-(\gamma_0-\omega_2)t}}{(\gamma_0-\omega_2)} \ll \frac{B_1 e^{-(\gamma_0-\omega_1)t}}{(\gamma_0-\omega_1)}$, so $\sigma_{31} = -ie^{-\gamma_0 t}[\frac{Ae^{-\gamma_0 t}}{\gamma_0} + \frac{B_1 e^{-(\gamma_0+\omega_1)t}}{(\gamma_0+\omega_1)} + \frac{B_2 e^{-(\gamma_0-\omega_1)t}}{(\gamma_0-\omega_1)}]$. This is the same solution of equation $\dot{\sigma}_{31} = (-\gamma_0)\sigma_{31} + i(A + B_1 e^{-i\omega_1 t} + B_2 e^{i\omega_1 t})$ and shows how we can drop all the fast oscillation terms.

APPENDIX D

PHASE MISMATCH CALCULATION

To produce E_{s1}, the four-wave-mixing term $E_{p1}(E_{p2}^{*}E_{s2})$ should have a phase mismatch term as $\frac{1}{L}\int_{0}^{L} e^{-i[(k_{p1}-k_{s1})-(k_{p2}-k_{s2})]z}dz$. Since $[(k_{p1}-k_{s1})-(k_{p2}-k_{s2})]$ is on the order of 10^{-4} and L is about 0.18 m, the whole integral goes to 1. Thus, no phase mismatch terms need to be considered.

APPENDIX E

MATLAB PROGRAMS

Intra-cavity Fields' Time Evolution

```
function Multi_mode_Ramman(t,y)
clear
global M Gama_31 Es Ep initial_condition Epin w_RF l F dispersion
Dispersion_pump_equation Dispersion_stokes_equation kp Lp Ls g_p g_s
g_31 Gama_31 k_pump k_stokes

for M=1:9            % number of mode
M
a=1;                 % define the Gama_31(Raman linewidth)
b=9;                 % define the Gama_31(Raman linewidth)
Gama_31=a*10^b;      % dephase rate 1GHz
l=0.1778;            % cavity length 17.78 cm
c=3*10^8;            % speed of light
w_RF=c/2/l;          % RF frequency (repetition rate of the ML-ECDL)
[Gama_31,w_RF];

if b<9               % if b<<9, in the low pressure region
    p_dis='low';
elseif b==9          % if b=9, in the medium pressure region
    p_dis='medium';
else                 % if b>>9, in the high pressure region
    p_dis='high'
end

initial_p=zeros(1,M); % set initial phaser for the individual pump mode
initial_s=rand(1,M)*2*pi;% set initial phaser for the individual Stokes
mode
initial_condition=[initial_p,1*exp(i.*initial_s)];

Epin=4100                   % set the input pump field
t0=1000;                    % time span

savefile = [ int2str(Epin)  p_dis '_P_M='  int2str(M) 'unequal_ww.mat'];
% save data to file

options = odeset('RelTol',1e-4,'AbsTol',1e-7) ;
Rp=0.99983;                 % Reflectivity of pump
Rs=0.99980;                 % Reflectivity of stokes

Tp=42*10^(-6);              % Transmittance of pump
Ts=25*10^(-6);              % Transmittance of Stokes
afa=1.53*10^(-11);          % plane-wave gain coefficient

lamdap1=800*10^(-9);        % pump wavelength

Raman_shift=4155*3*10^10;   % Raman shift in hydrogen 4155 cm ^(-1)
lamda_v_p1=800*10^(-9);     % the first pump mode wavelength
```

```
ww=[5.1 3 2.4 0.9 0.2 0.18 0.02 0.01 0.01 ]/11.82;% the weight of 9
pump modes

for n=1:M
f_p(n)=c/lamda_v_p1- (n-1)*w_RF;% calculate individual pump mode
frequency
lamda_v_p(n)=c/f_p(n);% calculate individual pump mode wavelength
lamda_v_s(n)=c/(c/lamda_v_p(n)-Raman_shift);% calculate individual
Stokes mode wavelength
f_s(n)=c/lamda_v_s(n);% calculate individual Stokes mode frequency
weight(n)=ww(n);% individual input pump mode weight
end

e0=8.85*10^(-12);
u0=1.26*10^(-6);
h_ba=1.054*10^(-34);          % Joul*s
Lp=-c/2/l*(log(Rp));          % the losses that are due to mirrors
Ls=-c/2/l*(log(Rs));          % the losses that are due to mirrors
G=1/2*((1/8)*afa*c*((e0/u0)^(1/2)))*(2*lamda_v_p(1)/(lamda_v_p(1)+lamda
_v_s(1)));     % gain of system
w31=f_p(1)-f_s(1);
g=(G*2*h_ba*e0*Gama_31/w31)^0.5;

Esin=1;             % initial Stokes field due to spontaneous emission
for n=1:M
EEpin(n)=(weight(n))^(0.5)*Epin;
kp(n)=c/l*EEpin(n)*(Tp)^(1/2);
g_p(n)=f_p(n)*g/e0; % calcualte individual mode gain coefficient
g_s(n)=f_s(n)*g/e0;
g_31=g/(2*h_ba);
end

no = 0.000136075;       % Index at zero frequency, 1 atm, and 273 K
bo = 2.69852 * 10^-22;  % Linear correction coefficient
co = 1.16021 * 10^-35;  % Quadratic correction coefficient

P = 10;             %  H2 pressure in cavity (atm)
T = 300;            %  Temperature in cavity (K)


%  The index of refraction takes on the following form: n = A + B*f +
%  C*f^2 where A, B, and C are definded by:
an = 1 + no*P*273/T;
bn = bo*P*273/T;
cn = co*P*273/T;



f_pump = c./lamda_v_p;            % Pump frequency (Hz)
f_stokes = c./lamda_v_s;          % Pump frequency (Hz)
n_pump = an + bn.*f_pump + cn.*f_pump.^2;% Pump index of refraction
```

```
n_stokes = an + bn.*f_stokes + cn.*f_stokes.^2;% Pump index of
refraction
k_pump=2*pi*n_pump./lamda_v_p;
k_stokes=2*pi*n_stokes./lamda_v_s;

[T,Y] = ode23s(@MM_Ramman,[0 t0*10^(-6)],initial_condition,options);  %
ODE solver

figure              % plot
for nnn=1:M
    subplot(M,1,nnn)
    plot(T*10^6,abs(Y(:,nnn)),'*-',T*10^6,abs(Y(:,nnn+M)),'o-')
    hold
end

Ip=0;
Is=0;
for nnn=1:M
    Ip=Ip+abs(Y(end,nnn))^2;
    Is=Is+abs(Y(end,nnn+M))^2;
end  %for nnn=1:M
[Ip, Is]

save(savefile,'ww','Epin','Gama_31','w_RF','l','T','Y','Ip','Is','initi
al_condition')
end    %for M=1:1  % number of mode

%%%%%%%This calculation is based on the Eqs.(3.27)---(3.29)%%%%%%%%%%%%%
function dy = MM_Ramman(t,y)
global M Gama_31 Es Ep initial_condition Epin w_RF l F dispersion
Dispersion_pump_equation Dispersion_stokes_equation kp Lp Ls g_p g_s
g_31 Gama_31 k_pump k_stokes

dy = zeros(2*M,1);    % a column vector
for iiii=1:M;    % n=iiii
    AAAA(iiii)=0;
    BBBB(iiii)=0;


    for iii=1:M   % Beta=iii
        AAA(iii)=0;
        BBB(iii)=0;


        for ii=1:M  % alfa=ii
                if  ( ( ii-(iii-iiii) ) >0  )&( ( ii-(iii-iiii) ) <=M  )
                    AA=y( ii-(iii-iiii) )*   conj(y(ii+M))  ;  % p
field * S field

                    BB=conj(y(ii))*    (  y(ii-(iii-iiii) +M)  )  ;
% p field * S field;
```

```
                else %( ( ii-(iii-iiii) ) >0)&( ( ii-(iii-iiii)) <=M )
                        AA=0;
                        BB=0;

                end %( ( ii-(iii-iiii) ) >0)&(( ii-(iii-iiii) ) <=M  )

        AAA(iii)=AAA(iii)+AA;
        BBB(iii)=BBB(iii)+BB;

        end  %for ii=1:M  % alfa=ii
        AAAA(iiii)=AAAA(iiii)+AAA(iii)*y(iii+M)/( Gama_31+i*(iii-
iiii)*w_RF );
        BBBB(iiii)=BBBB(iiii)+BBB(iii)*y(iii)/( Gama_31+i*(iii-
iiii)*w_RF );

    end  %for iii=1:M   % Beta=iii
    dy(iiii)=kp(iiii)-Lp*y(iiii)-g_p(iiii)*g_31*AAAA(iiii);
    dy(iiii+M)=-Ls*y(iiii+M)+g_s(iiii)*g_31*BBBB(iiii);

end  %for iiii=1:M;
```

Intra-cavity Stokes Field as a Function as Input Pump

```
function Multi_mode_Ramman(t,y)

global M Gama_31 Es Ep initial_condition Epin w_RF l kp Lp Ls g_p g_s
g_31 Gama_31 k_pump k_stokes

for M=6:6  % number of mode
M
a=1;                % define the Gama_31(Raman linewidth)
b=9;                % define the Gama_31(Raman linewidth)
Gama_31=a*10^b;     % dephase rate 1GHz
l=0.1778;           % cavity length 17.78 cm
c=3*10^8;           % speed of light
w_RF=c/2/l;         % RF frequency (repetition rate of the ML-ECDL)
[Gama_31,w_RF];


    p_dis='medium';   % medium pressure
    if M==1
        Epinreference=5000;
        ww=1;

    elseif M==9
        Epinreference=6000;
```

```
        ww=[0.29 0.29 0.23 0.1 0.0583 0.0233]; % weight of six
individual pump input mode
    end

initial_p=zeros(1,M);% set initial phaser for the individual pump mode
initial_s=rand(1,M)*2*pi;% set initial phaser for the individual Stokes
mode
initial_condition=[initial_p,1*exp(i.*initial_s)];


nn_Epin=0;  % counter for Epin

for Ipin=[4500^2:10^5:Epinreference^2,Epinreference^2: 5*10^5 :6500^2]
% set the input pump field

Epin=Ipin^0.5
if Epin<Epinreference
    t0=15000;
else
t0=1500;
end  %% if Epin<2500

savefile = [ 'Threshold_'  p_dis '_P_M='  int2str(M) '.mat'];

Rp=0.99983;                 % Reflectivity of pump
Rs=0.99980;                 % Reflectivity of stokes

Tp=42*10^(-6);              % Transmittance of pump
Ts=25*10^(-6);              % Transmittance of Stokes
afa=1.53*10^(-11);          % plane-wave gain coefficient

lamdap1=800*10^(-9);       % pump wavelength
Raman_shift=4155*3*10^10;   % Raman shift in hydrogen 4155 cm ^(-1)
lamda_v_p1=800*10^(-9);     % the first pump mode wavelength

for n=1:M
f_p(n)=c/lamda_v_p1- (n-1)*w_RF;% calculate individual pump mode
frequency
lamda_v_p(n)=c/f_p(n);% calculate individual pump mode wavelength
lamda_v_s(n)=c/(c/lamda_v_p(n)-Raman_shift); % calculate individual
Stokes mode wavelength
f_s(n)=c/lamda_v_s(n);% calculate individual Stokes mode frequency
weight(n)=ww(n); % individual input pump mode weight
end

e0=8.85*10^(-12);
u0=1.26*10^(-6);
h_ba=1.054*10^(-34);          % Joul*s
Lp=-c/2/l*(log(Rp));          % the losses that are due to mirrors
Ls=-c/2/l*(log(Rs));          % the losses that are due to mirrors
```

```
G=
1/2*((1/8)*afa*c*((e0/u0)^(1/2)))*(2*lamda_v_p(1)/(lamda_v_p(1)+lamda_v
_s(1)));         % gain of system
w31=f_p(1)-f_s(1);
g=(G*2*h_ba*e0*Gama_31/w31)^0.5;

Esin=1;   % initial Stokes field due to spontaneous emission
for n=1:M
EEpin(n)=(weight(n))^(0.5)*Epin;
kp(n)=c/l*EEpin(n)*(Tp)^(1/2);
g_p(n)=f_p(n)*g/e0;     % calcualte individual mode gain coefficient
g_s(n)=f_s(n)*g/e0;
g_31=g/(2*h_ba);
end

no = 0.000136075;   % Index at zero frequency, 1 atm, and 273 K
bo = 2.69852 * 10^-22;  % Linear correction coefficient
co = 1.16021 * 10^-35;  % Quadratic correction coefficient

P = 10;             %  H2 pressure in cavity (atm)
T = 300;            %  Temperature in cavity (K)

%  The index of refraction takes on the following form: n = A + B*f +
%  C*f^2 where A, B, and C are definded by:
an = 1 + no*P*273/T;
bn = bo*P*273/T;
cn = co*P*273/T;

f_pump = c./lamda_v_p;          % Pump frequency (Hz)
f_stokes = c./lamda_v_s;          % Pump frequency (Hz)
n_pump = an + bn.*f_pump + cn.*f_pump.^2;% Pump index of refraction
n_stokes = an + bn.*f_stokes + cn.*f_stokes.^2;% Pump index of
refraction
k_pump=2*pi*n_pump./lamda_v_p;
k_stokes=2*pi*n_stokes./lamda_v_s;
options = odeset('RelTol',1e-4,'AbsTol',1e-7) ;
[T,Y] = ode23s(@MM_Ramman,[0 t0*10^(-6)],initial_condition,options);

Ip=0;
Is=0;
for nnn=1:M
    Ip=Ip+abs(Y(end,nnn))^2;
    Is=Is+abs(Y(end,nnn+M))^2;
end  %for nnn=1:M
[Ip, Is];

nn_Epin=nn_Epin+1;
Pumpinput_I(nn_Epin)=Ipin;
Stokesoutput_I(nn_Epin)=Is;
Pumpoutput_I(nn_Epin)=Ip;
plot(Ipin,Is,'*');
hold on
```

```
end % for Ipin=[1500^2:10^5:2500^2,2500^2:5*10^5:6000^2]
save(savefile,'ww','Gama_31','w_RF','l','Pumpinput_I','Stokesoutput_I',
'Pumpoutput_I')
clear Pumpinput_I Stokesoutput_I Pumpoutput_I
end    %for M=1:1  % number of mode


%%%%%%%This calculation is based on the Eqs.(3.27)---(3.29)%%%%%%%%%%%%
function dy = MM_Ramman(t,y)
global M Gama_31 Es Ep initial_condition Epin w_RF l kp Lp Ls g_p g_s
g_31 Gama_31 k_pump k_stokes

dy = zeros(2*M,1);    % a column vector
for iiii=1:M;    % n=iiii
    AAAA(iiii)=0;
    BBBB(iiii)=0;

    for iii=1:M   % Beta=iii
        AAA(iii)=0;
        BBB(iii)=0;

        for ii=1:M  % alfa=ii
                if  ( ( ii-(iii-iiii) ) >0  ) &  ( ( ii-(iii-iiii) )
<=M  )
                      AA=y( ii-(iii-iiii) )*   conj(y(ii+M))  ;  % p
field * S field
                      BB=conj(y(ii))*    (  y(ii-(iii-iiii) +M)  )  ;
% p field * S field;

                else %( ( ii-(iii-iiii) )>0 )&( ( ii-(iii-iiii) ) <=M  )
                      AA=0;
                      BB=0;

                end %( ( ii-(iii-iiii))>0)&( ( ii-(iii-iiii) ) <=M  )

                AAA(iii)=AAA(iii)+AA;
                BBB(iii)=BBB(iii)+BB;
        end  %for ii=1:M  % alfa=ii
        AAAA(iiii)=AAAA(iiii)+AAA(iii)*y(iii+M)/( Gama_31+i*(iii-
iiii)*w_RF );
        BBBB(iiii)=BBBB(iiii)+BBB(iii)*y(iii)/( Gama_31+i*(iii-
iiii)*w_RF );
   end  %for iii=1:M   % Beta=iii
    dy(iiii)=kp(iiii)-Lp*y(iiii)-g_p(iiii)*g_31*AAAA(iiii);
    dy(iiii+M)=-Ls*y(iiii+M)+g_s(iiii)*g_31*BBBB(iiii);

end  %for iiii=1:M;
```

APPENDIX F

MECHANICAL DESIGN OF THE TAPERED AMPLIFIER DIODE SYSTEM

Assembly

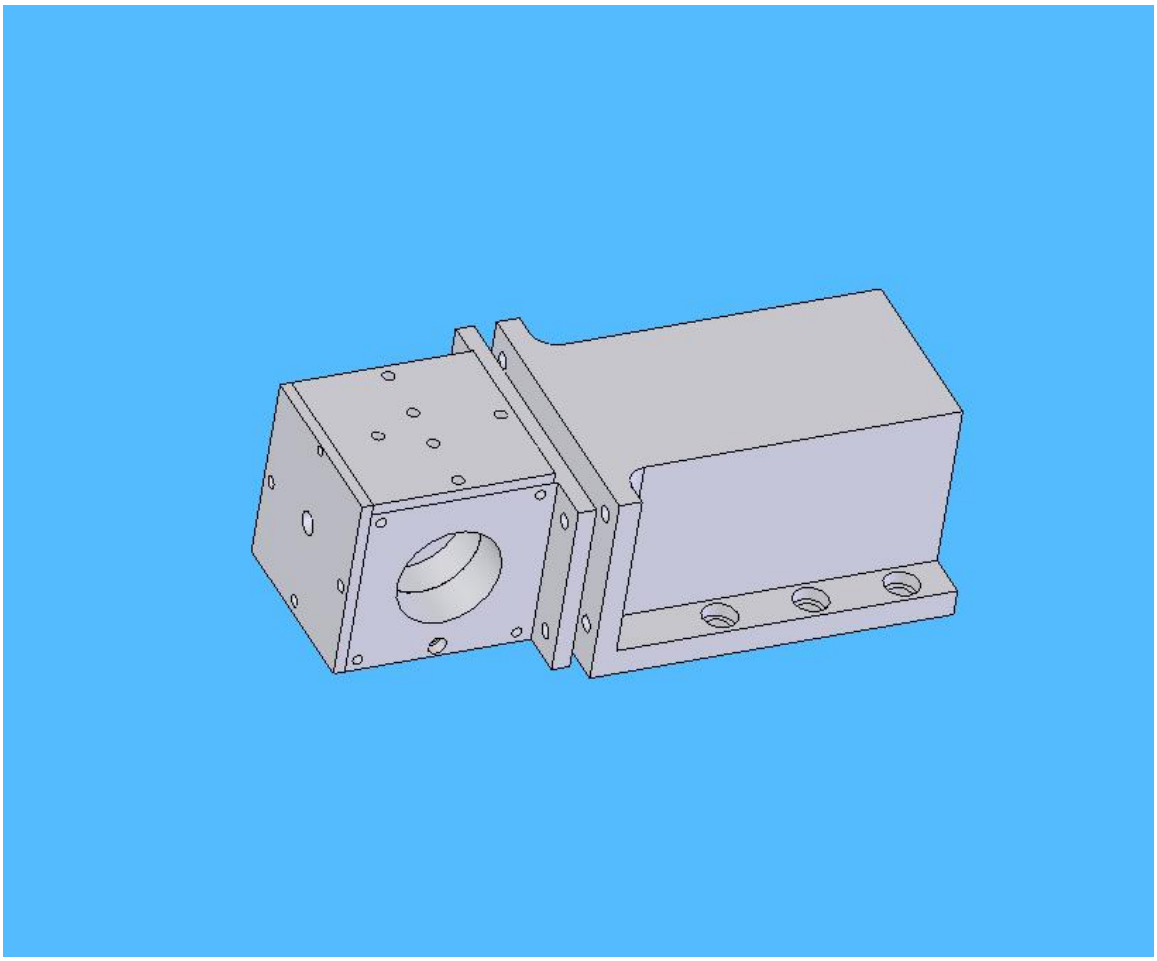

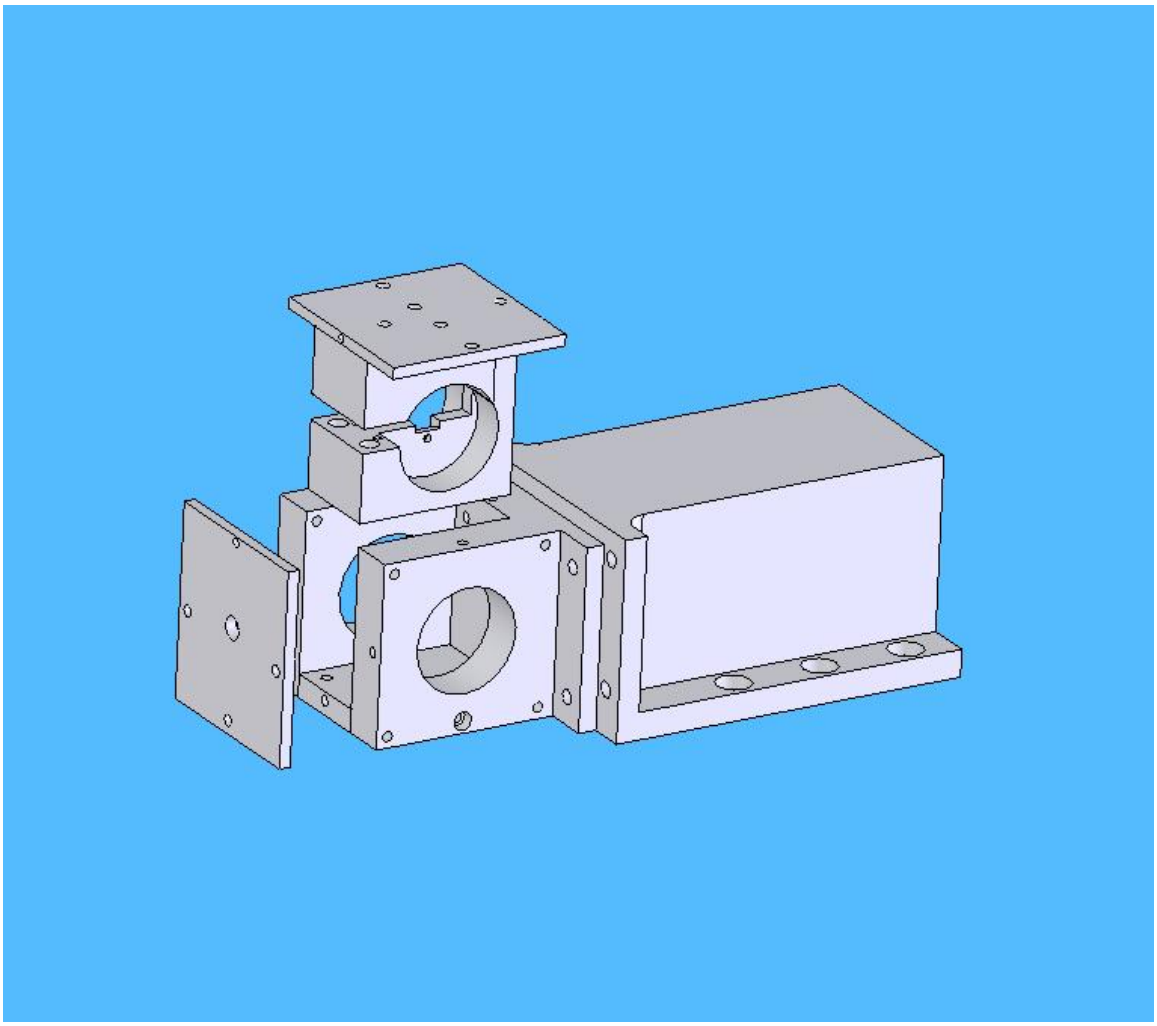

Tapered Amplifier Diode Holder

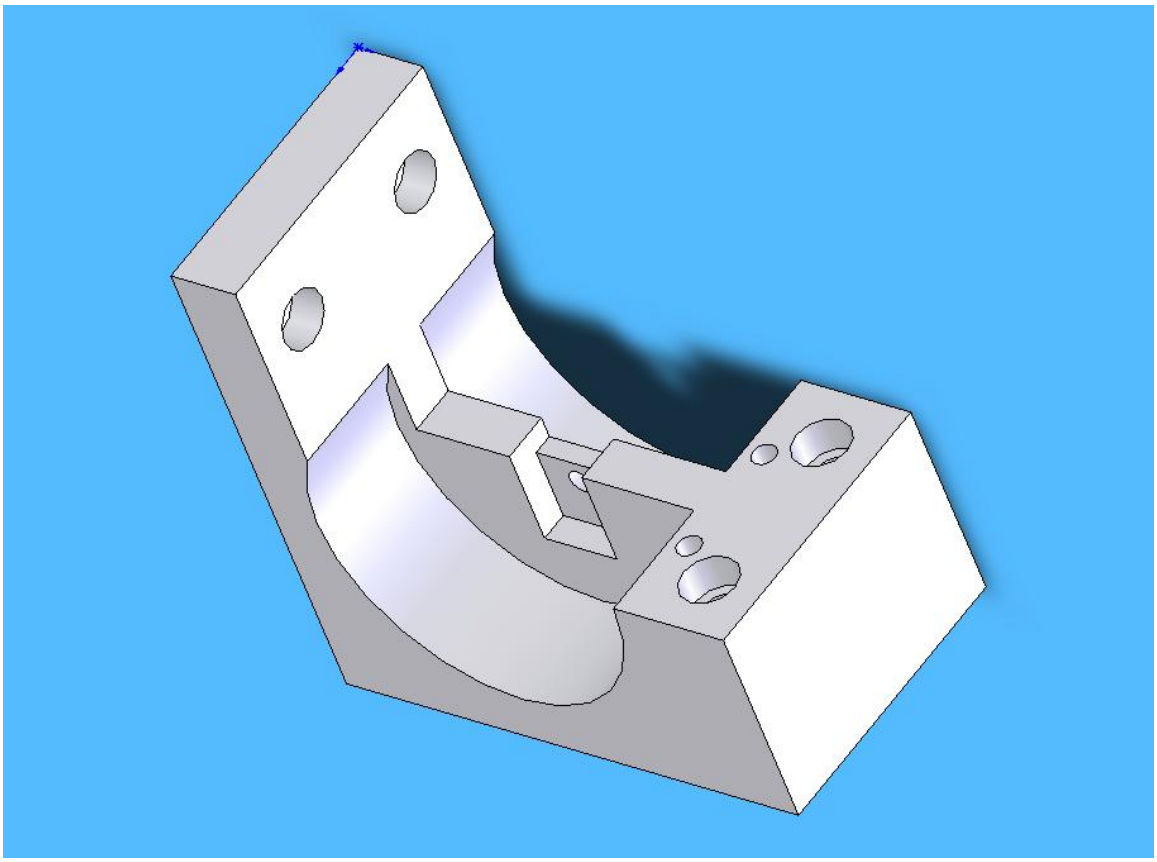

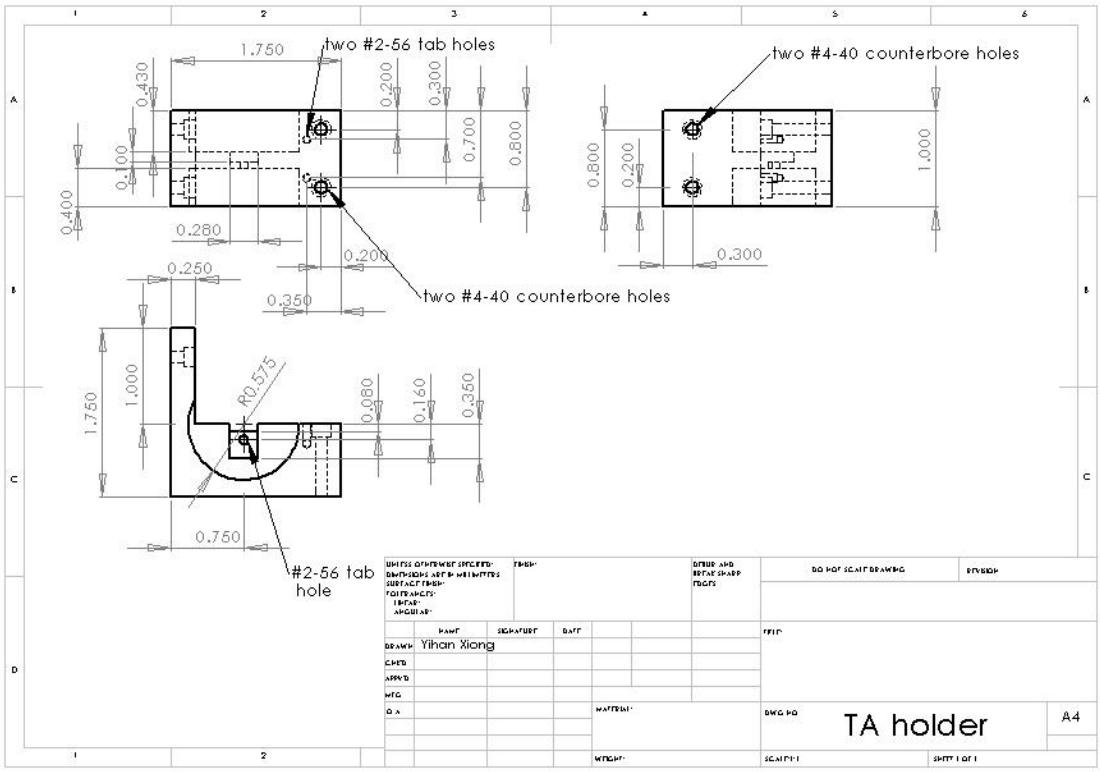
two #2-56 tab holes
two #4-40 counterbore holes
two #4-40 counterbore holes
#2-56 tab hole
1.750
0.430
0.100
0.400
0.280
0.200
0.300
0.700
0.800
0.250
0.350
1.000
1.750
R0.575
0.080
0.160
0.350
0.750
0.800
0.200
0.300
1.000
Yihan Xiong
TA holder
A4

Housing for the Tapered Amplifier Diode Holder

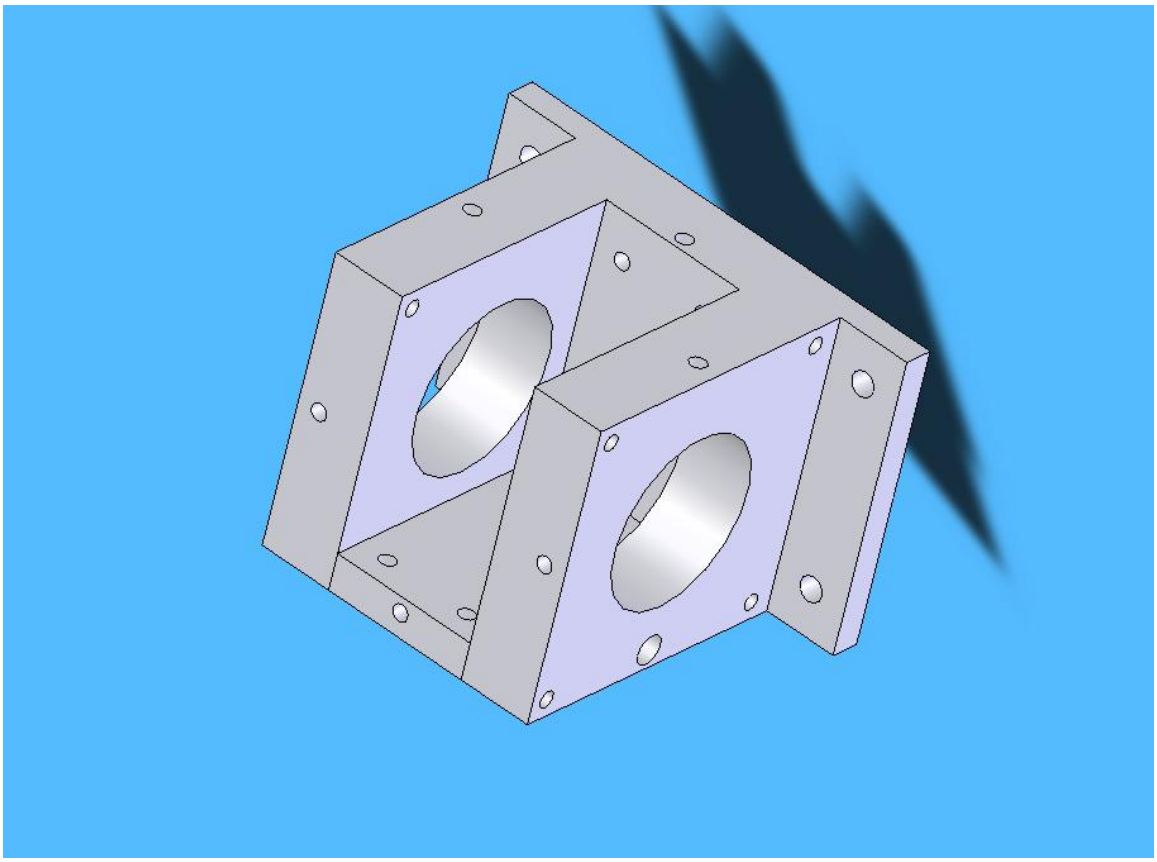

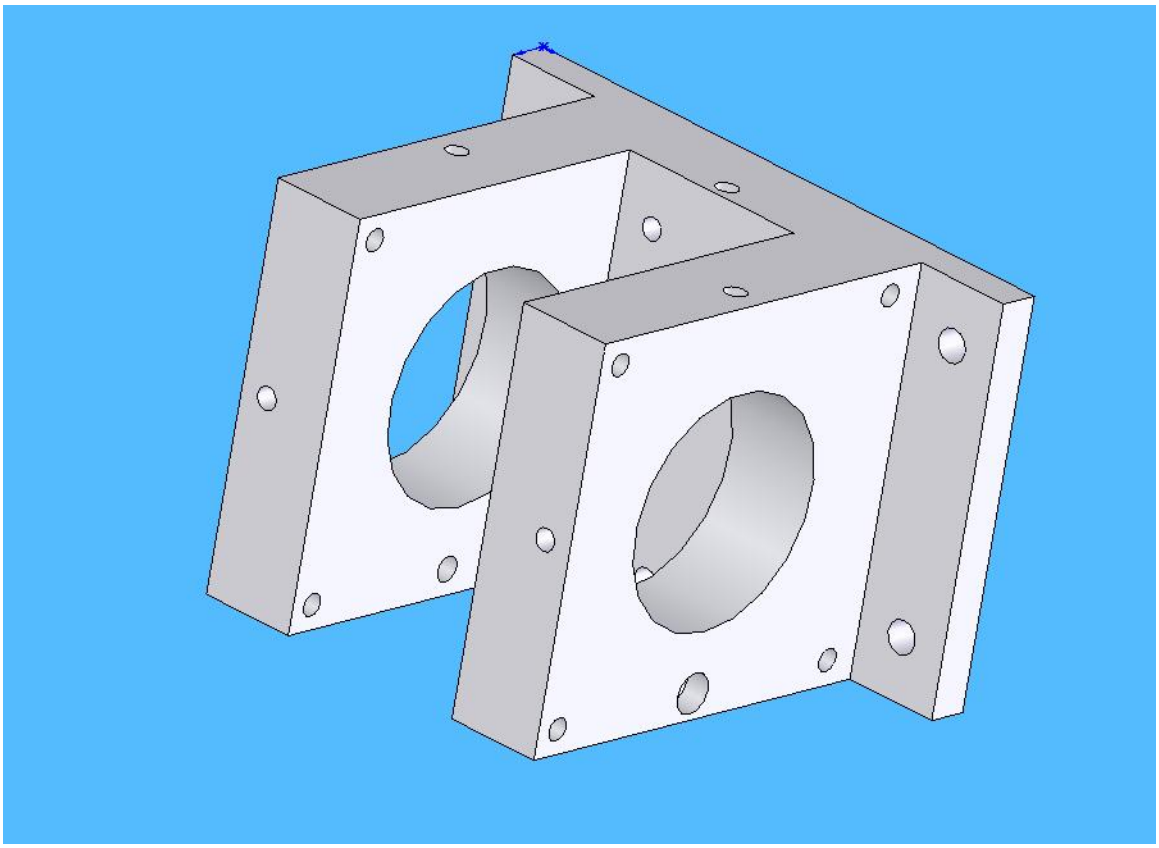

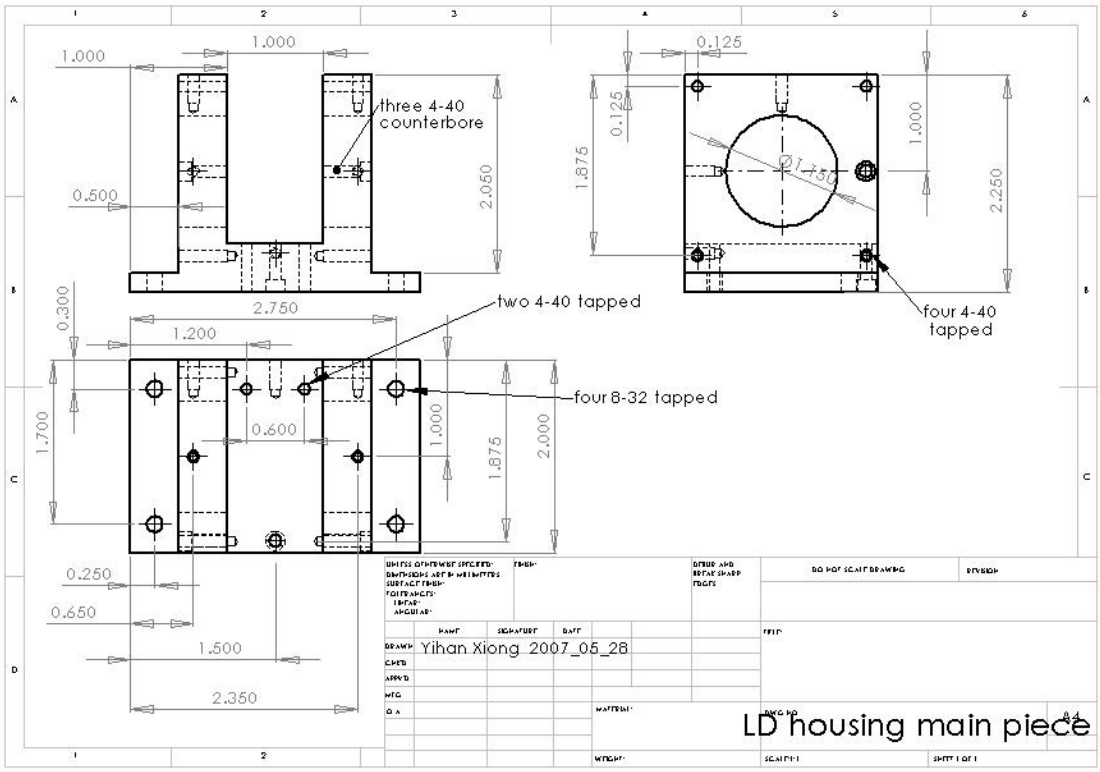
1.000
1.000
three 4-40
counterbore
0.500
2.050
0.125
0.125
1.875
1.000
Ø1.450
2.250
four 4-40
tapped
0.300
2.750
1.200
two 4-40 tapped
four 8-32 tapped
1.700
0.600
1.000
1.875
2.000
0.250
0.650
1.500
2.350
Yihan Xiong 2007_05_28
LD housing main piece

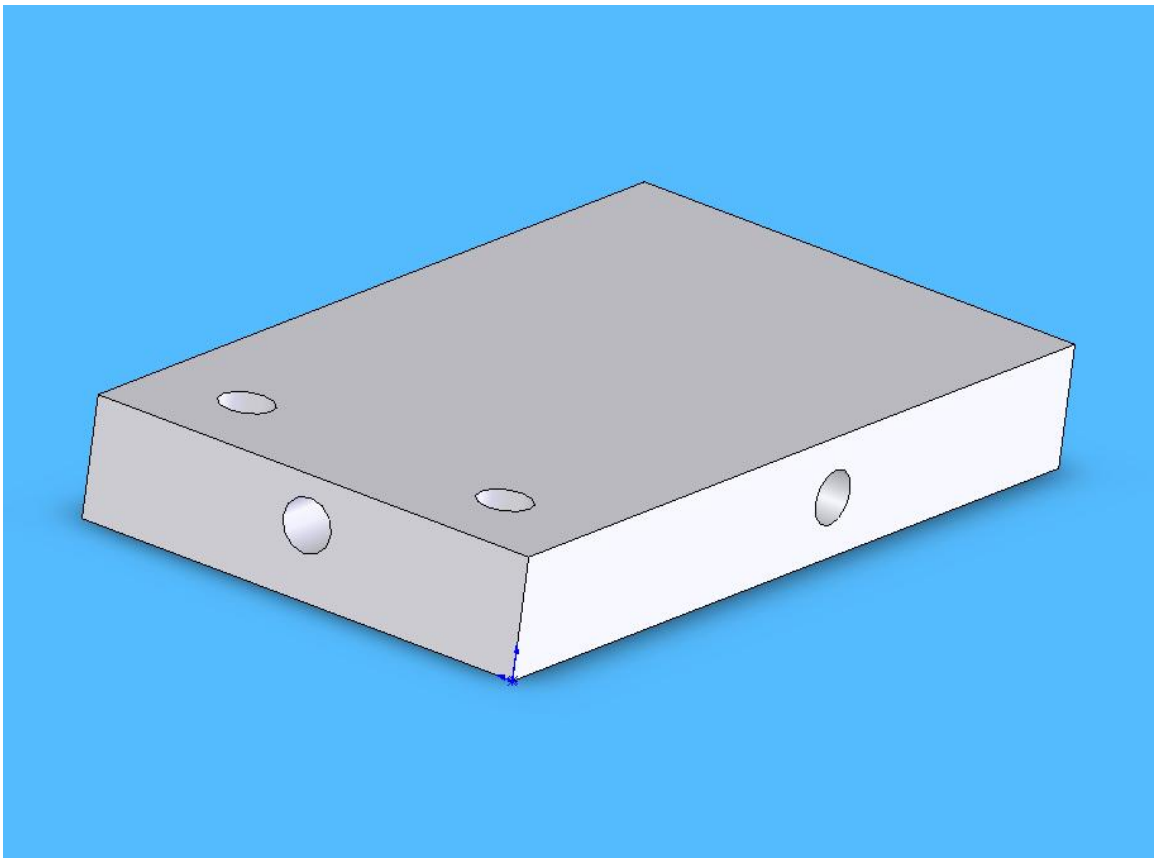

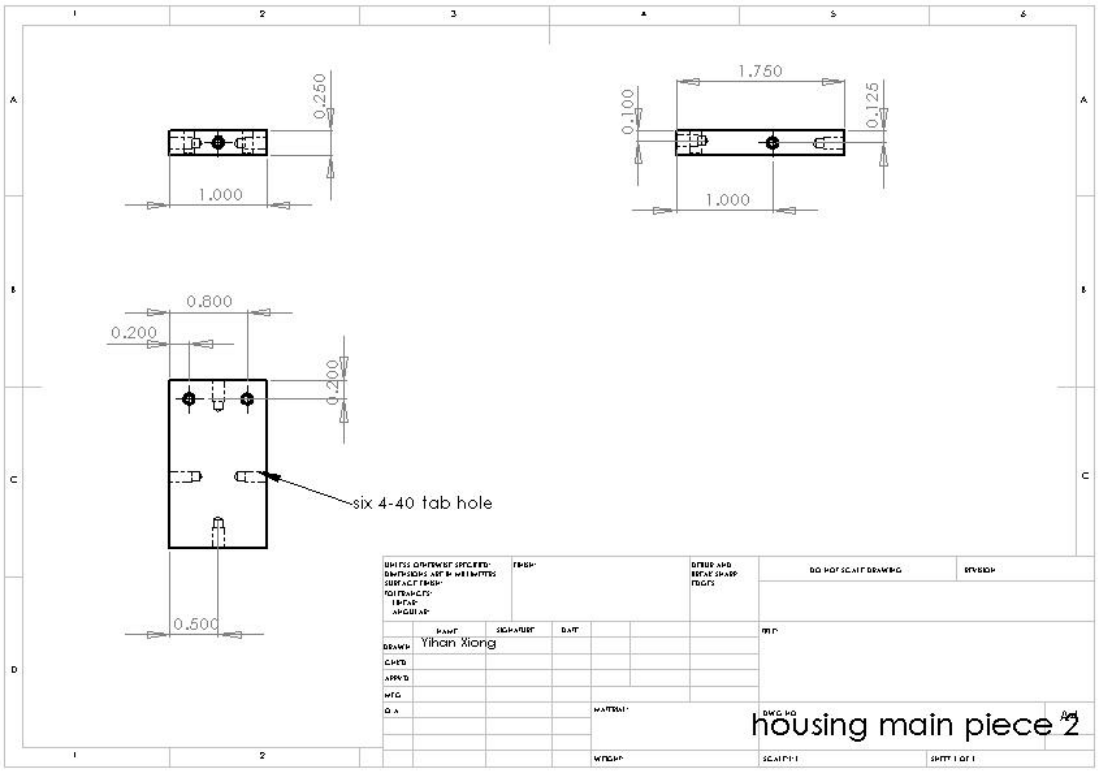
0.250
1.000
1.750
0.100
0.125
1.000
0.800
0.200
0.200
six 4-40 tab hole
0.500
Yihan Xiong
housing main piece 2

Heat Sink

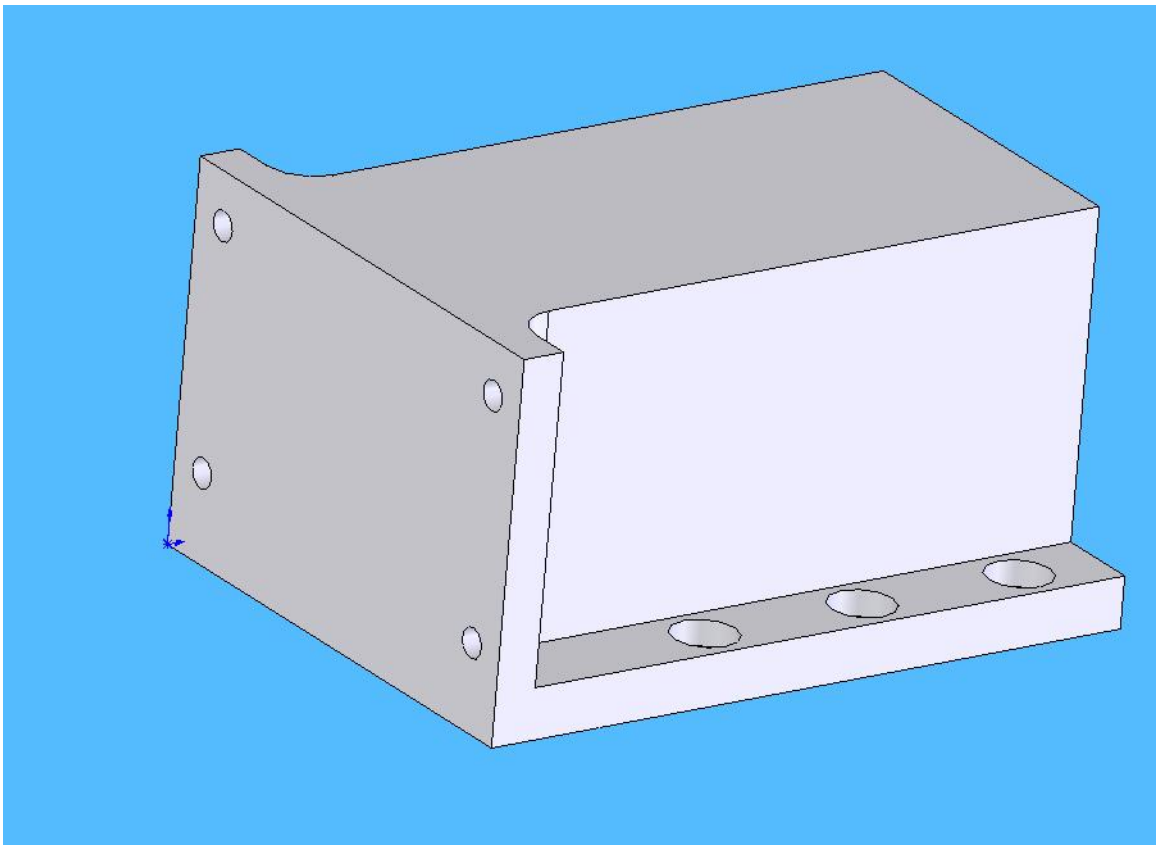

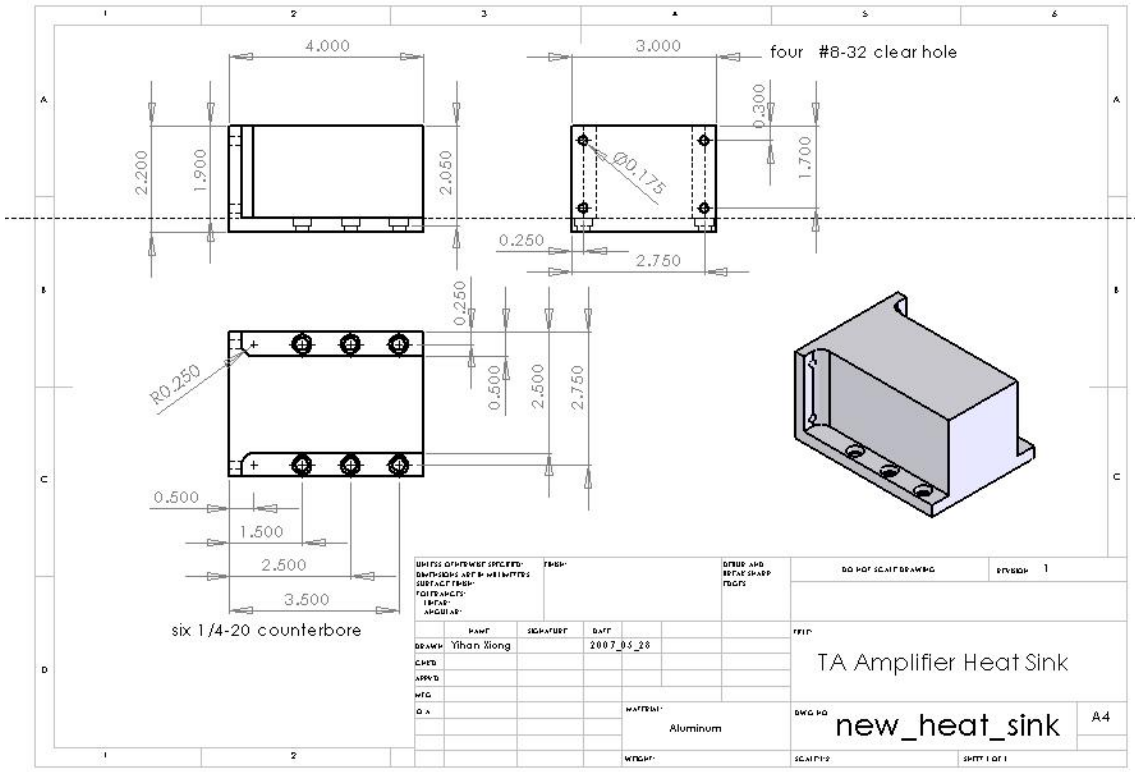
4.000
3.000
four #8-32 clear hole
2.200
1.900
2.050
0.300
1.700
Ø0.175
0.250
2.750
0.250
R0.250
0.500
2.500
2.750
0.500
1.500
2.500
3.500
six 1/4-20 counterbore
TA Amplifier Heat Sink
new_heat_sink
A4
Aluminum
Yihan Xiong
2007_05_28

Top Case

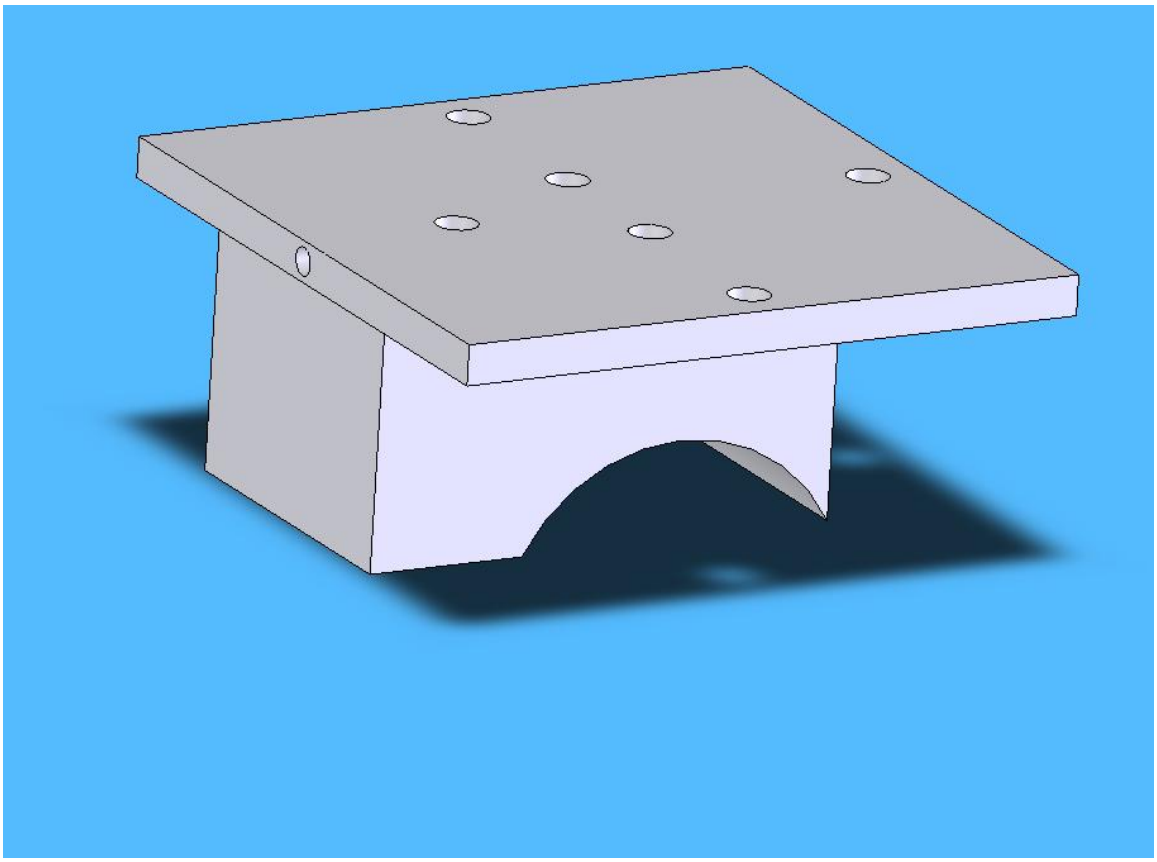

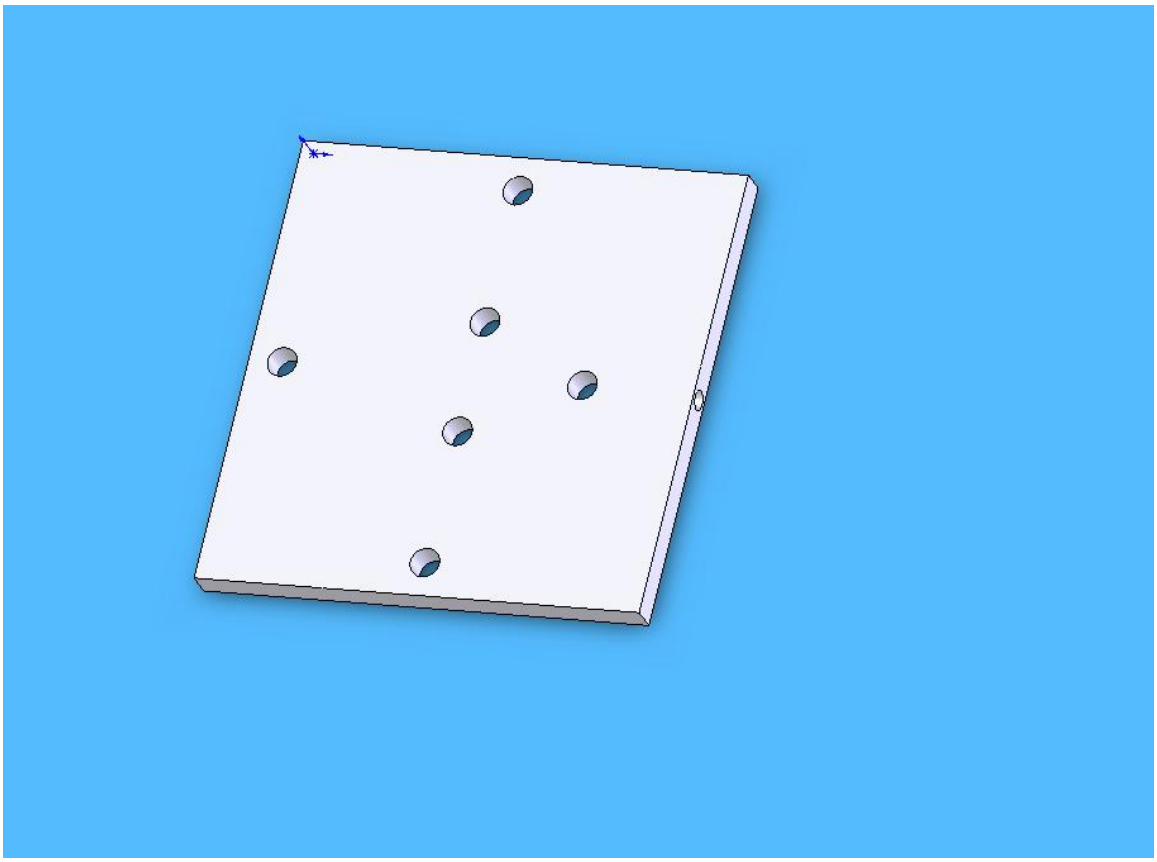

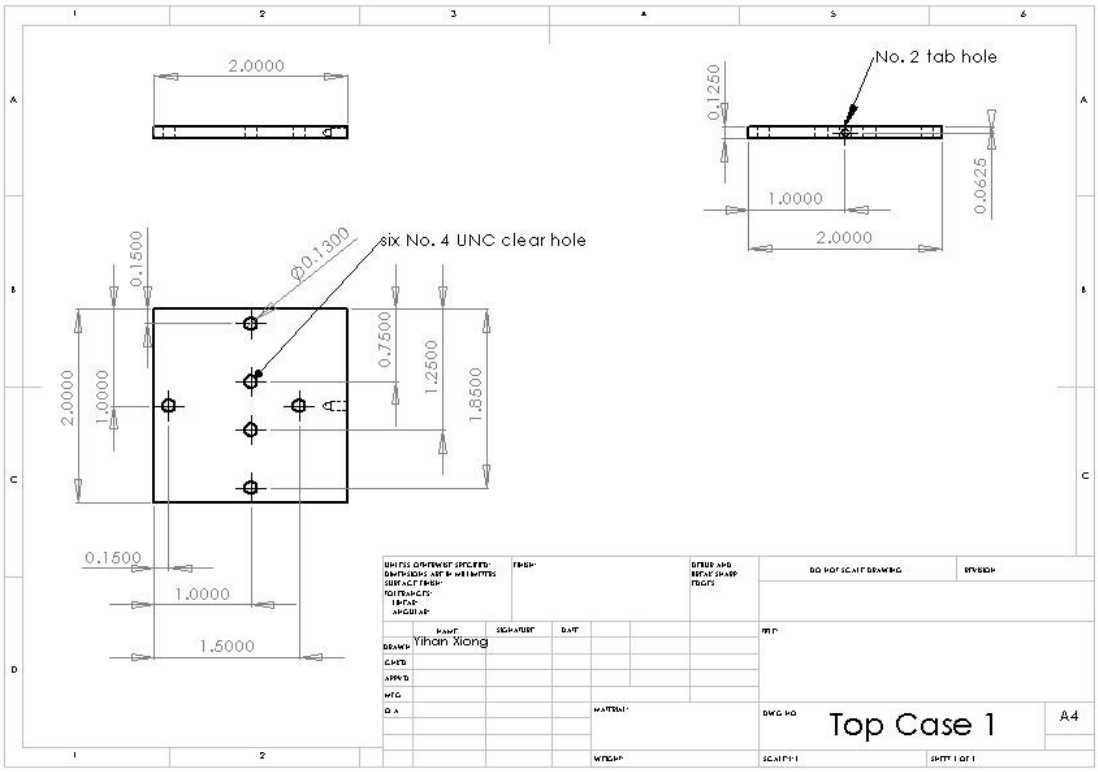
2.0000
No. 2 tab hole
0.1250
0.0625
1.0000
2.0000
six No. 4 UNC clear hole
Ø0.1300
0.1500
0.7500
1.2500
1.8500
2.0000
1.0000
0.1500
1.0000
1.5000
Yihan Xiong
Top Case 1
A4

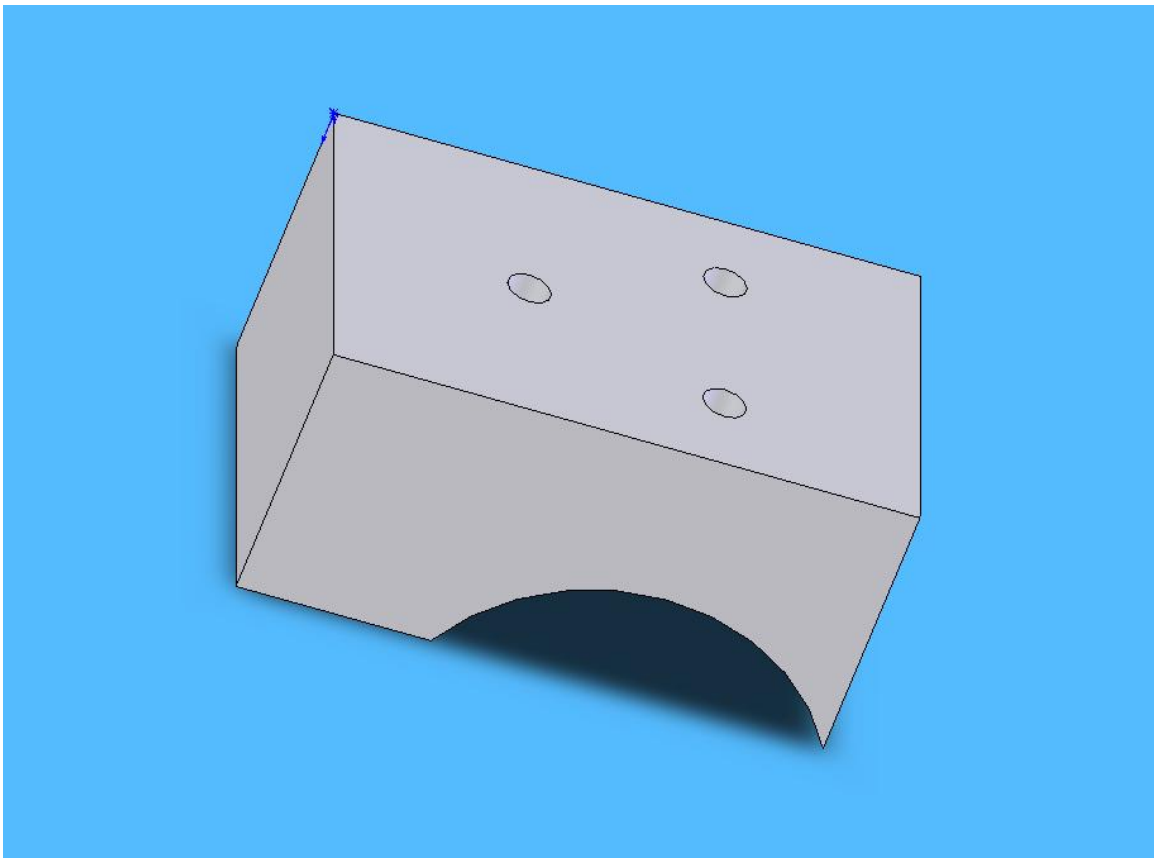

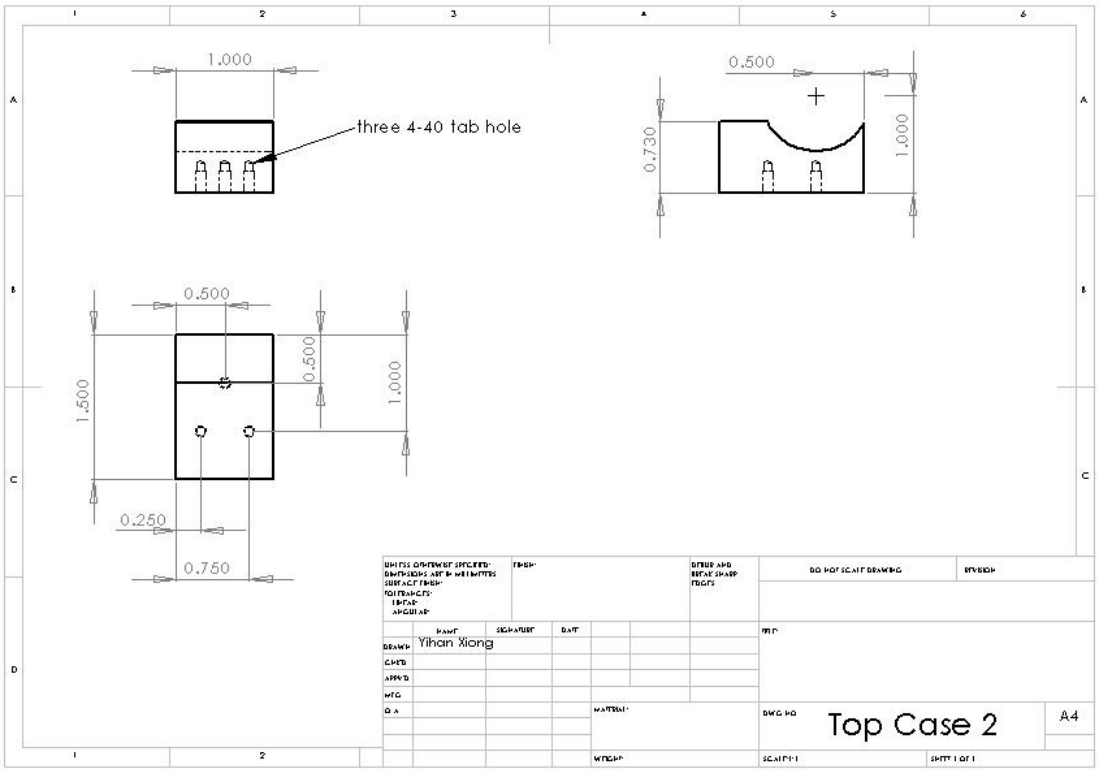
1.000
three 4-40 tab hole
0.500
0.730
1.000
0.500
1.500
0.500
1.000
0.250
0.750
Yihan Xiong
Top Case 2
A4

Front Case

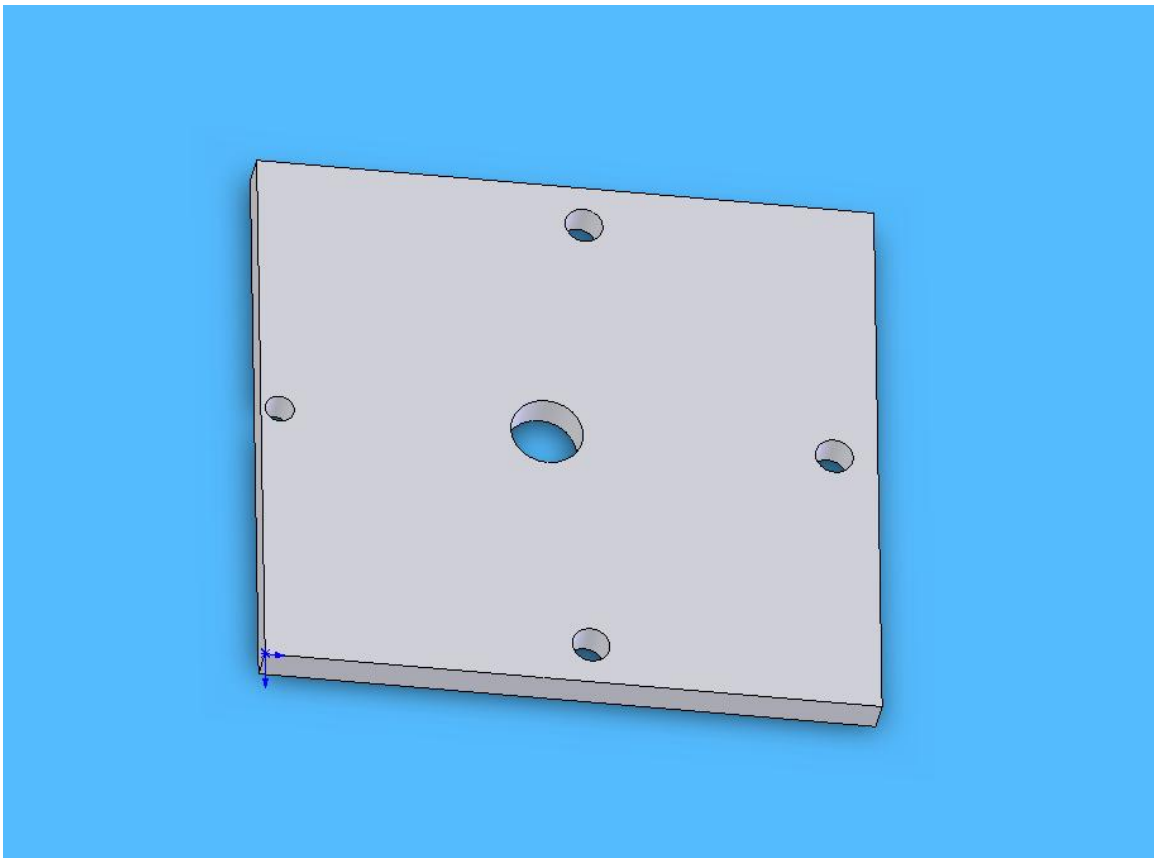

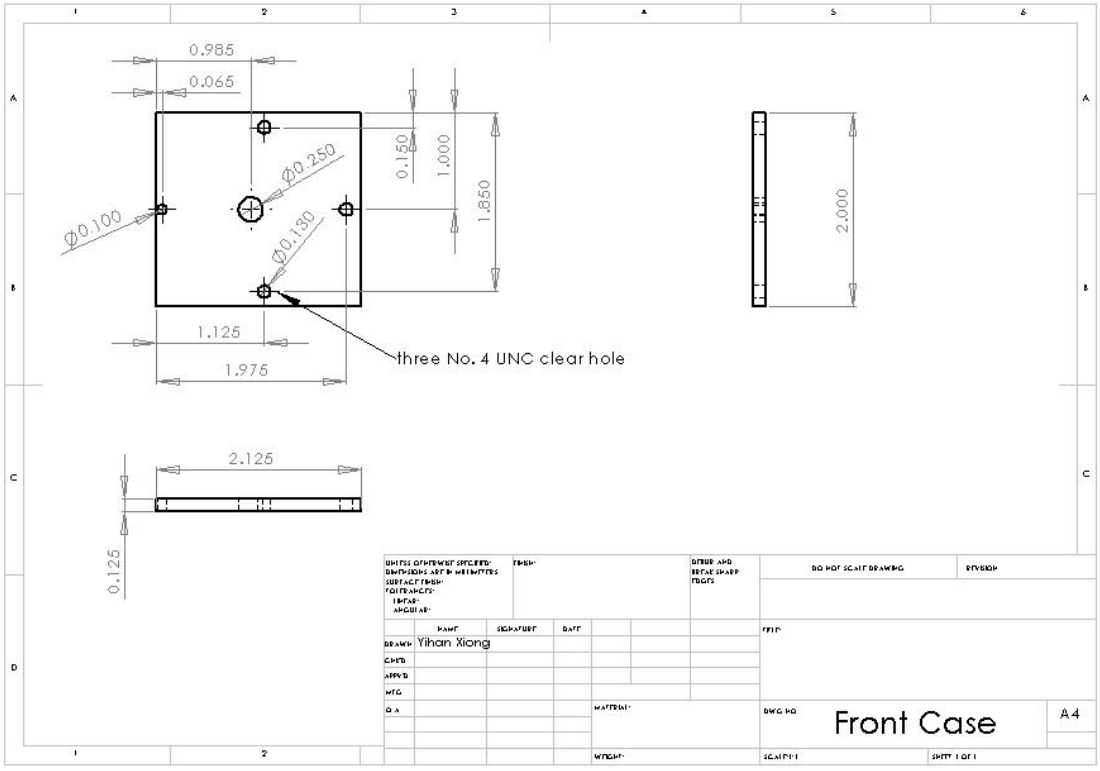
0.985
0.065
0.150
1.000
1.850
Ø0.250
Ø0.100
Ø0.130
1.125
1.975
three No. 4 UNC clear hole
2.000
2.125
0.125
Yihan Xiong
Front Case
A4

APPENDIX G

COLLIMATION CALCULATION FOR THE TAPERED AMPLIFIER SYSTEM

From the manufacture's data, the input and output aperture of the gain region is 3 μm and 190 μm respectively. We assume the index of refraction of the gain medium $n_1 \approx 3$ and index of the refraction of the air is $n_2 = 1$.

Figure G-1 is the top view of the tapered amplifier diode. From the basic geometry, $\theta_1 = \tan^{-1}(\frac{190/2}{2750}) = 1.978°$. Then from the Snell's law $n_1 \sin(\theta_1) = n_2 \sin(\theta_2)$, we have $\theta_2 = \sin^{-1}[\frac{n_1 \sin(\theta_1)}{n_2}] = 5.9°$ or $2\theta_2 = 11.8°$ and $h_1 = \frac{190/2}{\tan(\theta_2)} = 912.3$ μm. The manufacture's data shows the parallel divergence angle is $7° \sim 13°$, which consistent with our calculation $11.8°$. The perpendicular divergence angle from the datasheet is about $28°$. Since these two divergent angles differ a lot, it is impossible to collimate the beam with just one spherical lens. An extra cylindrical lens is needed after the spherical lens.

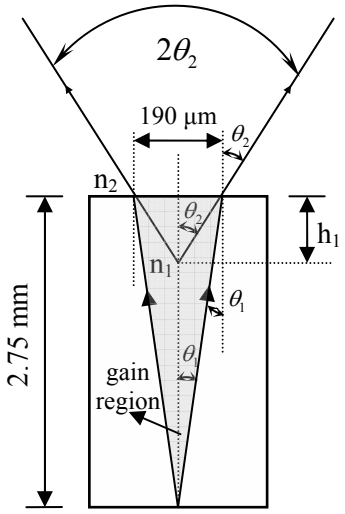

Figure G-1. The top view of the tapered amplifier diode. The shadowed area represents the gain region. The parallel divergent angle is about $11.8°$.

Collimating the Divergent Beam in the Perpendicular Direction

We choose to use a spherical lens with $f_s = 4.5$ mm to collimate the perpendicular divergent beam first. The height of the gain region is not given from the datasheet, but based on the single slit diffraction limit, we assume the height is about $2.4\ \mu m$, which is comparable with the input aperture, but much smaller than the output aperture in the paralle direction. The spherical lens is 4.5 mm away from the output aperture. The perpendicular divergent angle as shown in figure G-2 is $28°$ and we can calculate the collimated beam radius $R_1 = 4.5 \times \tan(14°) = 1.122$ mm based on simple geometry.

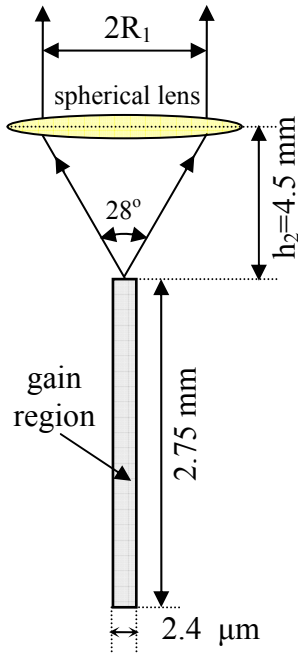

Figure G-2. The side view of the tapered amplifier diode. A spherical lens with focal length of 4.5 mm is used here to collimate the perpendicular divergent beam. The resulting collimated beam radius is 1.122 mm.

Collimating the Divergent Beam in the Parallel Direction

Now we need to collimate the divergent beam in the parallel direction to the same size as in the perpendicular direction. Unlike the perpendicular one, after a spherical lens, the beam does not collimate as shown in figure G-3, so an extra cylindrical lens is placed after the spherical lens.

From the earlier discussion, we know $h_1 = 912.3\ \mu\text{m}$, $h_2 = 4.5\ \text{mm}$ and $f_s = 4.5\ \text{mm}$. The Gaussian Lens Formula $\frac{1}{(h_1 + h_2)} + \frac{1}{h_3} = \frac{1}{f_s}$ gives $h_3 = 26.703\ \text{mm}$. Based on the figure G-3, $R_3 = (h_1 + h_2)\tan(\theta_2) = 1.121\ \text{mm}$ and $\frac{R_3}{R_1} = \frac{h_3}{h_4}$, then $h_4 = 52.537\ \text{mm}$, which also should be focal length of the cylindrical lens $f_c = 52.537\ \text{mm}$.

Summary of the Collimating the Tapered Amplifier Output Beam

In order to collimate the output beam from the tapered amplifier diode, we need to put a spherical lens ($f_s = 4.5\ \text{mm}$) 4.5 mm away from the diode and a cylindrical lens ($f_c = 52.537\ \text{mm}$) 7.9 cm after the special lens. With these parameters, the final collimated beam radius is 1.122 mm.

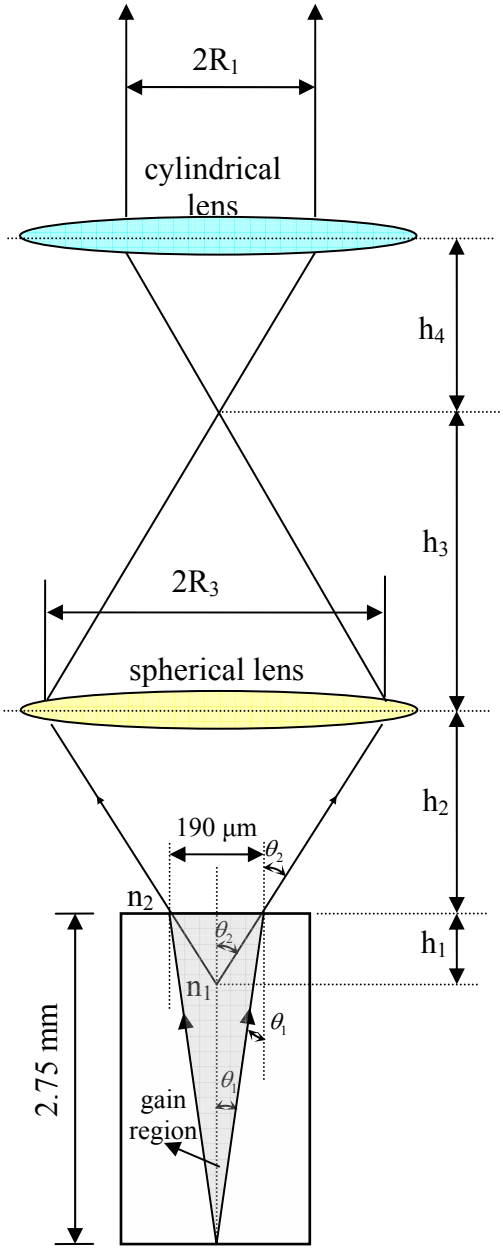

Figure G-3. Optical design of how to collimate the parallel divergent beam.

APPENDIX H

CAVITY RINGDOWN MEASUREMENTS

Principle of Ringdown Measurements

In a high finesse cavity with the mirror's reflectivity ~0.9999, an accurate way to determine the reflectivity of the mirrors is by measuring the cavity's ringdown time. The principle of the cavity ringdown measurement is that after shutting down the incident beam, we measure the time the light takes to leak out from the cavity and then convert this time to the mirror's reflectivity.

Assuming the electric field inside the cavity is E, cavity length is L, the cavity loss is α, the intra-cavity laser field equation can be written in the absence of a medium as

$$\frac{dE}{dt} = -\alpha E \tag{H.1}$$

or

$$dE = -\alpha E dt \tag{H.2}$$

or

$$E(t) = E_0 e^{-\alpha t} \tag{H.3}$$

where E_0 is the intra-cavity electric field at the moment when the incident beam gets shut down. We integrate the Eq. (H.2) over one round trip time $\frac{2L}{c}$. After one round trip time (or bouncing once from each mirror), the electric field E changes from E_0 to $E_0(\sqrt{R})^2$, where R is the mirror's reflectivity.

$$\int_{E_0}^{E_0 R} \frac{1}{E} dE = -\alpha \int_0^{\frac{2L}{c}} dt \tag{H.4}$$

Eq. (H.4) can be simplified to

$$\ln(R) = -\alpha \frac{2L}{c}. \tag{H.5}$$

Now we have

$$\alpha = -\frac{c}{2L}\ln(R) \tag{H.6}$$

From Eq. (H.3), when $t = \tau = \frac{1}{2\alpha}$, the intensity $I(\tau) = \frac{1}{e} I_0$

$$\ln(x) \simeq \frac{x-1}{\sqrt{x}} \qquad (x \sim 1) \tag{H.7}$$

$$\ln(R) \simeq \frac{R-1}{\sqrt{R}} \tag{H.8}$$

$$\tau = \frac{1}{2\alpha} = -\frac{2L}{2c}\frac{\sqrt{R}}{R-1} = \frac{L}{c}\frac{\sqrt{R}}{(1-R)} \tag{H.9}$$

The free spectral range (FSR) of the cavity is $\frac{c}{2L}$ and the finesse of the cavity is $\frac{\pi\sqrt{R}}{1-R}$, the linewidth (LW) of the cavity is defined as $\text{LW} = \frac{\text{FSR}}{\text{Finesse}} = \frac{c}{2L}\frac{1-R}{\pi\sqrt{R}}$, so $\tau = \frac{1}{2\pi}\frac{1}{\text{LW}}$

For our HFC, $\text{LW} \approx \frac{\text{GHz}}{10^4} \approx 100\ \text{kHz}$, $\tau = \frac{1}{2\pi}\frac{1}{100\ \text{kHz}} \approx \mu\text{s}$, which is an easily measurable scale.

Experimental Setup and Results

Experimental Setup

Figure H-1 shows the experimental setup for the ringdown measurements. The laser diode first goes through an acoustic-optic modulator (AOM), and the first order diffraction light from the AOM acts as an incident beam to the high finesse cavity (HFC). A detector is placed after the HFC measuring the leaking light power as a function of time (ringdown time). A high voltage supply is used to finely adjust the HFC length through the piezoelectric transducer (PZT) inside the cavity. Since the linewidth of the HFC is narrow, by finely tuning the voltage, we can meet the resonant condition, allowing the light to transmit through the HFC. Once the transmitted light from the HFC hits the detector, the electric servo will immediately shut down the first order diffraction light. Thus the ringdown time can be measured by the detector and an oscilloscope.

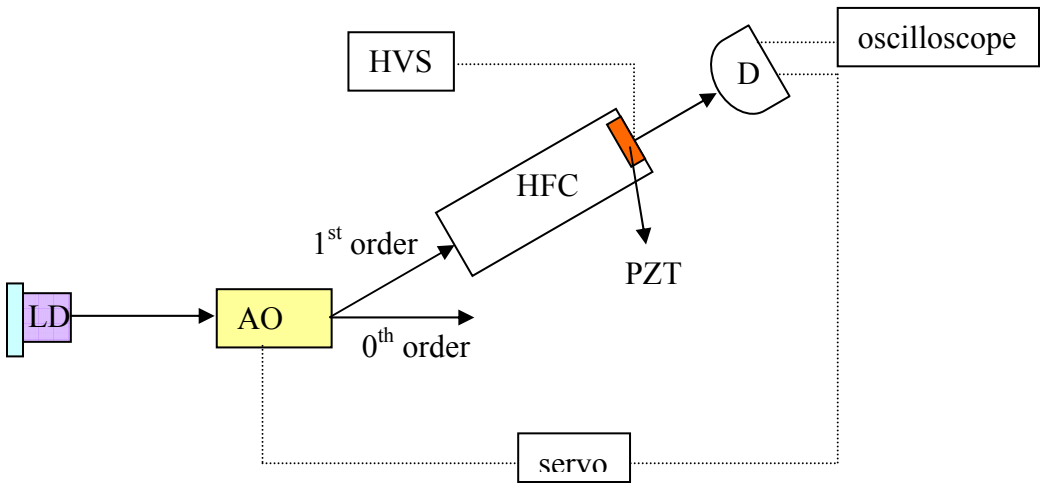

Figure H-1. The experimental setup for ringdown measurement. (LD---laser diode, AOM---acoustic-optic modulator, HFC---high finesse cavity, HVS---high voltage supply, PZT--- piezoelectric transducer, D---detector). Dotted lines represent electronic wires.

Experimental Results

Figure H-2 shows four sets of experimental data and exponential decay fits to the data. Using the exponential fits, we can determine the decay time (~μs) and then convert it to the finesse of the cavity and the reflectivity of the mirror. In this case, the reflectivity result is consistently around 0.99983.

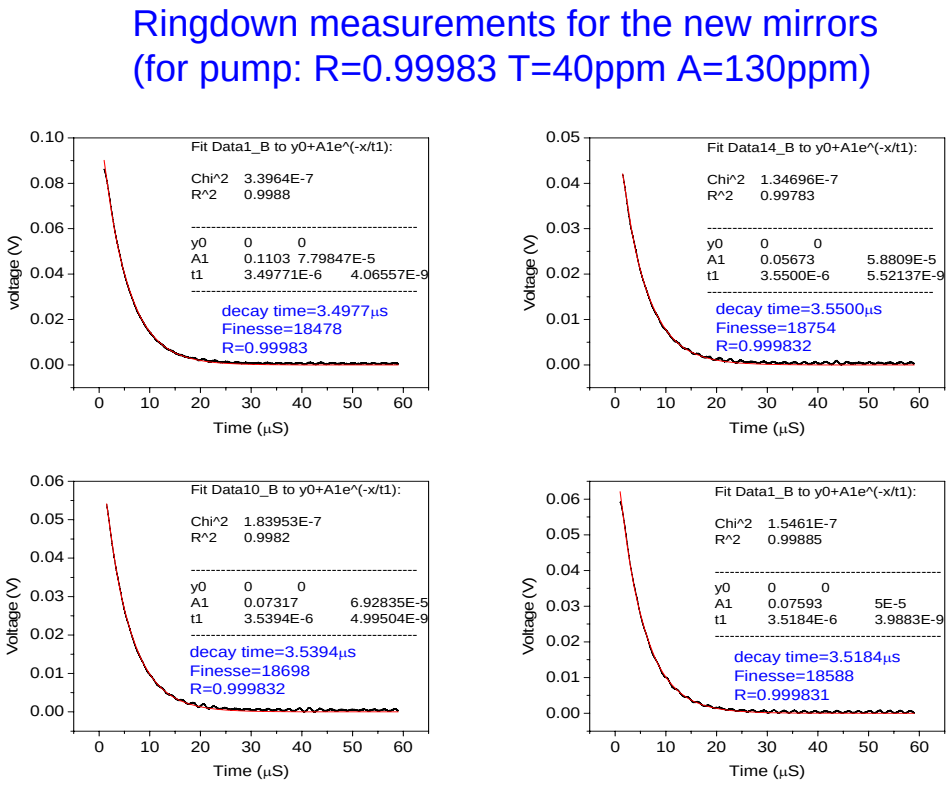

Figure H-2. Experimental data and exponential decay fitting data of the ringdown time.

APPENDIX I

ACRONYMS USED IN THIS THESIS

AOM — Acoustic-optic modulator

CW — Continuous-wave

CW-ECDL — Continuous-wave External Cavity Diode Laser

ECDL — External Cavity Diode Laser

EOM — Electro-optic Modulator

FI — Faraday Isolator

FSR — Free Spectral Range

FWHM — Full Width Half Maximum

HFC — High Finesse Cavity

HWP — Half Wave Plate

ML — Mode-locked

ML- ECDL — Mode-locked External Cavity Diode Laser

OSA — Optical Spectrum Analyzer

PBS — Polarizing Beam Splitter

PM — Polarizing Maintaining

PMT — Photon Multiplier Tube

PZT — Piezoelectric Transducer

QWP — Quarter Wave Plate

SM — Single Mode

SRS — Stimulated Raman Scattering

TA — Tapered Amplifier